NOVEL APPROACHES TO HIGH RESOLUTION STUDIES OF CALCAREOUS NANNOFOSSILS

EMMA M. HANSON

A thesis submitted to the University of Birmingham
for the degree of DOCTOR OF PHILOSOPHY

School of Geography, Earth and Environmental Sciences
College of Life and Environmental Sciences
University of Birmingham

March 2023

UNIVERSITY OF
BIRMINGHAM

University of Birmingham Research Archive

e-theses repository

This unpublished thesis/dissertation is copyright of the author and/or third parties. The intellectual property rights of the author or third parties in respect of this work are as defined by The Copyright Designs and Patents Act 1988 or as modified by any successor legislation.

Any use made of information contained in this thesis/dissertation must be in accordance with that legislation and must be properly acknowledged. Further distribution or reproduction in any format is prohibited without the permission of the copyright holder.

Abstract

Coccolith carbon isotope 'vital effects', which are the departure of the coccolith isotopic composition from the expected isotopic signature of inorganic calcite, are proposed to have originated in the late Miocene, between 7 and 5 million years ago. The main control on the size of these vital effects is the degree of carbon limitation experienced by the coccolithophore cell during coccolithogenesis. In culture studies, the main extant species are split into an isotopically 'heavy' group of small, lightly calcifying forms, such as *Gephyrocapsa oceanica* and *Emiliania huxleyi*, and an isotopically 'light' group of large, heavily calcifying forms, such as *Calcidiscus leptoporus* and *Coccolithus pelagicus*. This division between small, lightly calcifying and large, heavily calcifying forms is also well established in data from the geological record. The application of this understanding to the generation of new proxy measures for past ocean and ecological functioning is, however, hampered by the available size separation protocols that are labour intensive, time consuming and cannot be used to generate the ideal orbital-scale proxy records of environmental change. This thesis addresses this problem with the introduction of a novel size separation technique that allows for the rapid sample preparation of coccolith-rich sediments into very coarse and very fine coccolith size fractions. Using this new technique this thesis presents two new high-resolution records of coccolith geochemistry – including oxygen and carbon isotopes and strontium/calcium ratios - with one spanning the Pliocene-Pleistocene Transition (3.01 to 1.38 million years ago) and the second a long-term record from the Miocene to Recent (7.7 to 0.1 million years ago). Both records are based on analyses of sediment from International Ocean Discovery Program Expedition 363, Site U1482, off the northwest margin of Australia. Site U1482 has a continuous sedimentary sequence from the late Miocene to Recent, with well-preserved nannofossil carbonate present throughout. The short term Plio-Pleistocene record provides a reference framework for high-resolution coccolith geochemistry in a stable tropical environment across a long

sequence of orbital-scale variability. The long-term Miocene to Recent study records the onset of these coccolith vital effects and how they change with nannofossil evolution and climatic changes. These two records support the use of the new size separation technique and provide the highest resolution coccolith geochemistry records over the two time periods to date.

Acknowledgements

I could not have gotten through my PhD journey without the help and support from countless people. Firstly, a massive thank you to my supervisor, Tom Dunkley Jones. Without his help, patience, and constant support, this PhD would never have come to fruition. A sincere thank you for allowing me to work on these samples after my MSc, without doing so would never have meant a furthering career in research and science. A further thank you to all of the wonderful staff in the Earth Sciences department for many insightful talks and great company over the years (as well as an excellent array of pet pictures).

I am forever grateful for the friends I have made over the years at the University of Birmingham, whether office mates, fellow PhDs, or wonderful post docs, all past and present. This experience would have been very different (and boring) without you all, so thank you for making it so fun.

To my family, particularly my parents and grandparents, thank you for not asking 'when will you finally stop being a student?' too much and being a great support throughout anything and everything that I have done. To my sister Phoebe, thank you for making me cry-laugh exactly when I needed it.

A particular massive thanks to Emma and Thomas, for the entertaining evenings, keeping us sane during lockdowns, and being a constant source of laughter. To Mariem, Will and Lyra, for being there for us whilst I was on the Sonne and being a constant source of smiles every day. To Sarah, for the final push care packages and constant check ins about the tiny dinosaurs over the years. To Charlotte and Becca, the friends bought together by a hellish year that thankfully stuck around, you've been a constant source of joy. And to so so many more people who played such an important part in getting me through this PhD, thank you.

To my favourite person Harry, thank you for your unwavering support throughout the course of the PhD and beyond, I couldn't have done it without you. But most

importantly thank you for agreeing to us having a dog. And to my favourite non-person, Hugo, thank you for keeping me sane and for constantly keeping me on my toes, as well as being a reliable source of fluff and comfort.

This work was 50% funded by a Natural Environment Research Council (NERC) National Productivity Investment Fund (NPIF), with training and RTSG provided by the Oil & Gas Centre for Doctoral Training. The other 50% was funded by the University of Birmingham. Samples were provided by the International Ocean Discovery Program (IODP).

Statement of Impact of Pandemic on Work

- The lockdown and closure of labs from the March (2020) of my second year, and not reopening again until October (2020) of my third year, but then with further limited access through my third year of study (2020-21).
- First year (2018-2019) dominated by Oil & Gas CDT training which would usually leave subsequent years more free - but lack of access to labs and delayed automated microscope stage installation meant it was difficult to move project forward.
- Also delayed by a year (March 2020 to March 2021) was the installation of the automated microscope stage, which then required significant method development from me during my third year.
- Visits planned to go and work with collaborators on an automated system during my second year (Summer 2020) did not happen.

Contents

1 INTRODUCTION **1**

1.1 Overview 1
1.2 Coccolithophores 2
1.3 Vital effects in coccolithophores 3
1.4 Strontium-Calcium as a productivity indicator 7
1.5 Thesis objectives and outline 10

2 A NOVEL SIZE SEPARATION TECHNIQUE OF THE < 20 μm FRACTION FOR USE IN COCCOLITH GEOCHEMICAL ANALYSES **13**

2.1 Introduction 13
2.2 Sample selection 16
2.3 Preparation of sediments 18
2.3.1 Washing 18
2.3.2 Centrifuging 18
2.3.3 Drying 19
2.3.4 Separating 19
2.4 Particle size analysis 21
2.4.1 Slide settling technique 21
2.4.2 Microscope imaging & image processing 22
2.5 Results 25
2.6 Conclusion 32

3 NOVEL APPROACHES TO HIGH-RESOLUTION COCCOLITH GEOCHEMISTRY OVER THE PLIOCENE-PLEISTOCENE TRANSITION **34**

3.1 Introduction 34
3.2 Methodology 41
3.2.1 Sample selection 41
3.2.2 Stable isotope analysis 42
3.2.3 Trace metal analysis 44
3.2.4 Spectral analysis 47

3.2.5 Nannofossil assemblage analysis . . . 47
3.2.6 Particle size analysis . . . 48
3.3 Results . . . 48
3.3.1 Stable isotope analysis - δ^{13}C . . . 48
3.3.2 Stable isotope analysis - δ^{18}O . . . 50
3.3.3 Spectral analysis . . . 51
3.3.4 Trace metal analysis . . . 54
3.3.5 Nannofossil assemblage analysis . . . 56
3.3.6 Taxonomic composition of size separations . . . 56
3.3.7 Size corrections for δ^{13}C . . . 59
3.4 Discussion . . . 61
3.4.1 Coccolith size-fraction δ^{13}C . . . 61
3.4.2 Coccolith size-fraction δ^{18}O . . . 66
3.4.3 Coccolith size-fraction Sr/Ca . . . 68
3.5 Conclusion . . . 71

4 NOVEL APPROACHES TO COCCOLITH GEOCHEMISTRY OVER THE MIOCENE TO RECENT 73
4.1 Introduction . . . 73
4.2 Methodology . . . 79
4.2.1 Sample selection . . . 79
4.2.2 Stable isotope analysis . . . 81
4.2.3 Particle size analysis . . . 82
4.3 Results . . . 83
4.3.1 Stable isotope analysis - δ^{13}C . . . 83
4.3.2 Stable isotope analysis - δ^{18}O . . . 83
4.3.3 Particle size analysis . . . 86
4.3.4 Size corrections of δ^{13}C . . . 87
4.4 Discussion . . . 89
4.4.1 Coccolith size-fraction stable isotopes and geochemistry . . . 89
4.5 Conclusion . . . 97

5 CONCLUSIONS & FUTURE WORKS 100
5.1 General conclusions and summary . . . 100
5.2 Further work . . . 103

References 105

List of Figures

1.1 Schematic cartoon of isotope fractionation in coccolithophores, from Rae et al. (2021) 6
1.2 Scatter plot of carbon and oxygen isotope offsets with increased CO_2 concentration, from Hermoso et al. (2016a) 7
1.3 Sr/Ca ratios in cultures vs. organic carbon fixation rate estimated from cell volume and growth rates, from Stoll et al. (2002b) 9

2.1 Results of coccolith size following centrifugation technique from Zhang et al. (2021) 15
2.2 Map of Site U1482, IODP Exp. 363 (modified from Rosenthal et al. (2018), with modern day chlorophyll concentrations and sea surface temperatures 17
2.3 Schematic illustration of novel size separation method 20
2.4 Thresholding process within Fiji software 23
2.5 Binary image after setting threshold on Fiji software 23
2.6 Output of particle analysis measurement on Fiji software 24
2.7 Examples of 'good' vs. 'bad' images for particle size analysis 25
2.8 Average particle size (μm^2) vs age from the Pliocene-Pleistocene study 27
2.9 Cumulative percentage plots with the average particle size (μm^2) 32

3.1 Map of Site U1482 and the primary currents around the north western margin of Australia and through the Indo-Pacific Warm Pool (IPWP) (modified from Rosenthal et al. (2018) 39
3.2 Site U1482 age model, from Chen et al. (2022) 42
3.3 Carbon isotope analysis ($\delta^{13}C$) and the difference of the very fine (VF) coccolith fraction and very coarse (VC) coccolith fraction over the Pliocene-Pleistocene 50
3.4 Oxygen isotope analysis ($\delta^{18}O$) and the difference of the very fine (VF) coccolith fraction and very coarse (VC) coccolith fraction over the Pliocene-Pleistocene 52

3.5 Spectral power versus frequency plots for $\delta^{13}C$ and wavelet analysis . . 53
3.6 Lead-lag relationship between $\delta^{13}C_{VF}$ and $\delta^{13}C_{VC}$ 54
3.7 Trace metal analysis (Sr/Ca) and the difference of the very fine (VF) coccolith fraction and the very coarse (VC) coccolith fraction and the difference between the VF and VC over the Pliocene-Pleistocene 55
3.8 Nannofossil assemblage analysis samples spanning from the Pliocene to the Pleistocene 57
3.9 Assemblage contribution and mass contribution of 5 samples in the Pleistocene 58
3.10 Average differential size offset between the VF and VC fractions versus $\Delta\delta^{13}C$ 60
3.11 $\delta^{18}O$ versus $\delta^{13}C$ and $\delta^{13}C$ versus average particle size (μm^2) 62
3.12 Isotopic difference and Sr/Ca ratios for small reticulofenestrids vs. large *Helicosphaera*, edited from Bolton et al. (2012) 63
3.13 Size separated coccolith fraction $\delta^{13}C$ and $\delta^{13}C$ of *Globigerinoides ruber* 65
3.14 Net primary productivity from *Florisphaera profunda* 70

4.1 Atmospheric CO_2 reconstructions since the Miocene to Recent. Data from Rae et al. (2021) 76
4.2 Site U1482 bathymetric map showing Site U1482, Exp. 363 (Rosenthal et al., 2018) 80
4.3 Site U1482 age-depth plot for calcareous nannofossil and planktonic foraminifera biohorizons (Rosenthal et al., 2018) 80
4.4 Stable isotope measurements ($\delta^{13}C$ and $\delta^{18}O$) of the very fine (VF) and very coarse (VC) size fractions from the Miocene to Recent (*cont. on next page)* 85
4.5 Average particle size through time and against $\delta^{13}C$ 87
4.6 Average differential size offset (area) between the VF and VC fraction versus $\Delta\delta^{13}C$ 88
4.7 Comparison of $\delta^{13}C$ from this study and Bolton et al. (2016), with size data for reticulofenestrids 90
4.8 $\Delta\delta^{13}C$ and atmospheric CO_2 over the past 8 million years 93
4.9 $\delta^{18}O$ and *Gephyrocapsa* species abundance since the late Miocene . . 96

1 | INTRODUCTION

1.1 Overview

The study of coccolithophores (also known as calcareous nannoplankton) through the analysis of their fossilised calcite plates has led us to a greater knowledge of pelagic ecosystems and oceans since their Late Triassic appearance in the fossil record (Bown, 2005). Studies range from the assemblage analysis of fossil coccolithophore communities (e.g., Dunkley Jones et al., 2008; Beaufort & Grelaud, 2017; Jones et al., 2019), the geochemical analysis of their calcite plates for carbon isotopic ($\delta^{13}C$) (e.g., Bolton & Stoll, 2013; Bolton et al., 2016) and oxygen isotopic ($\delta^{18}O$) compositions (e.g., Tremblin et al., 2016; Hermoso et al., 2020), and trace metal based productivity indicators (e.g., Saavedra-Pellitero et al., 2017; Stoll et al., 2019). Recent work has started exploring their geochemical compositions for use as palaeothermometers (Tremblin et al., 2016; Hermoso et al., 2020) or in reconstructing atmospheric pCO_2 (Claxton et al., 2022; Godbillot et al., 2022). Understanding how these organisms were reacting to climate and environmental changes in the past can help to infer how they may react in the future, particularly under the effects of anthropogenic change. As they are at the bottom of the marine food web, any changes to coccolithophore communities are likely to impact ocean biogeochemical cycles. For example, a recent study found that ocean warming and acidification was decreasing the nutritional quality of coccolithophores, interfering with the marine food web (Johnson et al., 2022). They are also key in the oceanic carbon cycle as a key part of the biological pump, through their fixation of inorganic carbon via photosynthesis at the surface and the subsequent ex-

port of organic matter, generating a CO_2 sink (Rost & Riebesell, 2004). Unlike other phytoplankton, coccolithophore's production of calcium carbonate liths releases CO_2 in the surface layer in what is known as the carbonate counter pump, making the balance between coccolithophore organic and inorganic production a key driver of modern and ancient ocean chemistry (Rost & Riebesell, 2004). For example, on recent timescales, the increased efficiency of the biological pump has increased with global cooling over the past 15 million years (Boscolo-Galazzo et al., 2021), with a profound effect on the Neogene communities of both calcareous nannoplankton and foraminifera (Boscolo-Galazzo et al., 2022).

This chapter provides an overview of key ideas and background knowledge pertaining to the thesis, including the theory underpinning the development of a new method for coccolith size fraction analysis, as detailed in Chapter 2, as well as an outline of the inner workings of a coccolithophore cell, and how these can influence the measured parameters used throughout this thesis. The thesis objectives and structure are outlined at the end of this chapter.

1.2 Coccolithophores

Coccolithophores are single celled calcifying haptophyte algae that are first recorded in Upper Triassic sediments (Bown et al., 2004) and are abundant in modern day oceans. The coccolithophore cell is surrounded by individual calcite plates (coccoliths) that are produced intracellularly, and surround the cell, often in an interlocking fashion, to form an external covering or coccosphere. The products of the disaggregation of these coccospheres, individual coccoliths, are what is most commonly found in the fossil record. The long ranging and abundant fossil record of the coccolithophores make them the ideal candidate to track palaeoclimatological and palaeoceanographical changes (e.g. Beaufort et al., 2011; Jones et al., 2019; Hermoso et al., 2020; Tangunan et al., 2021). As coccoliths often constitute a high percentage (up to 60%) of total calcium carbonate in the ocean (Flores & Sierro, 2013), they are an important factor in studies of changing

ocean chemistry.

1.3 Vital effects in coccolithophores

Isotopic vital effects in coccoliths were first noted by Dudley et al. (1986), but substantial advances in coccolith geochemistry and methodological developments have taken place in the 21st Century (e.g., Ziveri et al., 2003; Rickaby et al., 2010; Bolton & Stoll, 2013; Hermoso et al., 2020). A vital effect - the isotopic departure of the coccolith from inorganic calcite - occurs due to the physiology of the coccolithophore deviating isotopic fractionation during calcification away from inorganic thermodynamic (equilibrium) values. As coccoliths are produced intracellularly, physiological processes exert a major control on the chemistry of the site of calcification – the coccolith vesicle – leaving a lasting imprint on the chemistry of coccolith calcite that can be preserved for tens of millions of years. The isotopic divergence from inorganic calcite can be as much as 5 ‰ in both carbon (δ^{13}C) and oxygen (δ^{18}O) isotopes (Dudley et al., 1986; Ziveri et al., 2003). Modelling and experimental work to constrain the inner workings of both oxygen and carbon isotope fractionation in the cell has enabled advances (Rickaby et al., 2010; Ziveri et al., 2012; Bolton & Stoll, 2013; Hermoso et al., 2014; Hermoso, 2015; Hermoso et al., 2016a; Hermoso et al., 2016b; McClelland et al., 2017), but not yet a full understanding. These culture and model studies show vital effects are influenced by parameters affecting growth conditions, including the carbonate chemistry of the growth medium, temperature and light availability (Rickaby et al., 2010; Bolton & Stoll, 2013; Hermoso et al., 2014; McClelland et al., 2017). In culture studies of carbonate chemistry, the availability of dissolved inorganic carbon (DIC) can affect both δ^{13}C and δ^{18}O at a greater rate than just temperature alone. The consensus from this culture work on extant species is that the variability and magnitude of vital effects – especially δ^{13}C - in coccolith calcite is strongly linked to available DIC in culture, and thus atmospheric pCO_2 over geological timescales (Rickaby et al., 2010; Hermoso et al., 2016a).

Not all coccolithophore species have similar vital effects, and one of the major findings of recent work is the division of coccoliths into two groups, an isotopically 'heavy' group - including *Gephyrocapsa oceanica* and *Emiliania huxleyi* - and an isotopically 'light' group – including *Calcidiscus leptoporus, Coccolithus pelagicus* and *Umbilicosphaera* spp. (Dudley et al., 1986; Ziveri et al., 2003; Bolton & Stoll, 2013; Hermoso, 2016; McClelland et al., 2017). Those in the 'heavy' group tend to be small, lightly calcifying and have a fast division rate, whereas those in the 'light' group are often large and heavily calcifying and have a slow division rate (Ziveri et al., 2003; Rickaby et al., 2010; Hermoso, 2014). In carbon isotope space this is represented by a large ($\sim$ 1 ‰) isotopic offset in the δ^{13}C of small versus large coccolithophores with correspondingly small and large coccoliths. Using size-separation methods on coccolith-rich ocean sediments, the appearance of a consistent, $\sim$ 1 ‰ offset between the δ^{13}C of large and small coccolith size fractions is documented to originate in the late Miocene to early Pliocene (7-5 Ma), and persist on into the Recent (Bolton & Stoll, 2013; Bolton et al., 2016). This change in size-specific coccolith δ^{13}C has been related to a decline in atmospheric pCO_2 previously unseen over the late Miocene (Bolton & Stoll, 2013). However, more recent studies have also noted these isotopic vital effects appearing around intervals of marked decline in pCO_2 further back in geological time, particularly accompanying the decline from a pCO_2 high in the Eocene (Claxton et al., 2022) and around the Miocene Climatic Transition (Hermoso et al., 2020). These new studies highlight that coccolith isotopic vital effects are not driven, or not driven only, by the evolution of new taxa or physiological pathways at one point in time, but rather are a response to carbon-limitation, which itself is a dynamic interplay between availability (atmospheric CO_2 and ocean DIC), uptake (transport into the cell by diffusion – controlled by cell size - or active uptake) and demand (growth and calcification rates).

The movement towards the modern large vital effects, especially in the large coccolith fraction, in the late Miocene is synchronous with major changes in climate and terrestrial plant (photosynthetic) communities. A global expansion of C_4 plants (plants

that use the C_4 photosynthetic pathway; mostly tropical grasses) relative to C_3 plants (primarily trees) occurred during this time (Cerling et al., 1997; Zhang et al., 2009). This shift in dominance has been touted as a response to decreasing pCO_2, as C_4 plants have a competitive edge over C_3 plants at low CO_2 to O_2 concentrations (Cerling et al., 1997; Zhang et al., 2009). Bolton & Stoll (2013) suggested that this showed both the marine and terrestrial realm exhibited adaptation by their primary photosynthetic communities to a common pCO_2 driver.

Modelling and culture experiments of the carbon system within the coccolithophore have attributed the large isotopic difference between small and large cells down to different strategies of carbon acquisition. Larger cells have a smaller surface area to volume ratio, which reduces the efficiency of the diffusive uptake of CO_2, making them more sensitive to CO_2 limitation. Large cells, in particular, therefore need to use carbon concentration mechanisms (CCMs), namely bicarbonate (HCO_3^-) reallocation from calcification (in the coccolith vesicle) to photosynthesis (in the chloroplast), especially under conditions of low DIC (Bolton & Stoll, 2013). Due to carbon isotopic fractionation during equilibration between DIC species, HCO_3^- is isotopically heavier than CO_2 (aq), so if more of this is being used for photosynthesis and less for calcification, then the remaining internal carbon pool that will be used for calcification is relatively depleted, leading to negative $\delta^{13}C$ coccolith values (McClelland et al., 2017). On the other hand, due to the high surface area to volume ratio of small cells, there is a greater (relative) influx of carbon into the cell by diffusive uptake, which is available for photosynthesis and reduces the need to reallocate bicarbonate away from calcification, which in turn leads to coccoliths being produced from an internal carbon pool that is isotopically heavier than that of large cells (McClelland et al., 2017). Under high CO_2 concentrations these vital effects are reduced (Rickaby et al., 2010; Hermoso et al., 2016a), indicating that the magnitude of vital effects are controlled by both the concentration of CO_2 and the coccolithophore cell size (Godbillot et al., 2022). A schematic cartoon of this isotopic fractionation in coccolithophores can be found in Fig. 1.1. When

this understanding is applied to the geological record, the study of fossil coccolith $\delta^{13}C$ can quantify these vital effects and provide information on both environmental conditions and coccolithophore cellular responses over time (Bolton & Stoll, 2013; Bolton et al., 2016).

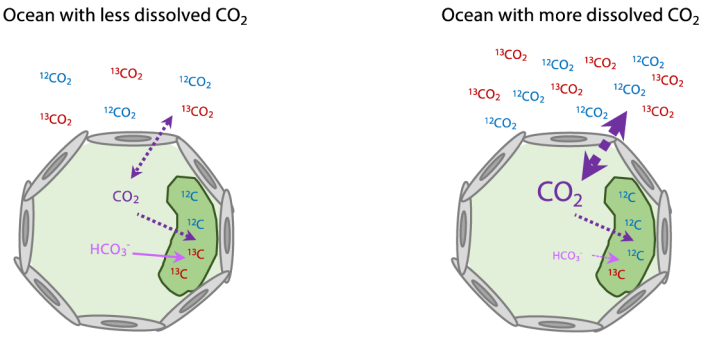


Figure 1.1: Schematic cartoon of isotope fractionation in coccolithophores, from Rae et al. (2021 (Supplementary Materials)). Cells take up dissolved CO_2 from seawater through diffusion (double-headed purple arrow). In the cell, carbon is then transported to the chloroplast (single-headed purple arrow). When CO_2 is abundant (right panel), the cell preferentially fixes ^{12}C into organic matter, and there is not as much need for the HCO_3^-, and this is also reflected in the $\delta^{13}C$ of the calcite. When the seawater is low in CO_2 (left panel), the cell needs a greater fraction of all CO_2 available, meaning that HCO_3^- is incorporated more into the chloroplast (pink arrow) than into calcification to maintain optimal photosynthesis rates (Rae et al., 2021).

Although there have been advances in understanding cellular carbon transport and fractionation, there are more uncertainties surrounding the fractionation of oxygen within the coccolithophore cell, especially during calcification. The predominant theory is that coccolith calcite in the isotopically 'heavy' group, e.g., *Emiliania huxleyi* and *Gephyrocapsa oceanica*, which are smaller and calcify at a quicker rate than larger cells, are more positive in $\delta^{18}O$ due to CO_2 rich in ^{18}O being taken in by the cell and inducing isotopic disequilibrium within the internal DIC pool (Hermoso et al., 2016b). The overall degree of equilibration between CO_2 and water molecules inside the internal DIC pool is governed by the balance of CO_2 concentrations and the degree of utilisation (Hermoso et al., 2014; 2016a; 2016b)(Fig. 1.2). At high temperatures, the magnitude of vital effects decreases (Hermoso et al., 2016b).

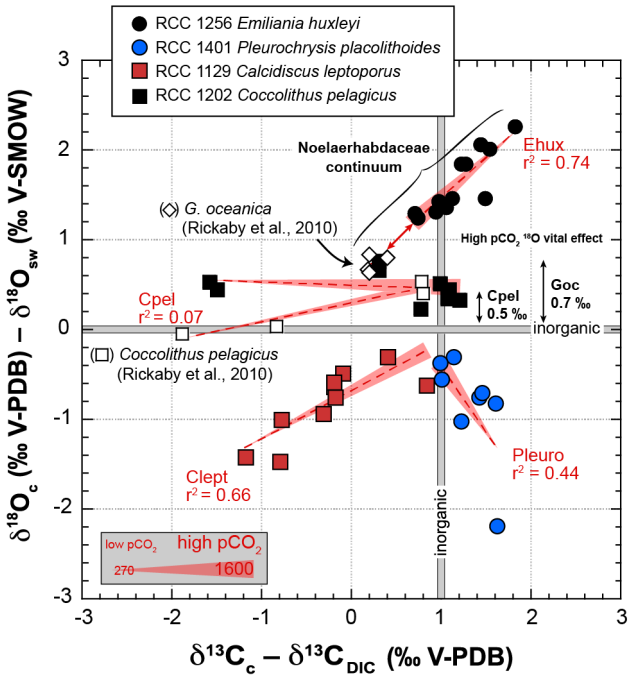


Figure 1.2: Scatter plot of carbon and oxygen isotope offsets with increased CO_2 concentration, from Hermoso et al. (2016a). With increased DIC and aqueous CO_2 concentrations (represented by the increasing red triangle on the regression line of each species), there is a decrease in magnitude of vital effects across both the $\delta^{13}C$ and $\delta^{18}O$ systems, with coccolith isotopic compositions moving towards inorganic calcite composition.

As can be seen, the physiological processes controlling isotopic fractionation within coccolithophores are complex. More work to understand coccolithophore cell physiology and how it reacts to different environmental parameters is crucial for advancement in the use of coccolith chemistry for palaeoclimate reconstructions. Such knowledge will also inform better CO_2 reconstructions using alkenone ε_p, which uses the magnitude of carbon isotopic fractionation between algal lipids produced by coccolithophores and ambient CO_2 to derive CO_2 concentrations (Pagani, 2014).

1.4 Strontium-Calcium as a productivity indicator

The Strontium-Calcium ratio (Sr/Ca) of coccolith carbonate is a well-known and developed proxy that reflects coccolithophore growth rates in culture studies (Ziveri et al., 2003), and records variations in coccolithophore production in coccolith-rich sediments

(Stoll et al., 2002b). The Sr/Ca ratio of biogenic calcite, including coccoliths, depends on the Sr/Ca of seawater and the Sr partition co-efficient into the carbonate, which in coccoliths is normally taken to be between coccolith calcite and the external growth medium (Stoll & Schrag, 2000; Stoll & Ziveri, 2004). In culture studies the coccolith Sr partition coefficient is positively related to the rate of calcification and organic carbon (C_{org}) fixation (Stoll & Schrag, 2000; Rickaby et al., 2002). The quicker that coccolithophores grow, the faster they calcify and therefore the more Sr is incorporated into the calcite of their lattice (Stoll & Schrag, 2000; Rickaby et al., 2002; Stoll et al., 2002b).

The interest in coccolith Sr/Ca ratios as a productivity indicator started with a latitudinal transect of core-top sediment analyses across the Equatorial Pacific, which found that Sr/Ca ratios varied across the transect dependent on surface ocean upwelling, with high coccolith Sr/Ca ratios coinciding with high surface productivity and high nutrient concentrations (Stoll & Schrag, 2000). This has since been supported by subsequent culture studies (Stoll et al., 2002a; Rickaby et al., 2007). Sr/Ca ratios have also been found to vary with seasonality in both sediment traps and through geological time (Stoll et al., 2007a; Cavaleiro et al., 2020). Temperature also has a minor effect on Sr/Ca ratios, following the pattern of inorganic calcite, with higher ratios at higher calcification temperatures (Müller et al., 2014; Stevenson et al., 2014).

Based on the above, coccolith Sr/Ca has also been used to reconstruct relative changes in primary productivity in the past (Waite et al., 2008), but with the limitation that coccolith Sr/Ca primarily records coccolithophore growth rates, not general surface ocean primary or export productivity. This should be remembered when discussing coccolith Sr/Ca as a general primary productivity indicator, as in many settings, especially at high-latitudes and in high-productivity areas, calcareous nannoplankton are unlikely to be the dominant primary producers (Stoll & Ziveri, 2004).

Between coccolithophore species, it has been shown that larger and more heavily calcified coccoliths generally have a higher Sr content than smaller and lighter coccoliths (Stoll et al., 2002b; Stoll et al., 2007b; Fink et al., 2010; Hermoso et al.,

2017)(Fig. 1.3). This effect needs to be considered when looking at bulk Sr/Ca, when the presence of large coccoliths could seriously alter the Sr/Ca ratio to higher concentrations, an effect that may dominate core-tope sediment records (Fink et al. 2010). Undertaking Sr/Ca analyses on specific size-fraction, rather than bulk nannofossil carbonate, is thus likely to be more informative of the nature and drivers of changes in coccolith Sr/Ca ratios.

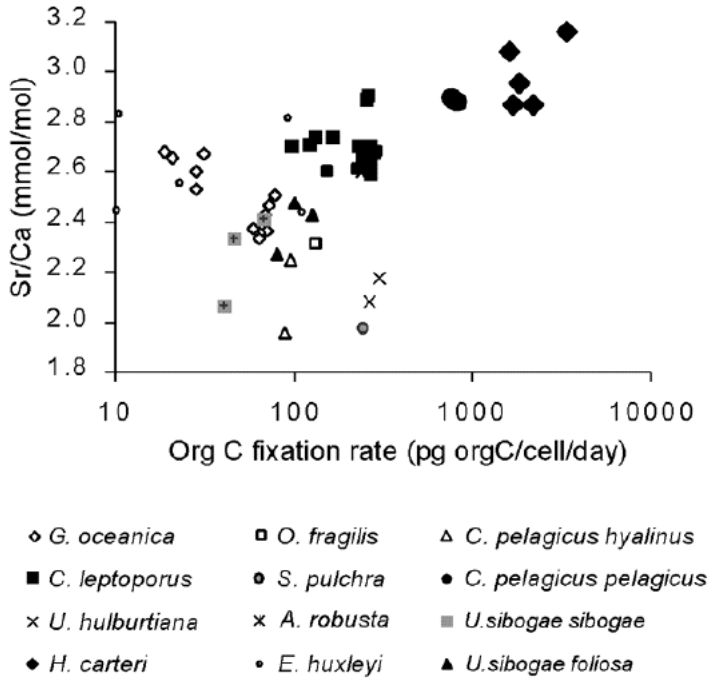


Figure 1.3: Sr/Ca ratios in cultures vs. organic carbon fixation rate estimated from cell volume and growth rates, from Stoll et al. (2002b). The larger coccoliths (e.g., *Helicosphaera carteri, Calcidiscus leptoporus, Coccolithus pelagicus pelagicus, Gephyrocapsa oceanica*) show higher Sr/Ca ratios that the smaller coccoliths (e.g., *Emiliania huxleyi, Umbilicosphaera* spp.).

Although much work has been completed on culture studies and sediment traps, Sr/Ca ratios have also been used as a measure of coccolithophore growth rates and productivity in the geological record. Most work has concentrated on the more recent past, such as the Middle Pleistocene (Cavaleiro et al., 2020), Marine Isotope Stage 11 ($\sim$424-374 kyr), (Saavedra-Pellitero et al., 2017) and the mid Pliocene (Waite et al., 2008). Some studies do go further back in time, including to the Paleocene-Eocene Thermal Maximum (Stoll et al., 2007b) and the Early Toarcian in the Jurassic

(Hermoso et al., 2009). What does need to be considered when looking at Sr/Ca ratios in deeper time is the residence time of Sr and Ca, which are thought to be relatively long; $\sim$5 myr and $\sim$1 myr respectively (Broecker & Peng, 1982). Studies of Sr/Ca variations on shorter timescales than the residence times should not be affected by changes in seawater Sr/Ca (Waite et al., 2008). However, on longer, multi-million year timescales, the changing chemistry of sea water should be taken into account (Stoll & Ziveri, 2004). Recent modelling work has suggested that the Sr/Ca has increased slowly over the past 50 myr from 8 mmol/mol to 9.4 mmol/mol, with fluctuations of $\sim$1 mmol/mol over 10 myr periods (Zhang et al., 2020).

1.5 Thesis objectives and outline

This thesis focuses on coccolith calcite geochemistry, particularly the δ^{13}C and δ^{18}O isotopic records of size separated coccoliths, and how these records can document large scale changes over a) a shorter but higher resolution (Pliocene-Pleistocene transition, 1.38-3.02 Ma); and b) a longer but lower resolution (late Miocene to Recent, 7.7-0.1 Ma). Coccolithophores exhibit vital effects, which are a record of cellular physiology imprinted on coccolith calcite. As the vital effects are due to carbon concentration mechanisms that are impacted by changing CO_2 availability, they have the potential to be an excellent record of past CO_2 changes in geological time. In this thesis, all sample material is taken from IODP Expedition 363, Site U1482 on the north-west Australian Margin.

The key objectives of this thesis are:

1. To present a novel method of coccolith size separation and determine if the method could be used for coccolith geochemistry studies.

2. To generate high-resolution coccolith chemistry data over the Pliocene-Pleistocene transition, using the novel size separation method, including isotopic signatures and trace metal analysis through orbital scale variations.

3. To analyse long term changes in the coccolith δ^{13}C and δ^{18}O signatures over the Miocene to Recent and see how long-term environmental or assemblage changes influence coccolith vital effects.

Chapter 2 is an introduction to the methods used within the thesis, including an in-depth report of a novel size separation method of the coccolith fraction (< 20 μm) and a measure of its effectiveness, by using particle image analysis. This novel method is used in the studies presented in Chapters 3 and 4.

Chapter 3 presents a high-resolution study spanning 3.02 to 1.38 million years (late Pliocene to early Pleistocene) from IODP Exp. 363, Site U1482 in the Indo-Pacific Warm Pool on the north-west Australian Margin. Samples were prepared using the novel size separation method detailed in Chapter 2. Presented within are δ^{13}C and δ^{18}O records of size separated coccoliths with an average temporal resolution of $\sim$4 kyr, showing how orbital scale variations affect these. Also presented are Sr/Ca records for the size split coccolith fraction over the same time period with a 10-20 kyr resolution to ascertain if the different size fractions have the potential to alter bulk Sr/Ca records and record any productivity changes. Assemblage analysis is presented with a resolution of 50 kyr with the aim to record the final extinction of the *Discoaster* genus and investigates changes in assemblages and how it affects the δ^{13}C and δ^{18}O records. Finally, particle size analysis is presented throughout the time period, indicating the robustness of the novel size separation method.

Chapter 4 presents the highest resolution to date study of size-separated coccolith fraction δ^{13}C and δ^{18}O records through the late Neogene (since late Miocene, 7.7 Ma to recent), prepared using the novel size separation method detailed in Chapter 2, from IODP Exp. 363, Site U1482. These δ^{13}C and δ^{18}O records are compared to reticulofenestrid size data and assemblage data from the same site to ascertain how the assemblage could affect changes in the geochemistry. Particle size analysis is presented for the time period, again documenting the success of the novel size separation method.

2 | A NOVEL SIZE SEPARATION TECHNIQUE OF THE < 20 μm FRACTION FOR USE IN COCCOLITH GEOCHEMICAL ANALYSES

My contribution to this work involved conducting all parts of the research, analysing the data, interpreting the results, writing the text and creating the figures. I also co-designed the separation methodology alongside T. Dunkley Jones. T. Dunkley Jones also provided feedback on the interpretations of results. The editorial 'we' is used here, to represent our collective viewpoint, but fully reflects the above share in contributions.

2.1 Introduction

Coccoliths are marine single-celled haptophyte algae that are the dominant calcifying phytoplankton in modern day oceans (Milliman, 1993). They are potentially an excellent record of palaeoclimate indicators, including Sr/Ca ratios indicating palaeoproductivity (Stoll et al., 2002c), and recently their carbon isotope measurements in estimates of pCO_2 concentrations in deep time (Claxton et al., 2022). Although the separation of the coccolith fraction (< 20 μm) from bulk sediment (> 20 μm) is relatively straight forward, the separation of coccolith size splits from the coccolith fraction is difficult. Different separation methods have been suggested and successfully implemented over the past few decades (Paull & Thierstein, 1987; Stoll & Ziveri, 2002; Minoletti et al., 2009; Zhang et al., 2021) but these are most often very time consuming

and can only generate relatively low stratigraphic and temporal resolution studies due to the laborious process of size-separation. These processes can be broadly split into micro-filtration (Minoletti et al., 2009) and sinking-decanting (Paull & Thierstein, 1987; Stoll & Ziveri, 2002) techniques. The former technique concentrates on passing the coccoliths through a membrane with defined pore sizes (e.g., 3, 5, 8, 10 and 12 μm). However, if there is a high amount of small (< 5 μm) coccoliths within the sediment, it can become very time consuming (Zhang et al., 2018), and the method does not work if trying to separate species in the same size category, such as the Noelaerhabdaceae and *Florisphaera profunda* (Hermoso et al., 2015). On the other hand, the sinking-decanting method is more effective on smaller coccoliths due to their size allowing for slower settling times (Zhang et al., 2018). However, this method still does not result in a perfect size split, and is also very time consuming, taking up to 1 week for a single separation. Some studies have employed a combination of both micro-filtration and sinking or centrifuging (e.g. Bolton et al., 2012; Hermoso et al., 2015) but none of these are efficient enough to process the large quantities of samples required for high-resolution studies.

More recently, there has been a move towards refining centrifugation in the separation of the coccolith fraction (Zhang et al., 2021). In that study they calculated, in theory, the trajectory of coccoliths during centrifugation and then tested this theory by conducting a size separation on a mid-Miocene sample from ODP Site 982B (Rockall Plateau, North Atlantic Ocean). The process involved suspending bulk sediment in an ammonia solution, transferring to a centrifuge tube and centrifuging down at the calculated parameters for different size categories (for full calculations see Zhang et al. (2021)). The upper 30 mL was then pumped out from each suspension, and 100 μL was dropped onto a glass coverslip, dried, and made into a slide. These steps were repeated for the different centrifuge parameters and then the slides were analysed by the measurements of coccoliths (Fig. 2.1). Whilst the method was broadly successful in separating the different size fractions, it should be noted that there is still

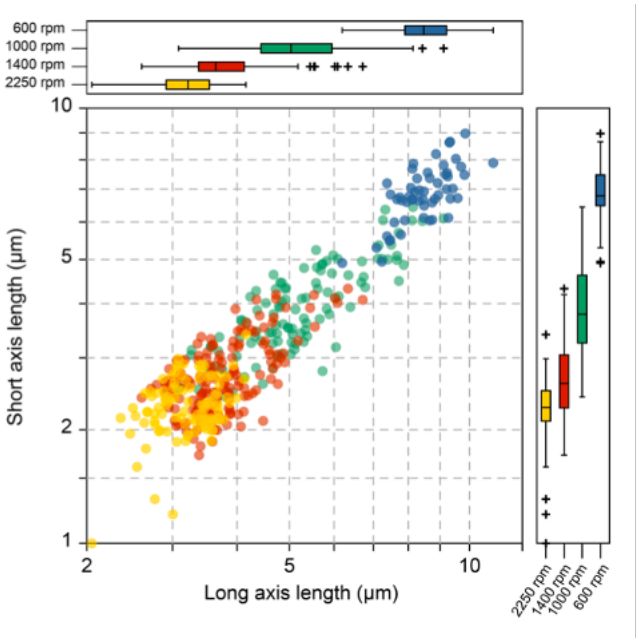


Figure 2.1: Results of coccolith size following centrifugation technique taken from Zhang et al. (2021). Yellow, red, green and blue dots represent 2250 rpm for 2 min, 1400, 1000 and 600 rpm for 1 min, respectively.

overlap between the length of the coccoliths at any given revolutions per minute (rpm). Although overlap may also happen in microfiltration and settling techniques, there appears to be a larger range using this centrifuge technique. This could be due to the pipetting technique when removing the suspended liquid or pumping close to the centrifuge wall where coccoliths may have congregated (Zhang et al, 2021). Moreover, although this method is quicker than those previously mentioned, it still requires repeated separations and repeated centrifugation for the multiple parameters, meaning it is still relatively time consuming. This method is not perfectly accurate yet yielded results that were similar to microfiltration and settling technique studies.

Here, we present a novel size separation technique based on centrifugation, where particle size analysis has been completed on samples from IODP Expedition 363, Site U1482. The technique utilised and described in this Chapter was successfully used in Chapters 2 & 3 to create the highest resolution studies on geochemistry within coccoliths over the time periods chosen.

2.2 Sample selection

The sediment samples analysed in this study were taken from IODP Expedition 363, Site U1482, on the north-west margin of Australia, at 15°3.32'S, 120°26.10'E in 1466m water depth (Rosenthal et al., 2018) (Fig. 2.2). There are 419 samples from holes A, B and C, spanning an age range from 3.02 to 1.38 million years. The average temporal resolution of this sample set is $\sim$4 kyrs, with the shortest time interval between samples of 0.8 kyrs and the largest 22 kyrs. Ages are assigned following the age model of Chen et al. (2022) which was based on a correlation of high-resolution benthic foraminiferal δ^{18}O data from U1482 to a globally stacked benthic δ^{18}O record (the Prob-stack; an updated LR04 record of Lisiecki & Raymo (2005); Ahn et al. (2017)). Samples were taken from the shipboard primary splice (Rosenthal et al. 2018), but then located on the revised splice of Lübbers et al. (2020), as adopted by Chen et al. (2022), from depths between 99.93 and 154.33 m r-CCSF-A.

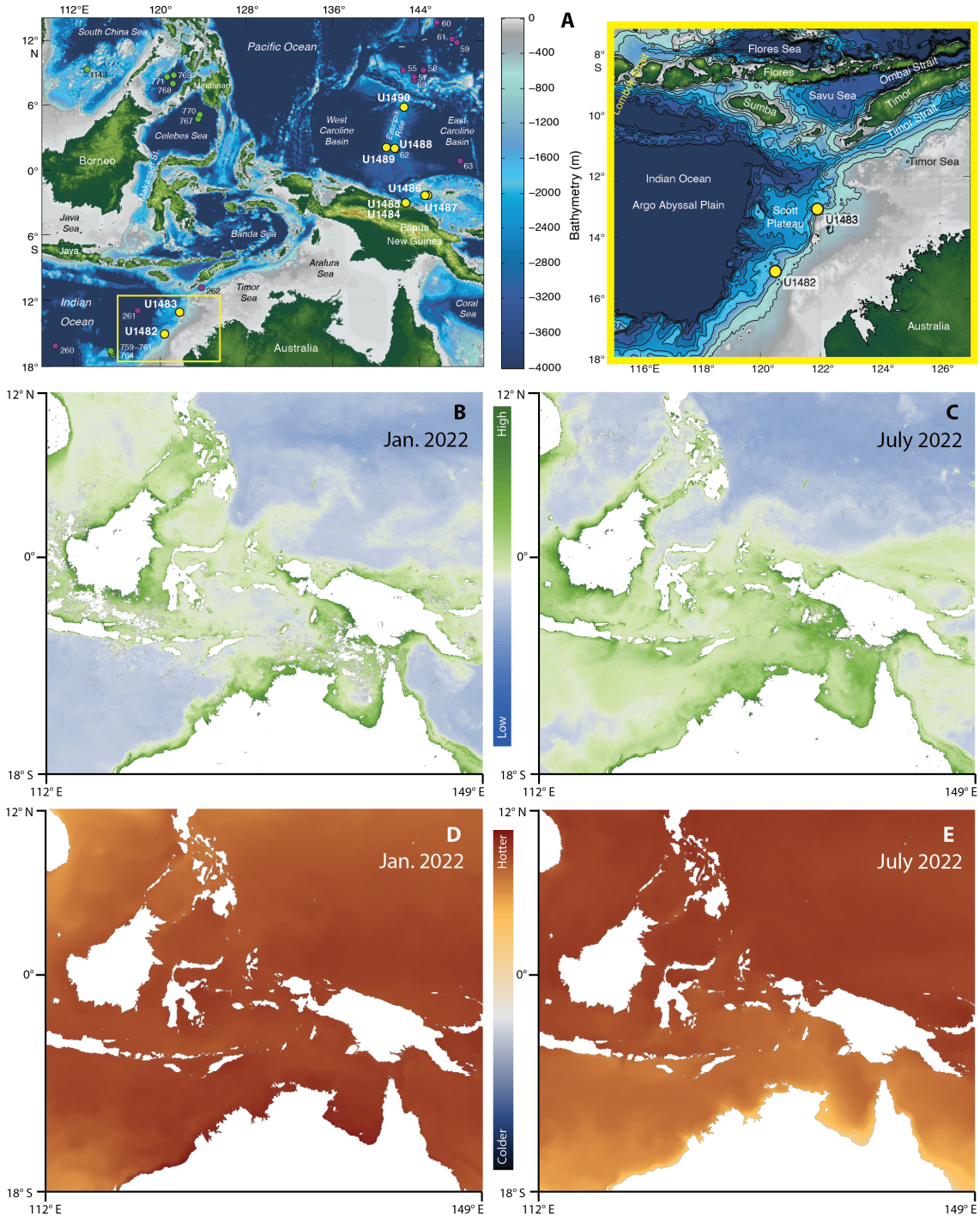


Figure 2.2: Panel A depicts bathymetric maps of both the overall area cored during Exp. 363 (right panel), with the yellow box indicating the location of Site U1482 (left panel), modified from Rosenthal et al. (2018). Panels B and C show chlorophyll concentration, where green is a high concentration, and blue is a low concentration. Panel B is for January 2022, C is for July 2022. Panels D and E show sea surface temperatures, where red is hotter, and yellow/blue is colder. panel D is for January 2022, E is for July 2022. Data for B, C, D and E from `https://www.nnvl.noaa.gov/view/globaldata.html`.

2.3 Preparation of sediments

The novel method we employed to separate the coccolith fraction from bulk sediment included 4 processes: washing, centrifuging, drying, and separating, as demonstrated in the schematic illustration (Fig. 2.3). This method was significantly quicker than those methods mentioned previously, with $\sim$420 samples being processed over a few months. The method is easily repeatable and is relatively simple, with minimal specialist equipment required.

2.3.1 *Washing*

Sediment samples (2 cc in volume) were put into a 250 mL Pyrex beaker, retaining a thumbnail size chip in the original bag for any future works. Enough DI water was added to the beaker to cover the sample, and this was allowed to soak for between 30 minutes and 1 hour to aid disaggregation. All sieves used within this process were Endecotts Laboratory Test Sieves. The samples were then washed through an 63 μm sieve using DI water until the water ran clear, collecting the < 63 μm fraction in suspension in a 1L glass beaker and discarding the > 63 μm fraction. The < 63 μm fraction was then washed again with DI water through a 20 μm sieve until clear, collecting the < 20 μm fraction in suspension and discarding the > 20μm fraction. The < 20 μm fraction in suspension was then transferred to 50 mL Falcon Centrifuge Tubes (multiple per sample). Sieves were thoroughly cleaned with DI water and placed within a Grant Ultrasonic Bath for 30 seconds at 42 kHz frequency between washing.

2.3.2 *Centrifuging*

The Falcon Centrifuge Tubes were placed into a Mistral 1000 Centrifuge and spun down for 6 minutes at 4000 rpm. Once the cycle was completed, the clarity of the water was checked. With the sediment slightly solidified occupying the bottom of the centrifuge, the water was poured off from the centrifuge tube until approximately < 0.5

cm of water was left on top of the sediment, to not disturb the top layer of centrifuged material. As there were multiple centrifuge tubes per sample (i.e., more than 50 mL of suspended solution was collected per sample), these were then combined into one final centrifuge tube per sample, DI water was added and the combined sediment was mixed with the DI water, creating a suspended solution again. This was then centrifuged one final time for 8 minutes at 4000 rpm and the water was poured off again, leaving < 0.5 cm to not disturb the sediment.

2.3.3 *Drying*

Two methods of drying were trialled for these samples; freeze drying and oven drying, with the latter being employed for most of the samples due to issues with the freeze-dried samples. Freeze drying involved placing the centrifuge tubes in a test tube holder to keep in an upright position and then opening the tubes. These were then placed in a freeze dryer for 24-48 hours until the sample was thoroughly dry. Although this method did lead to dry samples, it led to problems with the separation of the different size fractions (see next section). Therefore, oven drying within a Genlab Drying Cabinet was implemented. For this method the centrifuge tubes were placed into a test tube holder to maintain an upright position and were placed in the oven with the lids of the tubes off. The tubes were then left to dry in a Genlab Drying Cabinet at 50℃ overnight. When the sample was dry, it was a broadly triangular bullet-shaped piece of coccolith-fraction sediment, shaped by the form of the bottom of the centrifuge tube.

2.3.4 *Separating*

Upon beginning the separation process, the bullet shaped coccolith fraction was gently taken out of the centrifuge tube and placed on a piece of filter paper to aid transfer to 7 mL glass vials. Four glass vials were labelled with the targeted size fractions: very fine, fine, medium, and very coarse (VF, F, M and VC respectively). The bullet shaped sample was then split using a metal scalpel into these 4 categories. There

is a colour and texture change across the size fractions; the VF fraction is quite consolidated and a darker grey, whereas the VC fraction is more friable and a white grey. As these end members were what was being used for the isotope and trace metal analysis, the distinction between these two was easy to make as they come from the top (VF) and bottom (VC) of the centrifuge pellet. The different size fractions were then transferred to the labelled glass vials and the material was gently separated back into a powder within the vials. As mentioned above, the freeze-drying method led to problems when separating. When freeze dried, the bullet of coccolith fraction was very friable and would break apart and mix easily, meaning an accurate separation could not be completed. Hence, the oven drying method was preferred in this instance.

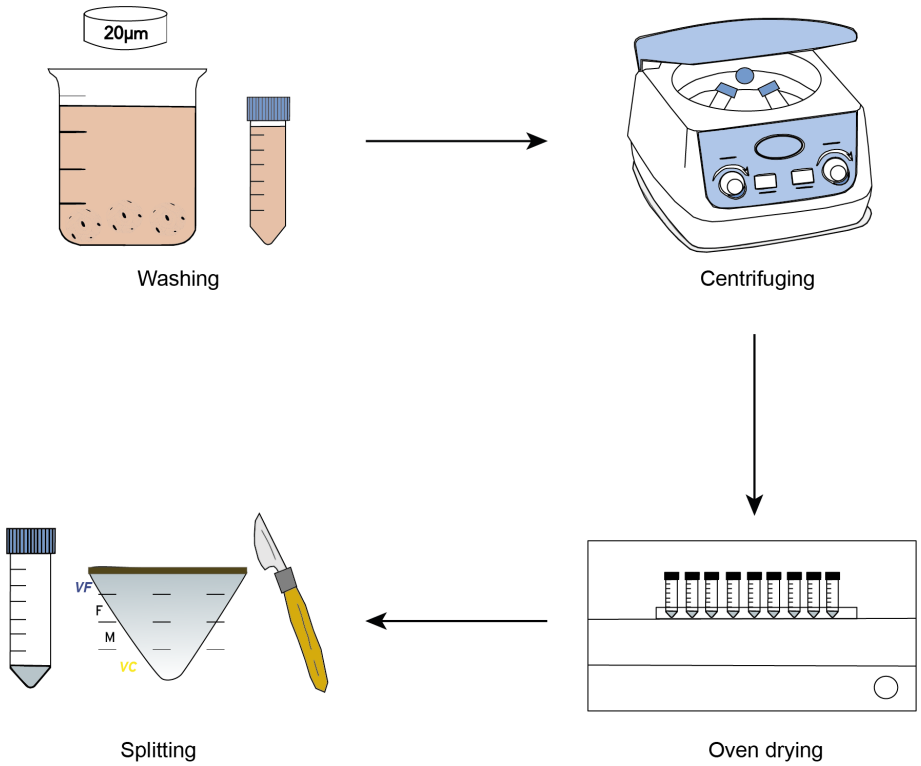


Figure 2.3: Schematic illustration of the method used within this study for splitting samples: washing, centrifuging, oven drying and splitting.

2.4 Particle size analysis

Following on from the novel separation method described above, it was necessary to ensure that the separation worked and characterised the coccolith size distribution. In previous studies of separation techniques, the rigorous, quantitative assessment of coccolith size distributions is rare, occurring only in a small amount of studies (e.g. Stoll & Ziveri, 2002; Zhang et al., 2021), with most relying on SEM images of the size fraction to demonstrate the separation quality (e.g. Hermoso et al., 2015).

2.4.1 *Slide settling technique*

Seventy slides (35 VF and 35 VC) were prepared following the settling technique of Flores & Sierro (1997). This technique was chosen to prepare the slides because of the need for particles to be dispersed and to avoid contacting particles that are difficult or impossible to separate in particle size distribution analyses.

Between 11 and 13 mg of the size-fraction material was transferred to a 10.5 mL glass sample vial. Buffered water solution consisting of 0.15 g/L of sodium carbonate, 0.2 g/L of sodium bicarbonate and 0.08 g/L of gelatin mixed in DI water was added. These vials were then ultrasonically treated for 2 minutes in a Grant Ultrasonic Bath at 42 kHz frequency. Cover slips were then placed on the bottom of glass petri dishes and a mixture of buffered water and gelatin was added. The solution in the glass vials was shaken to resuspend thoroughly and after 2 minutes, 75 μL of this solution was extracted using a micropipette and dropped into the petri dish with the cover slip. The solution was then gently pumped using the micropipette around the petri dish to gain a uniform distribution over the cover slip and then allowed to settle overnight. Excess water was then carefully siphoned off using strips of tissue and the cover slip allowed to air dry, before being fixed onto a glass slide with Norland Optical Adhesive.

2.4.2 *Microscope imaging & image processing*

These slide samples were analysed using a Zeiss AxioScope A.1 at 1000x magnification with circular polarisation, and a Märzhäuser Wetzlar motorised XYZ stage. After focusing, a continuous 20 to 30 fields of view were imaged using a QI Imaging camera. Microvision Cartograph software was used at the same time, automatically capturing and stitching sequential image tiles into one image. The total area of the exported image was 0.12 mm^2 or 0.18 mm^2, for the 20 and 30 tile images respectively.

Tiled images were processed using Fiji (Schindelin et al., 2012), a version of the open-source ImageJ that focuses on biological-image analysis and facilitates particle size distribution analysis.

The image firstly needed to be converted to an 8-bit greyscale image, as the particle analysis and thresholding steps will not work with a colour image. A spatial scale for the images also needed to be defined. The image taken using Microvision Cartograph software uses pixels as its standard measurement, with slides scanned at a scale of 0.03458 μm/pixel at 1000x magnification. This was input in the image properties in Fiji using microns as the units.

Thresholding detection was then set using the greyscale image, to distinguish the objects of interest (non-black pixels) from the background (black pixels). There are some automated threshold determinations available in Fiji but these did not work well across all images. Instead, thresholds were set using the histograms that are output from Fiji (Fig. 2.4). If a threshold is chosen that is too low and does not encompass the left-hand side of the histogram, then particles can become merged, meaning the area would be artificially large. If the threshold is too high and goes past the upper limit of the histogram (the right-hand side), then there are less detections of 'interesting' particles, artificially removing the smaller particles. A threshold that encompassed the whole histogram curve was chosen to be consistent throughout the samples.

Once the threshold had been set, a binary image was produced, highlighting the particles (in white) from the background (black) (Fig. 2.5). Following on from these

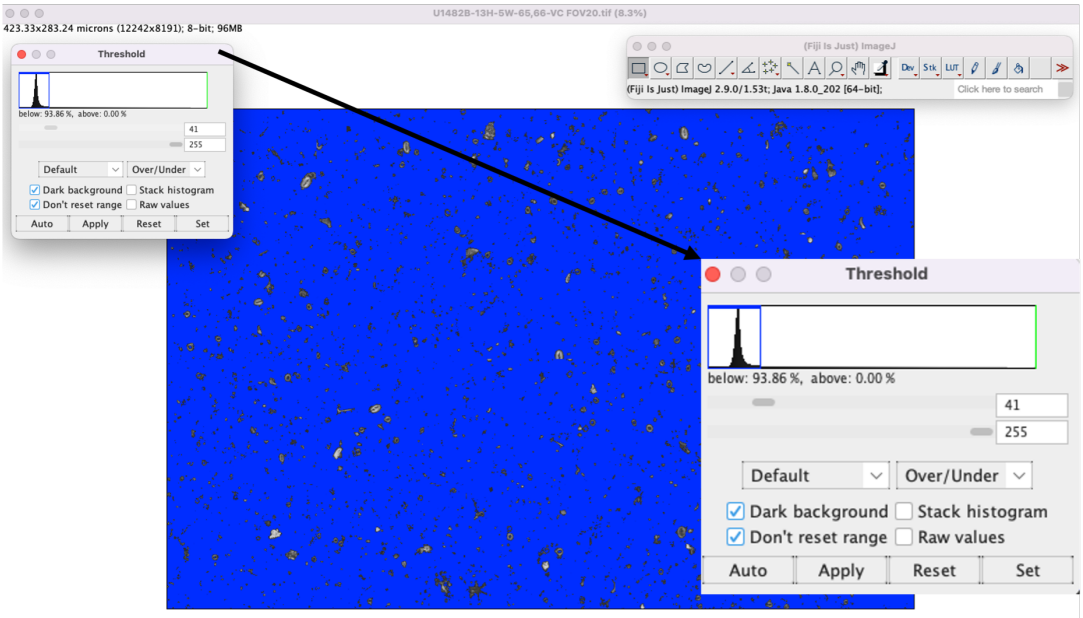


Figure 2.4: Screenshot of the Fiji software (Schindelin et al., 2012) and the thresholding process. As can be seen on the histogram, there is an upper limit, and the threshold was chosen to be there due to it encompassing the whole histogram, so all the 'interesting' particles are captured.

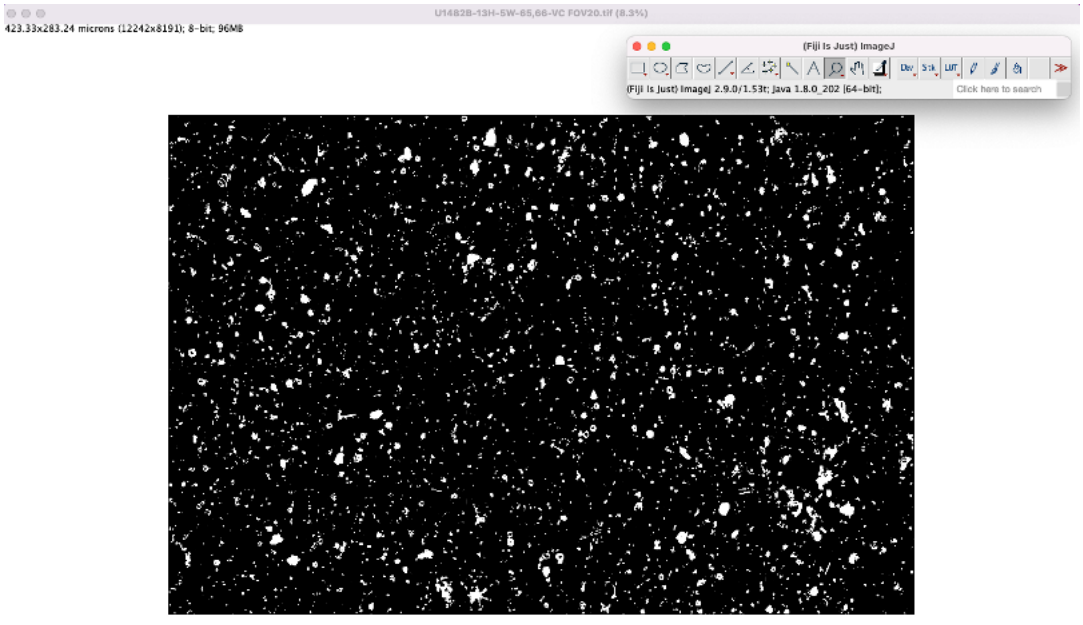


Figure 2.5: Screenshot of the Fiji software (Schindelin et al., 2012). This is the binary image produced after setting the threshold. It is the image that particle analysis will be performed on.

processes, the particle size distribution analysis was chosen from the the analysis menu. Anything with an area larger than 80 μm^2 or less than 1 μm^2 were disregarded

due to the limits of resolving minute coccolith particles with light microscopy (lower bound), and due to the unlikely occurrence of very large coccoliths in this material (upper bound), that makes very large particles more likely to be other biogenic carbonate fragments. For each particle, an area is determined as the total area within the particle margin, including any holes. There is an option for hole detection and exclusion within ImageJ, but for this analysis – based on coccolith size - we consider the total coccolith particle area, including any central area 'hole'. For calcification analyses, hole detection would be required. We also included the full range of circularity that could be measured (0.00-1.00) as there are a wide variety of coccolith shapes, and most are not perfectly circular. The output of running this analysis is an image that has each particle picked out, selected and numbered (Fig. 2.6), and a .csv file that contains the numerical information, i.e., each labelled particle and its total area.

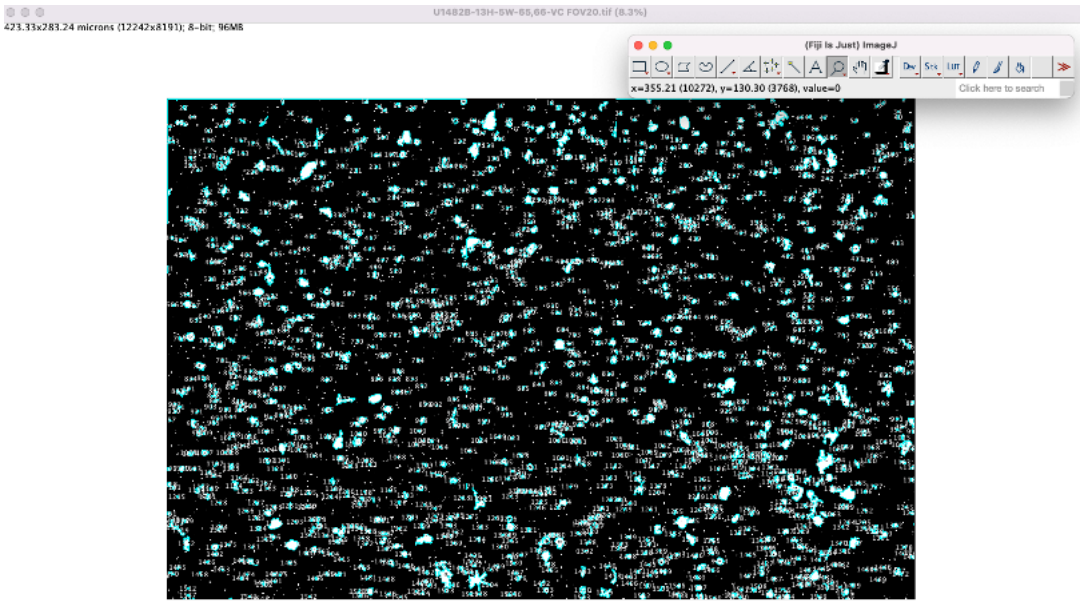


Figure 2.6: Screenshot of Fiji software (Schindelin et al., 2012). This is the image output of the particle analysis measurement, where all the particles are assigned a label.

2.5 Results

Sixty-two (31 VF, 31 VC) were deemed suitable for particle size analysis. Some slides were excluded because of an artifact during slide preparation. This produced a frosted effect on some of them, meaning particles could not be distinguished or they were artificially recorded with a significantly larger area than that of the underlying nannofossil particle distributions (Fig. 2.7). The average area of all VF fractions measured was 3.28 μm^2, with a range from 1.96 μm^2 to 5.48 μm^2. The average area of all VC fraction measured was 5.79 μm^2, with a range from 3.64 μm^2 to 11.44 μm^2 (Fig. 2.8). In all cases the VF fraction showed a markedly lower average particle size than the corresponding VC fraction, demonstrating that the underlying centrifuge methodology is an efficient size separation protocol.

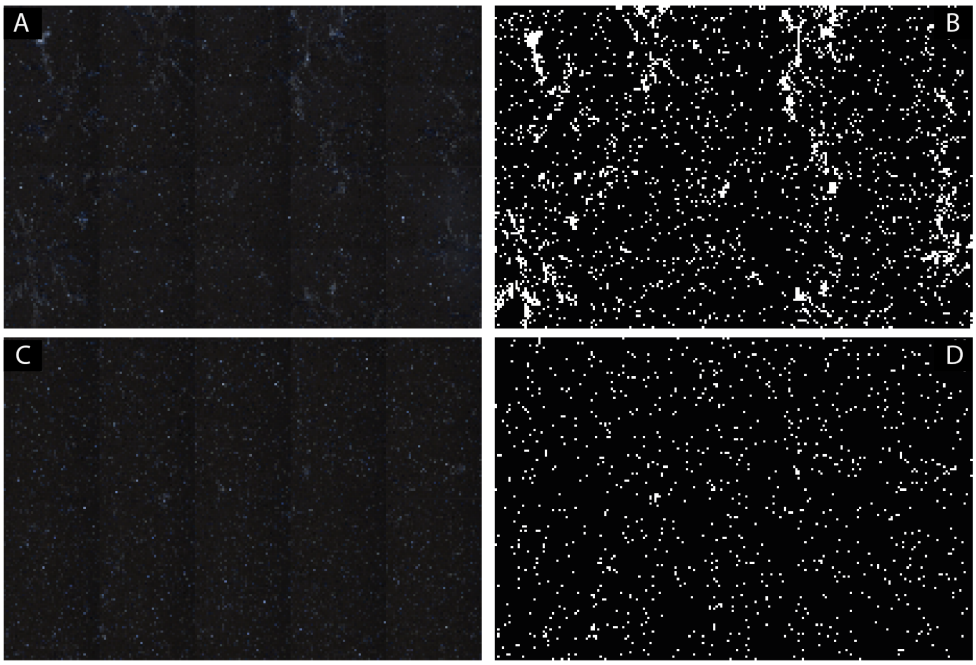


Figure 2.7: Examples of 'good' vs. 'bad' images and the thresholds that were set. A & B - U1482B 14H 2W 123/124, VF fraction. A is a circular polarised image; B is the threshold that was set using Fiji to distinguish the particles. The frosted effect and any light issues were picked up on, making the image/slide unusable. C & D – U1482B 12H 2W 52/53, VF fraction. C is a circular polarised image; D is the threshold that was set using Fiji to distinguish the particles. This is an example of a good image, as the particles are all individual and there is no frosted effect.

Similar to Zhang et al. (2021), there was some overlap between the total range of average particle size values, for the VF and VC fractions, across all samples analysed (Fig. 2.8). However, it is important to note that for all samples, the average size of the VC fraction was always greater than that of the VF fraction from the same sample. The overlap of the VF and VC average values through all samples analysed therefore reflects variations in the underlying particle size distribution through time, rather than a failure in the separation protocol for any sample.

The centrifugation method is inherently not a method that perfectly distinguishes all particles based on size thresholds, rather it relies on the more rapid settling of larger particles during centrifuging. The final particle size distribution of the layers of particles collected at the base of the centrifuge tube in this method depends on both the settling velocity of particles but also on their original distance to the centrifuge tube base or sediment surface as it accumulates in the base of the tube. Small particles near the base of the centrifuge tube, even with a lower settling velocity, are still likely to be admixed with larger particles that have settled out of the whole suspension, because they have less far to travel. This process results in a preferential distribution of larger coccoliths towards the base of the settled sediment, and of smaller coccoliths towards the top, but this is not perfect. However, when combined with full characterisation of the particle distribution of both fractions, and size normalisation on this basis, a perfect separation is not required.

The cumulative frequency distribution of particle size was established for the VF and VC fraction of each sample (Fig. 2.9). On the plots with only one cumulative frequency trend, for one size split, this is because the other size split was not measured due to poor slide quality. Apart from 2 samples (U1482B 12H 6W 37/38 and U1482A 14H 5W 143/144), the VC fraction is made up of larger particles. This could be due to a presence of anomalously large particles in the VF fraction that do not follow the shape of the rest of the distributions seen. These samples contain aggregates of small coccoliths that have clumped into larger particles in the VF fraction. It is important

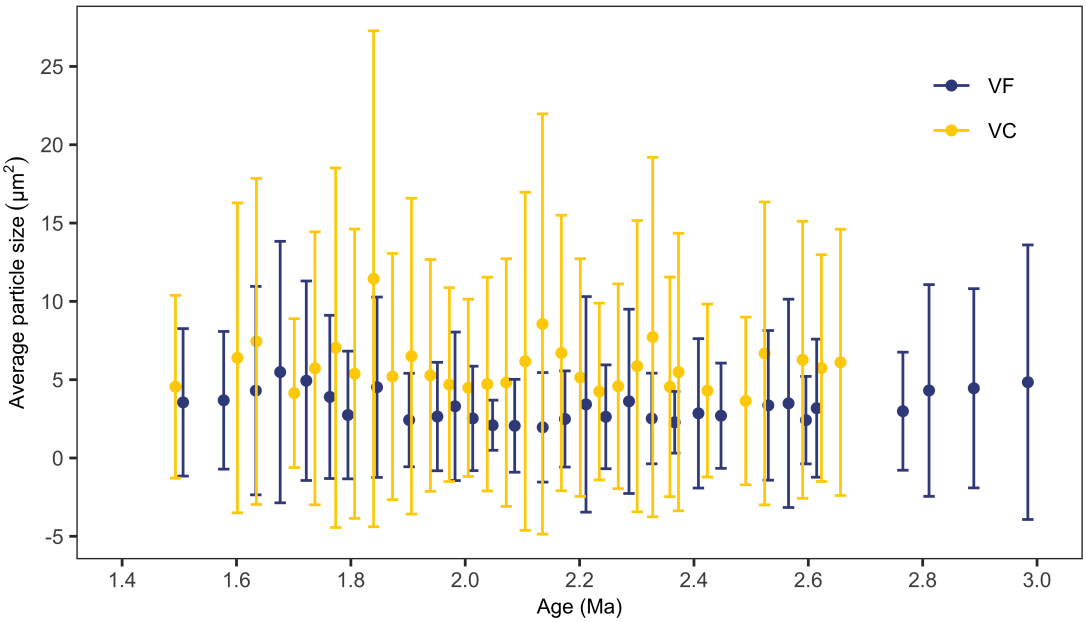
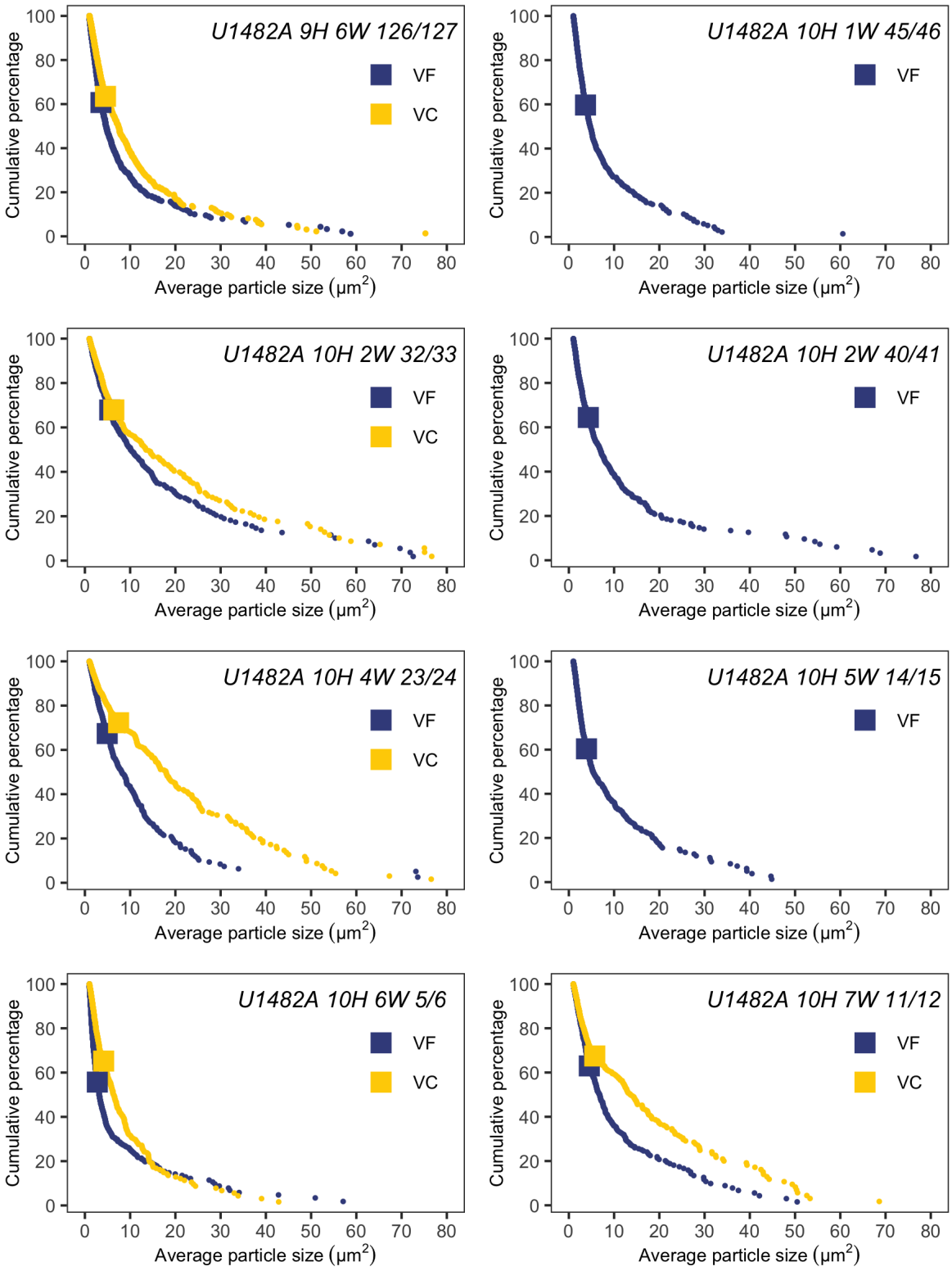
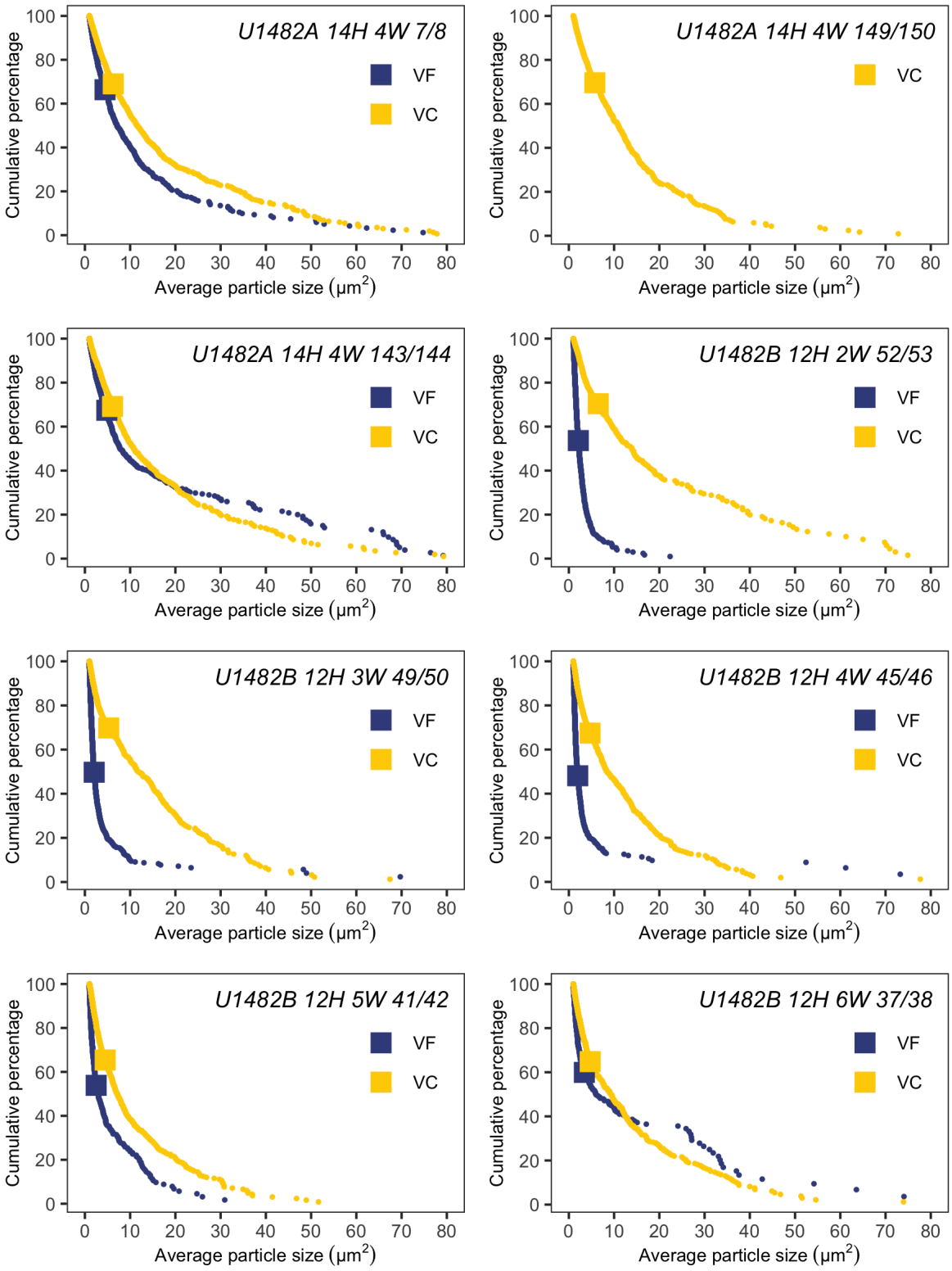
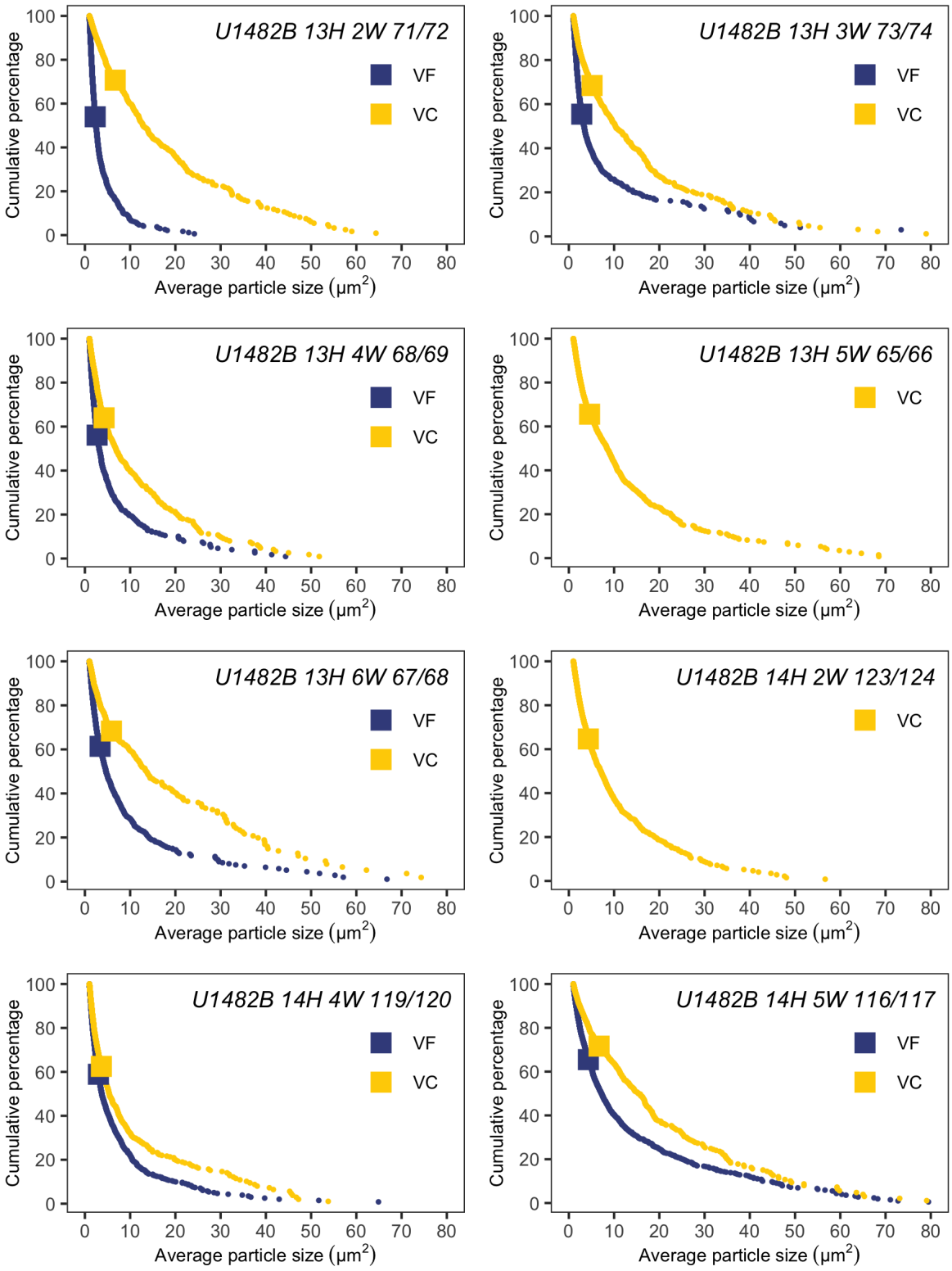


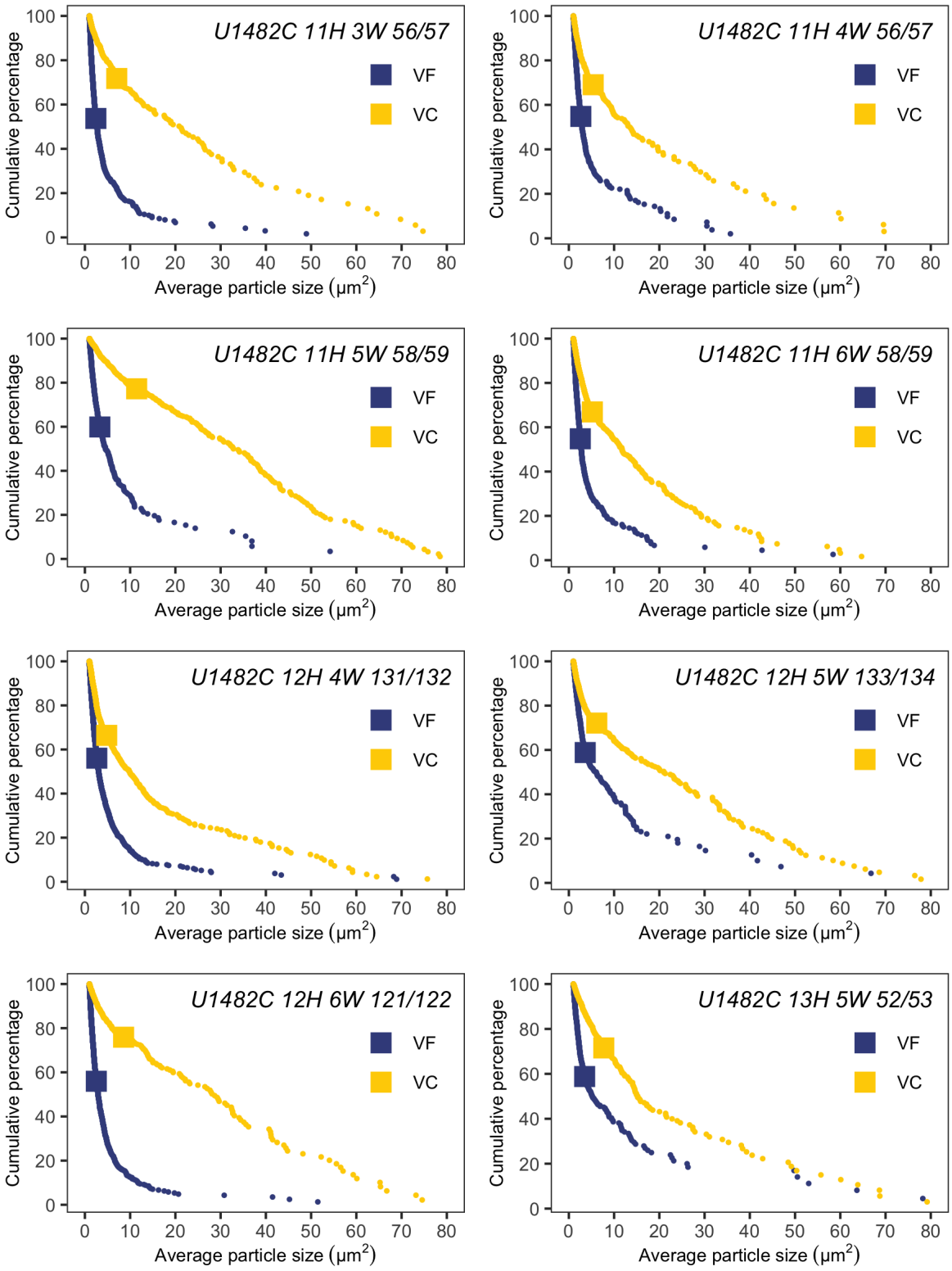
Figure 2.8: Average area of particle (μm^2) against age of sample along with the standard deviation. The blue is the VF fraction, the yellow is the VC fraction. As can be seen, the VC fraction consistently plots larger average particle size areas than the VF fraction.

to note that despite these anomalous cumulative frequency results, although the VC fraction is where larger particles are more often seen, they do not necessarily make up a numerically dominant portion of the particles, but their size constitutes the majority of the mass (discussed in Chapter 3).


U1482A 9H 6W 126/127
U1482A 10H 1W 45/46
U1482A 10H 2W 32/33
U1482A 10H 2W 40/41
U1482A 10H 4W 23/24
U1482A 10H 5W 14/15
U1482A 10H 6W 5/6
U1482A 10H 7W 11/12
VF
VC
Cumulative percentage
Average particle size (µm²)
0
20
40
60
80
100
0
10
20
30
40
50
60
70
80


U1482A 14H 4W 7/8
VF
VC
U1482A 14H 4W 149/150
VC
U1482A 14H 4W 143/144
VF
VC
U1482B 12H 2W 52/53
VF
VC
U1482B 12H 3W 49/50
VF
VC
U1482B 12H 4W 45/46
VF
VC
U1482B 12H 5W 41/42
VF
VC
U1482B 12H 6W 37/38
VF
VC
Cumulative percentage
Average particle size (µm²)
0
10
20
30
40
50
60
70
80
100


U1482B 13H 2W 71/72
U1482B 13H 3W 73/74
U1482B 13H 4W 68/69
U1482B 13H 5W 65/66
U1482B 13H 6W 67/68
U1482B 14H 2W 123/124
U1482B 14H 4W 119/120
U1482B 14H 5W 116/117
VF
VC
Cumulative percentage
Average particle size (µm²)
0
20
40
60
80
100
0
10
20
30
40
50
60
70
80


U1482C 11H 3W 56/57
U1482C 11H 4W 56/57
U1482C 11H 5W 58/59
U1482C 11H 6W 58/59
U1482C 12H 4W 131/132
U1482C 12H 5W 133/134
U1482C 12H 6W 121/122
U1482C 13H 5W 52/53
VF
VC
Cumulative percentage
Average particle size (µm²)
0
10
20
30
40
50
60
70
80
100

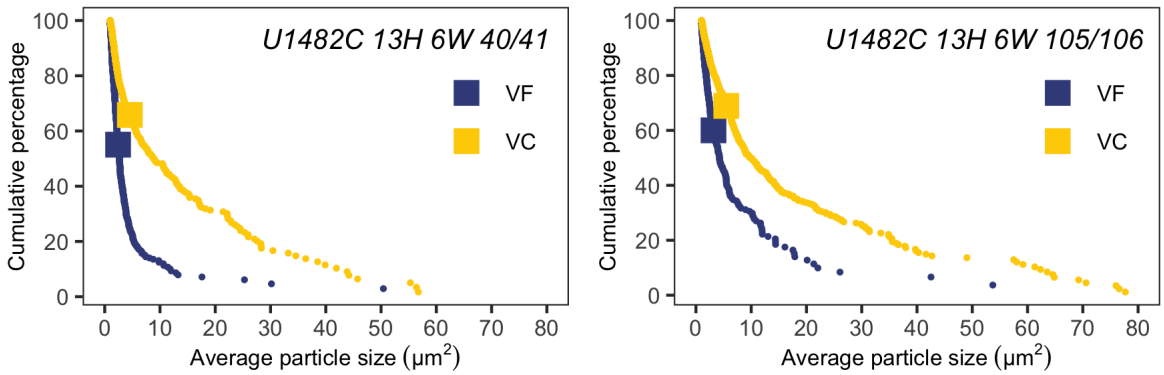


Figure 2.9: Cumulative percentage plots for each sample alongside the average particle size (μm^2). Blue is the very fine fraction, yellow is the very coarse fraction. As mentioned previously, the VC fraction mostly has a larger cumulative percentage of the larger sized particles, apart from two samples. The explanation is given in section 2.4.4, Particle size analysis results.

2.6 Conclusion

The novel size separation technique presented in this Chapter is a step towards a greater proportion of high-resolution studies of coccoliths, whether that be stable isotope, trace metal or assemblage analyses. We showed that the protocol was successful through particle size analysis, showing a consistently larger area of particles in the VC fraction when compared to the VF fraction. The previous methods often used in the community are time consuming and laborious, whereas the novel method presented is comparatively less time consuming. The stable isotope and trace metal analysis presented in Chapters 3 and 4 of this thesis is confirmation that the method is a step in the right direction.

3 | NOVEL APPROACHES TO HIGH-RESOLUTION COCCOLITH GEOCHEMISTRY OVER THE PLIOCENE-PLEISTOCENE TRANSITION

My contribution to this work involved the preparation of the samples for analysis, the nannofossil assemblage analysis, the interpretation of the results, writing the text and creating the figures. The methodology is the same as that described in Chapter 2, which I co-designed with T. Dunkley Jones. Stable isotope analysis was conducted at the British Geological Survey, Keyworth, UK, by M. Leng. Trace metal analysis was conducted at the University of Cardiff, UK, by C. Lear and S. Slater. Planktic foraminifera carbon isotope results were provided by J. Liu. T. Dunkley Jones provided feedback on the the research design and interpretation of the results. As in previous chapters, the editorial 'we' is used to reflect these proportional contributions.

3.1 Introduction

The mid Pliocene to early Pleistocene is a period of change that has been extensively studied in the search for future climate analogues under elevated atmospheric CO_2 concentrations (Burke et al., 2018). Attention has especially focused on the Mid-Piacenzian Warm Period, within the Pliocene (mPWP; 3.264-3.025 Ma, (Haywood et al., 2013; Haywood et al., 2016)), as the most recent period with comparable CO_2 mea-

surements to today (in excess of 400 ppm) (Pagani et al., 2010) and surface temperatures 1.8℃ to 3.6℃ warmer than pre-industrial temperatures (Haywood et al., 2013). Under the Representative Concentration Pathway 8.5 (RCP 8.5), where greenhouse gas emissions are left to grow unmitigated, by 2030 future climates will resemble mid-Pliocene climates (Burke et al., 2018). More recent work has suggested that with the current rates of CO_2 increase, mPWP values will be surpassed by 2024/2025, meaning levels of atmospheric CO_2 will be the highest they have been for 3.3 million years (De La Vega et al., 2020). As well as the focus on the narrow mPWP "warm climate" analogue, the subsequent progressive cooling into the late Pleistocene provides information on the coupled dynamics of Antarctic and incipient northern hemisphere ice sheets to orbital variability and declining atmospheric CO_2. As modern ice sheets retreat, the Earth's climate state has a combination of components from across this time interval – mid-Pliocene like greenhouse gas forcing, with progressively early Pleistocene to late Pliocene ice sheet configurations (Hill et al., 2017; Colleoni et al., 2022; Wilson et al., 2022). It is this interval that this study targets to document the responses of the tropical phytoplankton to progressively increasing carbon limitation, combined with orbitally-driven dynamics, ice volume and ocean circulation nutrient dynamics.

The transition from the mid Pliocene to the late Pleistocene signalled a change from a relatively warm Earth with restricted Antarctic ice sheets to a much cooler global climate with extensive ice sheets at both poles and an increased latitudinal temperature gradient (Zachos et al., 2001; Ravelo et al., 2004; Lisiecki & Raymo, 2005; Raymo et al., 2006; Westerhold et al., 2020). This climatic variability has been extensively studied, largely by geochemical analyses of benthic and planktic foraminifera. Benthic foraminiferal oxygen isotope compositions ($\delta^{18}O$) - representing a combination of deep ocean temperature and global ice volume - show a rapid movement to more positive values 4 million years ago (Ma) associated with the movement to a cooler climate (Zachos et al., 2001; Westerhold et al., 2020). The climate became much more variable in the Pleistocene than the Pliocene due to high-amplitude glacial-interglacial temper-

ature differences (Ravelo et al., 2004; Lisiecki & Raymo, 2005).

Although the study of Pliocene climate has been reconstructed from a global spread, high resolution studies in temporal space are limited and concentrate on key periods (Groeneveld et al., 2014). One of these is Marine Isotope Stage (MIS) M2, a significant glaciation event within the late Pliocene that interrupted the warm period with an isolated cold stage at 3.3 Ma (De Vleeschouwer et al., 2018; Kirby et al., 2020; Westerhold et al., 2020), and marked the transition from a Coolhouse state to an Icehouse state (Westerhold et al., 2020). There was a marked increase in benthic δ^{18}O over this period (Lisiecki & Raymo, 2005; De Schepper et al., 2014; Westerhold et al., 2020) and was accompanied by a transition from occasional, local glaciers to a more modern Northern Hemisphere ice configuration (De Schepper et al., 2014). The mPWP is also a key period of study (Dowsett et al., 2013; Haywood et al., 2013; Haywood et al., 2016; Burke et al., 2018; De La Vega et al., 2020), as well as between MIS 95-100; the first glacial/interglacial cycles after the intensification of the Northern Hemisphere Glaciation (Bolton et al., 2010; Naafs et al., 2010; Bailey et al., 2013; Hennissen et al., 2014). These glacial periods are marked by increases in the benthic δ^{18}O over this period, as clearly seen in the LR04 stack (Lisiecki & Raymo, 2005).

The onset of Northern Hemisphere Glaciation (NHG) 3.6 million years ago was seen in the benthic δ^{18}O record as an increase in values, indicating the build-up of ice sheets in the Northern Hemisphere (Mudelsee & Raymo, 2005). The subsequent intensification of the NHG (iNHG) at 2.7 Ma (Ruggieri et al., 2009) is a key period of study over the Pliocene, where the 41kyr world of glacial-interglacial cycles was amplified. Sea surface temperatures (SSTs) record a global cooling trend following the warm Pliocene (Etourneau et al., 2009; Etourneau et al., 2010; Lawrence et al., 2010; Naafs et al., 2010; Venti et al., 2013). Variability in benthic δ^{18}O also increased (Lisiecki & Raymo, 2005), indicating that orbital forcing was having a stronger influence on the climate system (Willeit et al., 2015). Major ice sheets over land in the Northern Hemisphere are supported by a sudden increase in ice-rafted debris at many

locations, including the North Atlantic (Bailey et al., 2013). The cause of this intensification is still under debate, with many mechanisms suggested. This includes tectonic rearrangements, such as the emergence of the Panama Isthmus (Keigwin, 1982), uplift and erosion of the Tibetan-Himalayan plateau (Raymo, 1994), or the restriction of the Indonesian Seaway (Cane & Molnar, 2001). Intensified Atlantic meridional overturning circulation (Hayashi et al., 2020) or the presence of permanent El Niño conditions prior to the iNHG could have inhibited glaciation (Wara et al., 2005; Fedorov et al., 2006). The most accepted explanation is a decline in atmospheric CO_2 concentrations at this time (Lunt et al., 2008; Seki et al., 2010; Willeit et al., 2015), with other mechanisms playing a minor role (Lunt et al., 2008).

CO_2 is thought to have had a major control on environmental change throughout Earth's history. Most CO_2 reconstructions are done with boron isotopes ($\delta^{11}B$) in planktic foraminifera or carbon isotopes in alkenone measurements. A recent compilation of CO_2 reconstructions over the past 66 million years using these two methods found close coupling between CO_2 and climate (Rae et al., 2021). The Pliocene and Pleistocene have been the subject of numerous studies. There seems to be a slight rise in CO_2 during the mPWP, ranging from 394 to 330 ppm (De La Vega et al., 2020), from a relatively stable Pliocene world of 270±40 ppm (Badger et al., 2013). CO_2 then falls again as the Icehouse state intensifies, with glacial maxima being associated with increased variability of CO_2 and a more gradual decline in interglacial periods (Honisch et al., 2009; Chalk et al., 2017; Dyez et al., 2018). However, in times of low pCO_2, there is a muted response in alkenone pCO_2 records in comparison to $\delta^{11}B$ pCO_2 records, suggesting caution needs to be taken in the interpretation of alkenone records in low pCO_2 (Badger et al., 2013; Badger et al., 2019).

There are arguments for permanent El Niño conditions in the Pacific Ocean during the Pliocene (Wara et al., 2005; Ravelo et al., 2006; Etourneau et al., 2010), with widespread impacts on tropical ocean-atmosphere dynamics across the planet (Haywood et al., 2007). These arguments are based on reconstructions of a reduced

east-to-west asymmetry of sea surface temperatures and thermocline depths in the early Pliocene relative to the modern (e.g. Wara et al., 2005; Ford et al., 2015; Jakob et al., 2017; Beltran et al., 2019). This east-to-west difference in SST was only ∼1.5℃ in the warm Pliocene and increased to 5℃ after 1.7 Ma (Ravelo et al., 2006). The thermocline of the eastern Pacific was deep in the warm Pliocene (Wara et al., 2005). In the early Pleistocene, SSTs show an increase in global latitudinal and Pacific east-west temperature gradients between 2.2 and 1.8 Ma, indicating that the Walker and Hadley circulation was strengthening (Ravelo et al., 2004; Wara et al., 2005; Etourneau et al., 2010). This intensification of the Walker circulation has also been touted for driving the aridification of the African continent (Van Der Lubbe et al., 2021).

The Indonesian Throughflow (ITF) is a crucial link in transporting warm waters from the Indo-Pacific Warm Pool (IPWP) to the Indian Ocean (De Vleeschouwer et al., 2019) (Fig. 3.1), and serves as a source for multiple currents around Australia and in the Indian Ocean, including the Leeuwin Current (LC). The ITF has been through periods of restriction, and this has been mapped through changes in the LC. De Vleeschouwer et al. (2019) showed that a tectonic ITF reorganisation at 3.7 Ma permanently reduced the LC, as the timing coincides with collision of the Banda volcanic arc with the Australian margin (Hall, 2009). The ITF also decreased at 3.3 Ma, at the same time as the MIS M2 glaciation event, where it reduced the LC current but it did not fully disappear (De Vleeschouwer et al., 2018). On the Australian continent, there was a movement from dry to humid conditions across north-west Australia at 5.5 Ma, lasting for 2.2 million years (Christensen et al., 2017). Precipitation was likely year round, with humidity reducing gradually from 3.3 to ∼2.4 Ma, before switching to an arid interval and being more like the modern Australian monsoon system we see today, indicating a major change in Indian Ocean circulation during this time (Christensen et al., 2017). Overall, in the early Pliocene, the ITF is unbound by any tectonic activity, whereas by the Late Pliocene onwards there seems to be a restricted connection between the Pacific and Indian Ocean (Karas et al., 2011; De Schepper et al., 2014;

Christensen et al., 2017; Karas et al., 2017).

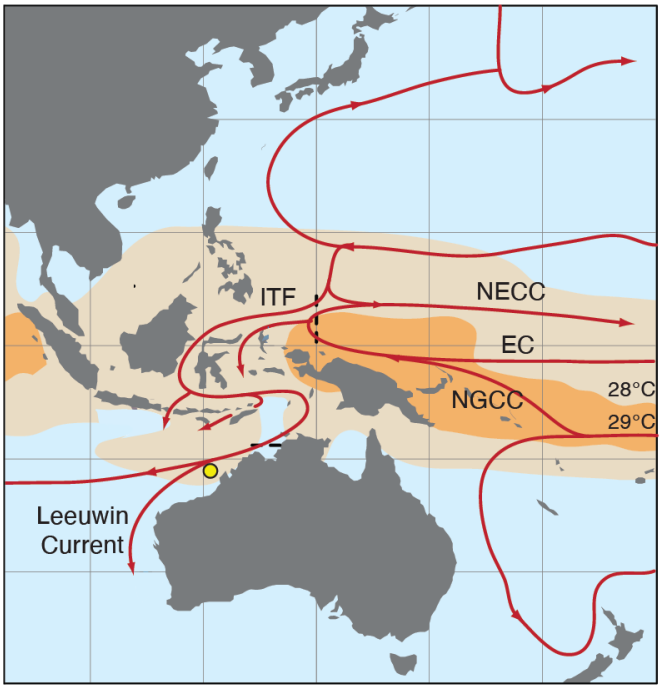


Figure 3.1: Map of Site U1482, marked by the yellow circle, and the primary currents around the north western margin of Australia and through the Indo-Pacific Warm Pool (IPWP). NECC = North Equatorial Countercurrent, NGCC = New Guinea Coastal Current, EC = Equatorial Current, ITF = Indonesian Through Flow, LC = Leeuwin Current. The northern part of the LC can be called the Hadley Current, but for the purpose of this work are considered as one system. Figure modified from Rosenthal et al. (2018).

Globally, there was significant nannoplankton turnover that accompanied the drastic climatic transition between 5 Ma and 1 Ma, with the Pliocene-Pleistocene being a well-documented period of reduced diversity in nannofossils (Bown et al., 2004). Aubry et al. (2007) argued that the transition from the warm Pliocene to the cool Pleistocene was the driver for the nannoplankton turnover and the subsequent extinction events. The long-lived Cenozoic genus *Discoaster*, within the order Discoasterales, met their demise during this period and were clearly impacted by climate fluctuations prior to this final extinction (Chapman & Chepstow-Lusty, 1997; Schueth & Bralower, 2015). They are a distinct genus of nannoliths that have been present in the fossil record since the late Paleocene ($\sim$60 Ma) and are prominent in the fossil record up until their extinction at $\sim$1.9 Ma, in the Pleistocene (Young, 1998). The final 1 million

years of their existence was punctuated by 5 successive extinctions (Bukry, 1971; Raffi et al., 2006), until the final extinction of *D. brouweri* at 1.9 Ma. Although their successive Pliocene extinctions are well documented and constrained in time (e.g. Bukry, 1971; Browning et al., 2017; Tangunan et al., 2018), the ultimate cause of this systematic extinction within one clade is till debated. One explanation is due to variations in SSTs (Chapman & Chepstow-Lusty, 1997), but their extinction occurs diachronously in different ocean basins (Raffi et al., 2006; Schueth & Bralower, 2015), indicating that changes in SSTs cannot be the only factor in their demise. Although they are thought to have an affinity for warm and oligotrophic waters (Minoletti et al., 2001; Bralower, 2002; Schueth & Bralower, 2015) their depth habitat is still uncertain. δ^{18}O records of discoasters resembled planktonic foraminifera records (*Globorotalia menardii, Dentoglobigerina altrispira, Globigerinoides obliquus*), placing their depth habitat in shallow waters (Minoletti et al., 2001), contradicting the notion that this group prefers the deep photic layer (Bralower, 2002; Schueth & Bralower, 2015). Schueth & Bralower (2015) suggest that that although *Discoaster* and *Florisphaera* both live in deep but warm waters, the *Discoaster* niche became more restricted in the late Pliocene, leaving them vulnerable to extinction. Trends in abundance through the late Neogene, and especially the decline in *Discoaster* alongside the rise in *Florisphaera* and *Gephyrocapsa* indicate ocean structure as a potential driver, with a change from shallow, mixed layer nutrient cycling to the modern conditions with a deep nutricline and stronger seasonality (Boscolo-Galazzo et al., 2021; Boscolo-Galazzo et al., 2022).

We present a high-resolution ($\sim$4 ka) size separated coccolith fraction record of δ^{13}C isotopes, δ^{18}O isotopes and Sr/Ca ratios to determine changes in the tropical ocean from Exp. 363, Site U1482 on the north-west Australian margin (Fig. 3.1). We will concentrate on carbon limitation at an orbital scale for our δ^{13}C records, which are driven by the dynamics of declining CO_2 and orbital controlled changes in ocean structure. These records show, for the first time, the variability of the vital effects through orbital scale records. We will also concentrate on long-term changes in coccolithophore

growth rate – in both the large and small size fractions – using Sr/Ca ratios. Finally, we will determine if there are signals of either carbon limitation or changes in the growth rate associated with the *Discoaster* extinction events.

3.2 Methodology

The novel method described in Chapter 2 for splitting samples was employed in this study for the analysis of stable isotopes, trace metals and particle size distribution. In brief, samples were washed through a 63 μm then a 20 μm Endecotts Laboratory Test Sieve using deionized (DI) water, with the < 20 μm material being collected. Sediment at this point was in suspension in water. These were then centrifuged in a Mistral 1000 Centrifuge for 6 minutes at 4000 rpm, with the excess water being poured off. When fully centrifuged, samples were left to dry in an oven at 50℃ overnight until fully dry. Once dry, the samples were separated into 4 targeted size fractions: VF, F, M, and VC. The VF (very fine) and VC (very coarse) are the only size fractions that were analysed. Unsplit samples were used for nannofossil assemblage analysis.

3.2.1 *Sample selection*

The sediment samples analysed in this study were taken from IODP Expedition 363, Site U1482, on the north-west margin of Australia, at 15°3.32'S, 120°26.10'E in 1466m water depth (Rosenthal et al., 2018) (Fig. 3.1). There are 419 samples from holes A, B and C, spanning an age range from 3.02 to 1.38 million years. The average temporal resolution of this sample set is ∼4 kyrs, with the shortest time interval between samples of 0.8 kyrs and the largest 22 kyrs. Ages are assigned following the age model of Chen et al. (2022) which was based on a correlation of high-resolution benthic foraminiferal $\delta^{18}O$ data from U1482 to a globally stacked benthic $\delta^{18}O$ record (the Prob-stack; an updated LR04 record of Lisiecki & Raymo (2005); Ahn et al. (2017)) (Fig. 3.2). Samples were taken from the shipboard primary splice (Rosenthal et al. 2018), but then located on the revised splice of Lübbers et al. (2020), as adopted by Chen et al. (2022), from

depths between 99.93 and 154.33 m r-CCSF-A. The characteristics of the sediment was a clay-rich nannofossil ooze (Rosenthal et al., 2018). The preservation of nannofossils at Site U1482 is generally very good to excellent, coccospheres are often found and dissolution-susceptible taxa are present throughout (Rosenthal et al., 2018).

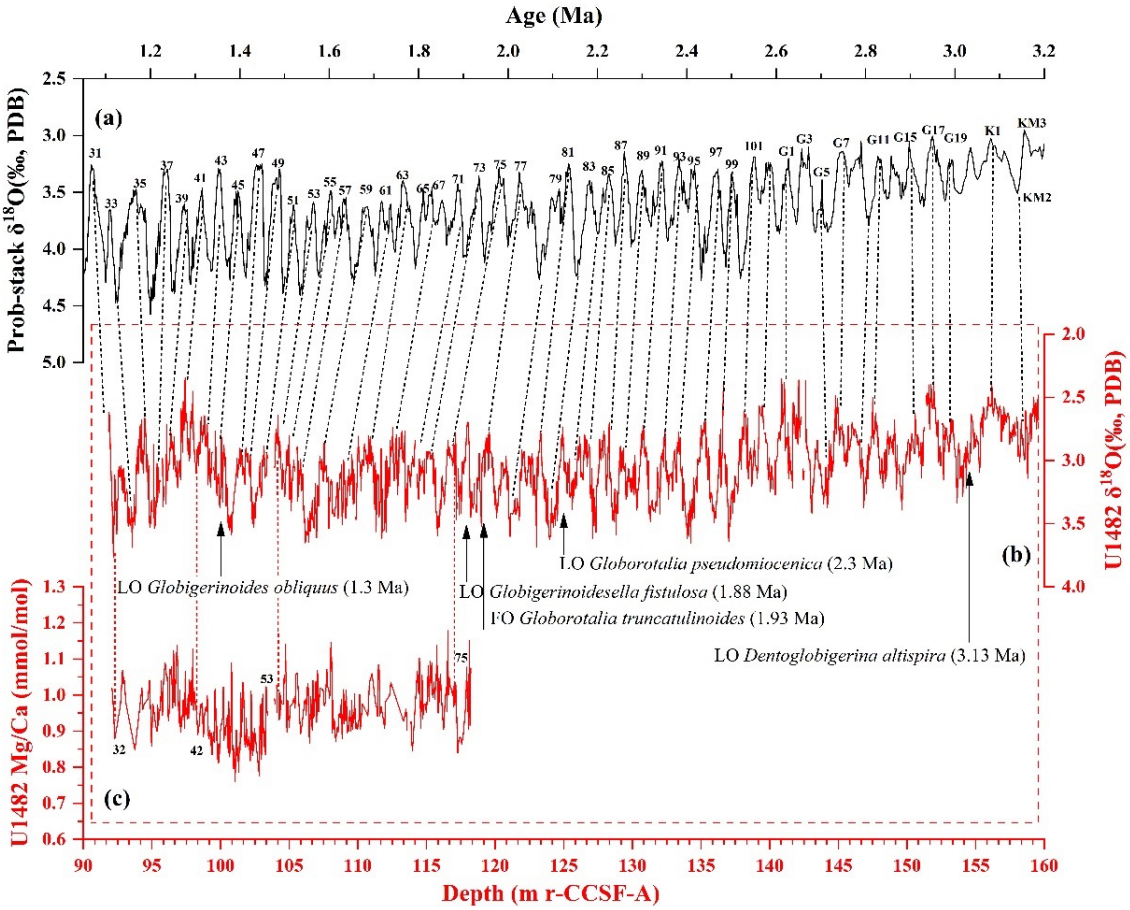


Figure 3.2: Site U1482 age model based on correlating benthic foraminiferal δ^{18}O to a globally stacked benthic δ^{18}O (the Prob-stack), modified from Chen et al. (2022 (Supplementary Materials)). (a) the Prob-stack vs. age (Ma) (Ahn et al. (2017)); (b) Benthic δ^{18}O against sampling depth (m r-CCSF-A) with biostratigraphic constraints (Rosenthal et al., 2017).

3.2.2 *Stable isotope analysis*

Stable isotope analysis was conducted on the split samples, where the VF and VC fractions were analysed and 838 samples in total (419 VF, 419 VC) were analysed at the BGS Stable Isotope Facility, Keyworth, Nottingham, on a VG Optima mass spec-

trometer (standard reproducibility of < ± 0.1%). All data are reported to the Vienna Pee Dee Belemnite (VPDB) standards. The sample went through a plasma ashing process at BGS, a widely used process to remove organic matter from samples, before being analysed. Sample material was powdered to yield CO_2 from the equivalent of 10 mg of 100% calcite and reacted with anhydrous phosphoric acid in vacuo overnight at a constant 25℃. Liberated CO_2 was separated from water vapour under vacuum and collected for analysis.

3.2.2.1 Carbon isotopes

Carbon naturally occurs in three isotopic forms, of which two are stable (^{12}C and ^{13}C) and one which is radioactive (^{14}C). They occur in different concentrations in the natural environment: ^{12}C at 98.9%, ^{13}C at 1.1% and ^{14}C which occurs in trace amounts. The presence of the latter is used in organic materials to radiocarbon date samples, and has been widely used in geological, archaeological, and palaeontological studies for this. The $^{13}C/^{12}C$ ratio of a sample whether it is, for example, bulk sediment or foraminifera, is measured and compared to the $^{13}C/^{12}C$ ratio of a known standard, in this case a laboratory standard calcite. Carbon isotopes ($\delta^{13}C$) are reported as a per mille (‰) difference to the VPDB standard (equation below).

$$\delta^{13}C = \frac{^{13}C/^{12}C_{sample} - ^{13}C/^{12}C_{standard}}{^{13}C/^{12}C_{standard}} X1000$$

3.2.2.2 Oxygen isotopes

Oxygen naturally occurs in three stable isotopic forms: ^{16}O, ^{17}O and ^{18}O. They occur in different concentrations in the natural environment: ^{16}O at 99.763%, ^{17}O at 0.0375% and ^{18}O at 0.1995%. The $^{18}O/^{16}O$ ratio of a sample is measured and compared to the $^{18}O/^{16}O$ of a known standard, in this case a laboratory standard calcite. Oxygen isotopes ($\delta^{18}O$) are reported as per mille (‰) relative to the standard (equation below). If the δ is positive, then it indicates enrichment of the heavier isotope relative to the

standard. Contrarywise, if the δ value is negative, then there is a depletion of the heavier isotope.

$$\delta^{18}O = \frac{^{18}O/^{16}O_{sample} - ^{18}O/^{16}O_{standard}}{^{18}O/^{16}O_{standard}} X1000$$

3.2.3 *Trace metal analysis*

All trace metal analysis was performed at the University of Cardiff, Wales, on an Element XR High-Resolution Inductively Coupled Plasma Mass Spectrometer (HR-ICP-MS). A total of 195 (97 VF and 98 VC) samples with a resolution of 10-20 kyr were analysed for Sr/Ca, Mg/Ca, Mn/Ca and Al/Ca ratios. The method used is detailed below.

3.2.3.1 Oxidative cleaning

Oxidative cleaning was performed at the University of Birmingham. 100 mg of the VF and VC portion of the split samples was measured into centrifuge tubes, with 10 ml of a diluted solution of sodium hyperchlorite (NaOCl) (one part DI water, one-part NaOCl) being added, and the sample was shaken. The samples were then left overnight to react, followed by centrifugation for 4 minutes at 4000 rpm. The NaOCl was then gently poured off and 10 ml of DI water was added, the sample agitated, the tube shaken and centrifuged again for 4 minutes at 4000 rpm. These steps were repeated twice more. After the final removal of the water, the samples were then dried in a 30℃ oven overnight.

3.2.3.2 Reductive cleaning

Reductive cleaning and any further steps in conducting trace metal analysis were performed at the University of Cardiff. Prior to any reductive cleaning, all tubes and bottles were cleaned using a 10% hydrochloric acid solution mixed with milliQ water. All centrifuge and Eppendorf tubes were placed in heated HCl solution on a hotplate at 100℃ for 1 hour, 150℃ for another hour and finally 200℃ for 4 hours. After this, the hot-

plate was turned off and left to cool overnight. The next day, the acid was decanted, and tubes were rinsed with milliQ water several times and left to dry. The larger bottles were filled with HCl solution and left overnight, before being decanted and rinsed thoroughly with milliQ water. To begin the reductive cleaning process, 20 mg of oxidatively cleaned sediment was weighed into a cleaned centrifuge tube, followed by the addition of 10 mL of "MNX" solution. The MNX solution was made from 300 mL milliQ water, 200 mL ammonia solution (NH_4OH) and 25 g of hydroxylamine hydrochloride. Reaction with MNX solution removes Fe-Mn oxides within the sediment, which can be a source of non-carbonate hosted trace metals in the samples. The tubes were then agitated and left on a shaker table overnight, before being centrifuged for 8 minutes at 3000 rpm.

3.2.3.3 Ion exchange

A 2% ammonia solution was made with 40 mL of concentrated (35%) ammonia and 660 mL of milliQ water. The supernatant within the centrifuge tubes was then pipetted out, with care taken not to disturb the sediment. 15 mL of the 2% ammonia solution was added, followed by agitating and shaking well for 5 minutes and then centrifuging for 8 minutes at 3000 rpm. The extraction of the supernatant, the addition of the ammonia solution and the shaking then centrifuging was repeated one more time. After this second centrifuge, the supernatant was removed, and each tube filled with milliQ water. It was then centrifuged, extracted, and rinsed with milliQ water twice more. After the last centrifuging, all but 1 mL of milliQ water was extracted, leaving the sediment in 1 mL of water.

3.2.3.4 Acetic acid dissolution

Buffered acetic acid was made using 490 mL milliQ water, 3.45 g of ammonium acetate and 2.83 mL of concentrated acetic acid. In a cleaned flow bench, a pipette set to 0.15 mL was used to agitate the sediment by aspirating and discharging repetitively the

sediment in the tubes, so that it was in a homogenous suspension. Once mixed, 0.15 mL of the suspended sediment was released into another clean 15 mL centrifuge tube and the pipette was discarded. A 5 mL pipette tip was cleaned four times with 10% HCl and four times with milliQ water, and 10 mL total of the buffered acetic acid solution was pipetted into each of the tubes containing 0.15 mL of sample. This process was repeated for every sample. These were then left overnight ($\sim$12 hours) to react. The samples were then vortexed and centrifuged for 8 minutes at 3000 rpm. From these, 0.5 mL from the top of the sample tube was aspirated and released into a labelled 0.5 mL centrifuge tube, and these were left to dry down in a 40 ℃ oven.

3.2.3.5 Nitric acid dissolution

A 0.5 M 99.99% LC/MS grade nitric acid was made up using 484 mL of milliQ water and 15.8 mL of concentrated nitric acid. Once the samples were dry, 0.12 mL of the nitric acid was pipetted into the sample tubes, vortexed and left in the fridge overnight to dissolve.

3.2.3.6 Splitting of samples for analysis

Once the samples were dissolved, they were vortexed and centrifuged. 100 μL of the sample solution was pipetted into a trace element aliquot (TE) and 200 μL was pipetted into a Ca aliquot (Ca). These were then stored in the fridge until analysis. On the day of analysis, the relevant aliquots were removed from the fridge and allowed to warm to room temperature. They were then vortexed and centrifuged. The sample names were written into the sequence window and placed in the Element autosampler. They were then run on the Element XR High-Resolution Inductively Coupled Plasma Mass Spectrometer (HR-ICP-MS).

3.2.4 *Spectral analysis*

Spectral analysis was conducted using Acycle software (Li et al., 2019), a free and comprehensive software package for time series analysis in palaeoclimate research. To remove the potential for the misinterpretation of long-term shifts as a low frequency cycle, all datasets where detrended prior to analysis using a LOESS model (locally weighted smoothing). This was then followed by a sort/unique/delete function, which removed any data points that were duplicates on the X axis. The dataset was then interpolated with a user-defined sampling rate. The resulting time series was then the basis for spectral and evolutionary spectral analyses using the multi-taper method (Thomson, 1982).

3.2.5 *Nannofossil assemblage analysis*

Nannofossil assemblage analysis was conducted on 35 smear slides made from the bulk sediment (unsplit samples), following the methodology of Bown & Young (1998). A cascading count was performed on each sample providing assemblage data with a temporal resolution of $\sim$50kyr. Coccoliths were identified using the Nannotax website (`https://www.mikrotax.org/Nannotax3/`). All taxa apart from those in the *Reticulofenestra* genera were identified to species level. *Reticulofenestra* was identified according to size categories; < 3 μm, 3-5 μm, 5-8 μm. For the purpose of calculating relative abundance (%) (Fig. 3.8), taxa were grouped to genera level, with *Reticulofenestra* having multiple size categories; < 3 μm and > 3 μm. For the comparison of the assemblage contribution (%) and the mass contribution (%) (Fig. 3.9), coccoliths were grouped to genera level, with *Pseudoemiliania, Gephyrocapsa* and *Reticulofenestra* all placed into a reticulofenestra group (Isochrysidales), with the size categories < 3 μm, 3-5 μm, 5-8 μm and > 8 μm. All other genera were sub-split into the following size divisions; < 5 μm, 5–8 μm and > 8 μm, apart from *Rhabdosphaera* and *Florisphaera* which were not size categorised due to their limited size range. To calculate the carbonate mass contributions by taxonomic group within the VF and VC size fractions, the taxon

and size specific mass estimates were taken from Baumann (2004).

The abundance of *Florisphaera profunda* has been successfully used as a palaeo-proxy of the depth of the nutricline/thermocline (Molfino & McIntyre, 1990; McIntyre & Molfino, 1996; Beaufort et al., 1997), where a high abundance of *F. profunda* indicates a deep nutricline, and vice versa. In this study, we also calculated an estimate of net primary productivity (Npp), from the percent abundance of *F. profunda* expressed as mg C m^{-2} day^{-1}, using the formulation of Saavedra-Pellitero et al. (2022):

$$Npp = 10^{3.09-0.01*\%F.profunda}$$

which is based on the calibration to satellite-derived Npp across multiple oceanic regions of Hernández-Almeida et al. (2019), but with additional calibration points from the Pacific Ocean.

3.2.6 *Particle size analysis*

Particle size analysis was conducted on the VF and VC size splits of 35 samples using slides prepared following the technique of Flores & Sierro (1997). Slides were imaged using a Zeiss AxioScope A.1 at 1000x magnification with circular polarisation, and a Märzhäuser Wetzlar motorised XYZ stage with 20-30 fields of view (FOV) taken. Images were then processed using Fiji (Schindelin et al., 2012), a version of ImageJ that facilitates particle size distribution. Any particle with an area < 1 μm^2 or > 80 μm^2 were excluded as unlikely to be coccolith material. A further, in depth description of this method can be found in Chapter 2.

3.3 Results

3.3.1 *Stable isotope analysis -* $\delta^{13}C$

Stable isotope data reveals that a significant offset between the $\delta^{13}C$ of the different size fractions is maintained throughout the period of just over $\sim$1 ‰ (Fig. 3.3A). This

offset is maintained across precession-scale orbital scale variations. The $\delta^{13}C_{VC}$ signal is noisier and overall has a greater range in values than $\delta^{13}C_{VF}$, but for most of the record $\delta^{13}C_{VF}$ and $\delta^{13}C_{VC}$ are synchronised with each other.

The difference between $\delta^{13}C_{VF}$ and $\delta^{13}C_{VC}$ was calculated for all samples as:

$$\Delta\delta^{13}C = \delta^{13}C_{VF} - \delta^{13}C_{VC}$$

LOESS smoothing (locally weighted smoothing) was applied to $\Delta\delta^{13}C$ to make trends in this relationship clear (Fig. 3.3B). On the LOESS regression curve, there are deviations from the maintained $\sim$1 ‰. There are several periods of increased difference between $\delta^{13}C_{VF}$ and $\delta^{13}C_{VC}$ throughout the study interval. First, at the beginning of the record at $\sim$3 Ma where the difference is $\sim$1.5 ‰, and again slightly earlier, at $\sim$2.8 Ma where the difference is $\sim$1.6 ‰. It remains relatively stable until $\sim$2.3 Ma, where the difference decreases to a low at $\sim$2.1 Ma of $\sim$0.75 ‰. This is followed by a sharp increase to a high at $\sim$1.95 Ma where the difference is $\sim$1.5 ‰. A gradual decrease to a low difference is seen at $\sim$1.55 Ma, where it reaches 0.75 ‰, before remaining just over 1 ‰ until the end of the record.

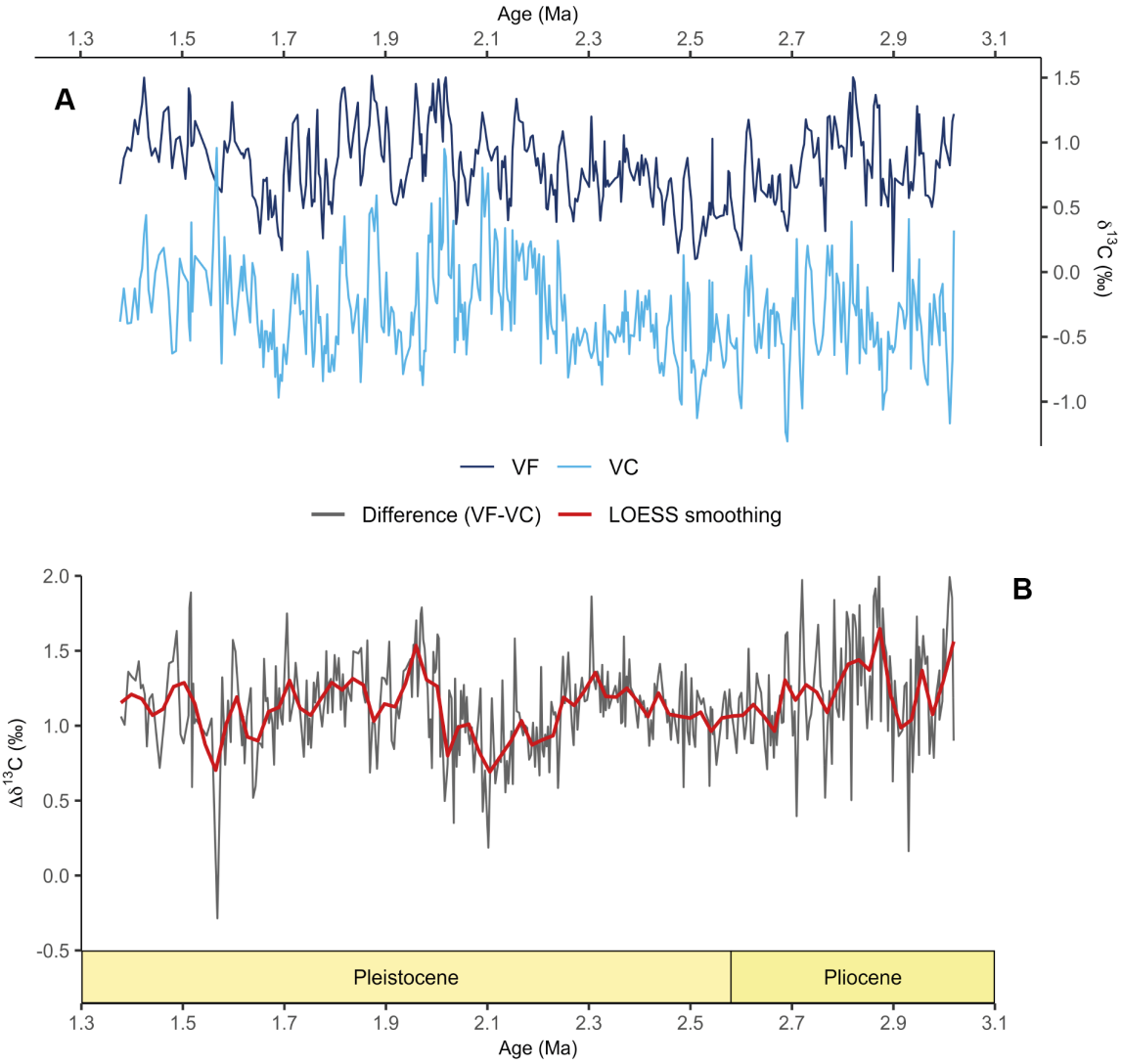


Figure 3.3: Carbon isotope analysis ($\delta^{13}C$) and the difference of the very fine (VF) coccolith fraction and very coarse (VC) coccolith fraction. A) Carbon isotopic signal of the VF (light blue) and VC (dark blue) coccolith fractions from the Pliocene to the Pleistocene (3.02 to 1.38 million years ago). B) Difference between the VF and the VC fraction (VF-VC) carbon isotope measurement from the same time span. Note the red line is LOESS smoothing with a span of 0.05.

3.3.2 *Stable isotope analysis - $\delta^{18}O$*

Stable isotope analysis shows that there is an offset between the $\delta^{18}O_{VF}$ and $\delta^{18}O_{VC}$ throughout the period, but it is variable and less consistent than that of the carbon isotope fractions (Fig. 3.4A). On orbital scales there are intervals where $\delta^{18}O_{VF}$ and

$\delta^{18}O_{VC}$ are both more and less in phase with each other.

The difference between $\delta^{13}C_{VF}$ and $\delta^{13}C_{VC}$ was calculated for all samples as:

$$\Delta\delta^{18}O = \delta^{18}O_{VF} - \delta^{18}O_{VC}$$

LOESS smoothing was applied to the $\delta^{18}O$ difference between size fractions to create a smoothed line through the time series to allow trends to be seen (Fig. 3.4B). The largest $\Delta\delta^{18}O$ occurs around the Pliocene-Pleistocene boundary, with a difference of $\sim$1.5 ‰, and a second peak at $\sim$1.95 Ma with a difference of $\sim$1.4 ‰. The smallest values of $\Delta\delta^{18}O$ occurs $\sim$1.6 million years ago, where the difference reach just below 0 ‰, measuring $\sim$-0.3 ‰, indicating that the VC fraction is recording more positive values than the VF fraction. Other low values of $\Delta\delta^{18}O$ occur at $\sim$2.15 Ma ($\sim$0.3 ‰ difference), $\sim$2.75 Ma and $\sim$2.95 Ma (both exhibiting differences of 0.4 ‰).

3.3.3 *Spectral analysis*

Both the $\delta^{13}C_{VF}$ and $\delta^{13}C_{VC}$ respond to the 41kyr cycle (obliquity), as demonstrated by power spectral analysis (Fig. 3.5A and B). Evolutionary spectral analysis of the $\delta^{13}C_{VF}$ (Fig. 3.5C) shows steady 41kyr orbital forcing between 3 and 2.4 Ma before a slight branching and influence of 2 cycles, 41kyr and 30kyr, between 2.2 and 1.8 Ma. This is then followed with 41kyr being the dominant cycle influence from 1.8 to 1.4 kyr. Evolutionary spectral analysis of the $\delta^{13}C_{VC}$ (Fig. 3.5D) shows a similar pattern, with the 41kyr obliquity cycle dominant from 3 to 2.2 Ma. Between 2.2 and 1.8 Ma there seems to be branching, with an influence from both the 41kyr and $\sim$30kyr dominance, and then, between 2 and 1.7 Ma, it is back to predominantly being influence by the 41kyr cycle. The main difference is from 1.7 to 1.4 Ma, where power at $\sim$34kyr is dominant but within a broader range of frequencies.

Lead-lag analysis was completed on the $\delta^{13}C_{VF}$ and $\delta^{13}C_{VC}$ (Fig. 3.6), to determine if there is a consistent temporal offset between these two parameters. The

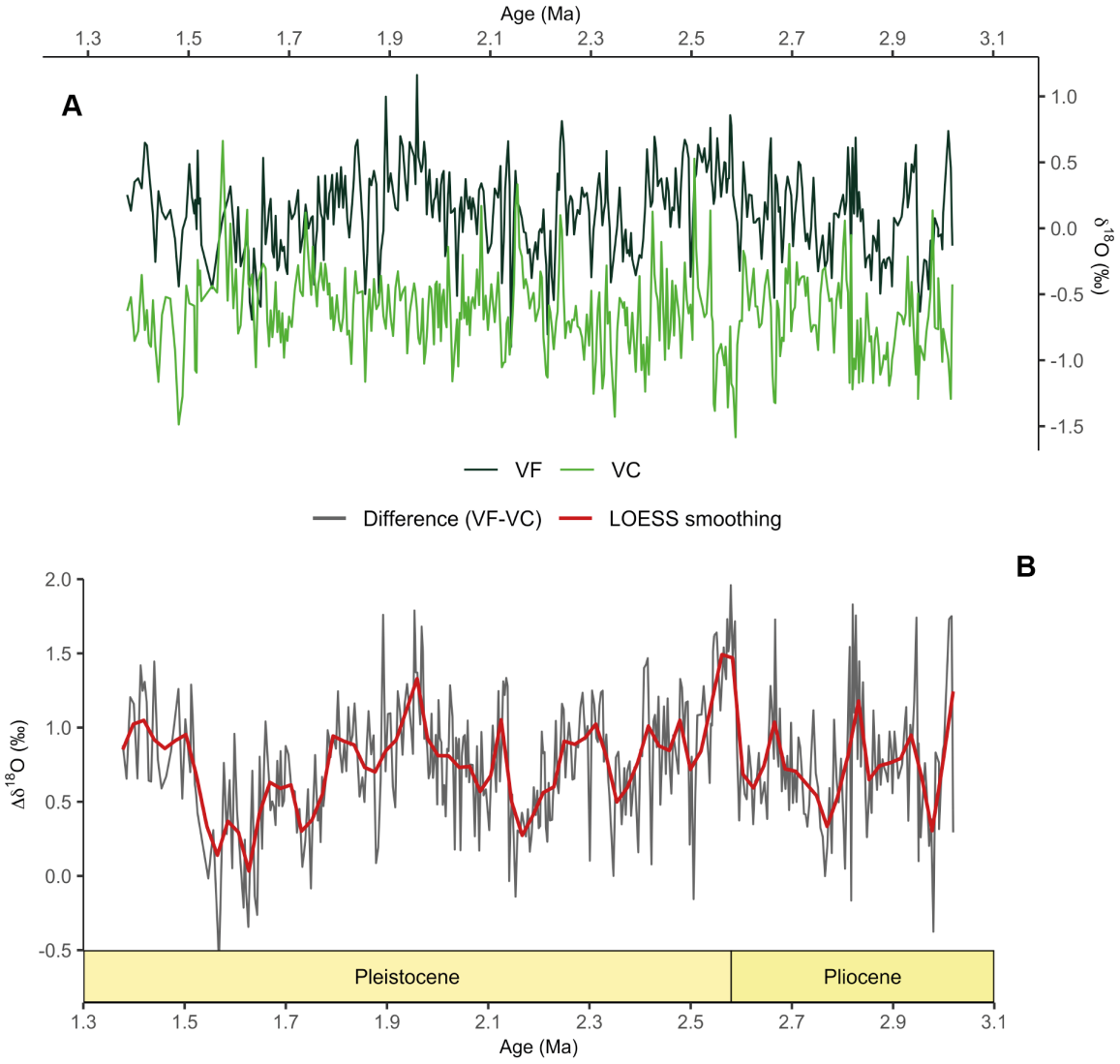


Figure 3.4: Oxygen isotope analysis ($\delta^{18}O$) and the difference of the very fine (VF) coccolith fraction and very coarse (VC) coccolith fraction. A) Oxygen isotopic signal of the VF (dark green) and the VC (light green) fractions from the Pliocene to the Pleistocene (3.1 to 1.3 million years ago). B) Difference between the VF and VC fractions (VF-VC) oxygen isotope measurement from the same time span. Note the red line is LOESS smoothing with a span of 0.05.

expectation is for zero offset, if both are responding directly to surface ocean chemistry mediated by the differential isotopic fractions between different sized coccolithophores. For the analysis, $\delta^{13}C_{VF}$ is used as a reference series onto which the target series, $\delta^{13}C_{VC}$, is matched. The lead-lag relationship between the two series seems to be minimal, with the target leading the reference by -0.45. The closer to 0, the closer the

match is between the two time series.

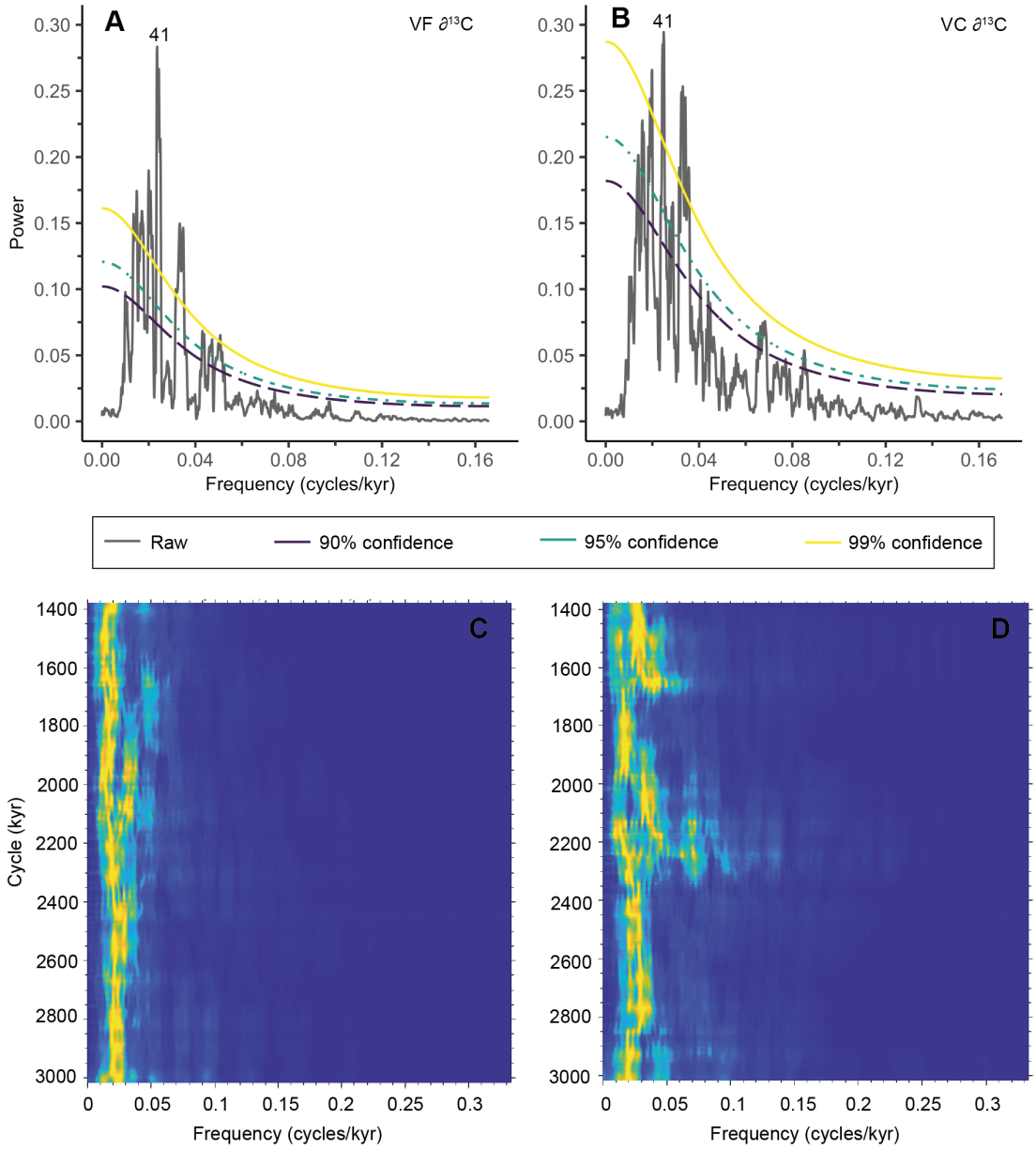


Figure 3.5: Spectral power versus frequency plots for $\delta^{13}C$ and wavelet analysis. A) VF B) VC. Coloured lines indicate 90%, 95% and 99% confidence intervals. Note the number 41, indicative of the 41kyr orbital cycles. C) wavelet analysis for VF. D) wavelet analysis for VC. Note that the timescale is in kyr.

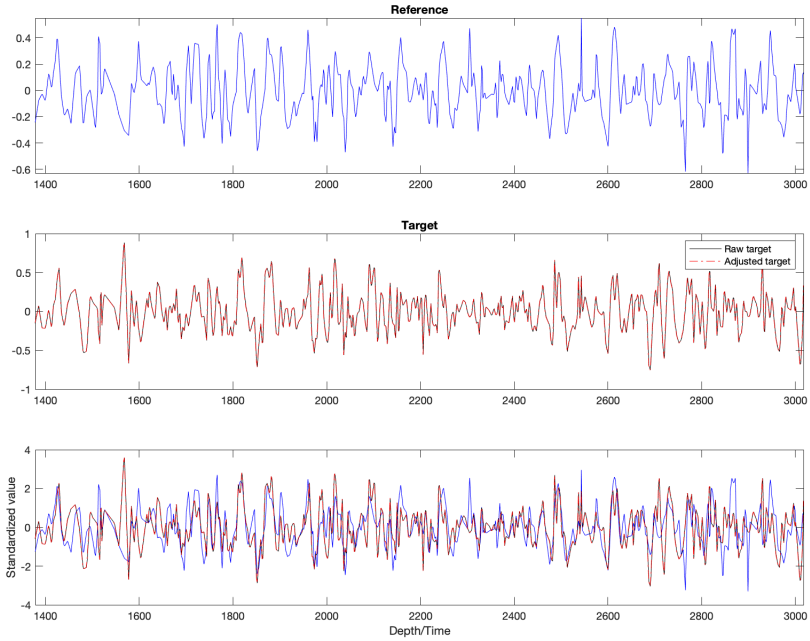


Figure 3.6: Lead-lag relationship between $\delta^{13}C_{VF}$ and $\delta^{13}C_{VC}$. From top to bottom: the reference series, $\delta^{13}C_{VF}$. Middle panel: the target series: $\delta^{13}C_{VC}$. Bottom panel: the two time series with the aim of matching the reference and target together. There is a lead-lag relationship of -0.45, where the target is leading the reference. Note the timescale is in kyr.

3.3.4 *Trace metal analysis*

Sr/Ca trace metal analysis between the VF and VC fraction shows there is a distinct difference between the two size fractions, although not represented as a consistent off-set in absolute values (Fig. 3.7A). The VF fraction is relatively stable, with measurements ranging from 2.12 mmol/mol to 2.49 mmol/mol. The VC fraction however fluctuates over a larger range, sometimes between adjacent samples, from 1.81 to 2.74 mmol/mol. Before $\sim$1.9 million years ago, this fluctuation in the VC fraction is more marked, with more notable excursions to low (< 2 mmol/mol) values, but afterwards it follows the VF fraction more closely in absolute values and relative changes (Fig. 3.7A). The difference between the VF and VC fractions:

$$\Delta Sr/Ca = Sr/Ca_{VF} - Sr/Ca_{VC}$$

is shown in Fig. 3.7B, with LOESS smoothing (locally weighted smoothing) to allow long-term trends to be seen. There is a general trend from small positive values of ΔSr/Ca, with the largest offset at ∼2.9 million years, to small negative values, with the largest negative offset at ∼1.4 million years ago. The difference is often close to zero or slightly positive, meaning that the VF fraction has a higher Sr/Ca ratio, but at ∼1.9 million years ago this seems to switch to VC having a higher Sr/Ca value.

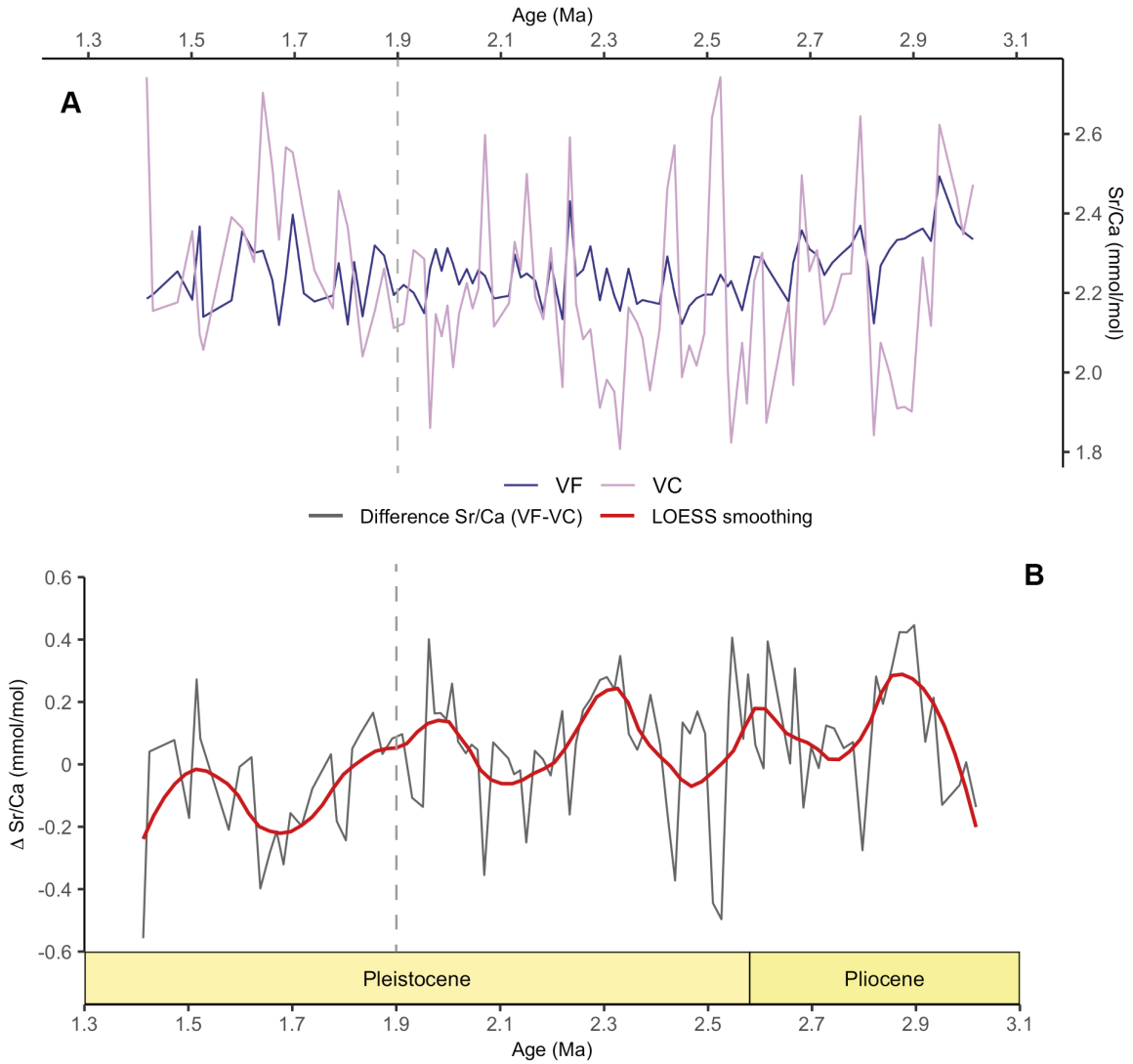


Figure 3.7: Trace metal analysis (Sr/Ca) and the difference of the very fine (VF) coccolith fraction and the very coarse (VC) coccolith fraction and the difference between the VF and VC. A) Sr/Ca ratio signal (mmol/mol) of the VF (dark purple) and the VC (light purple) fractions from the Pliocene to the Pleistocene (3.1 to 1.3 million years ago). B) Difference between the VF and VC fractions Sr/Ca measurements (ΔSr/Ca = $Sr/Ca_{VF} - Sr/Ca_{VC}$). Note the red line is LOESS smoothing with a span of 0.2. The dashed vertical grey line indicates the extinction of the discoasters at 1.9 Ma.

3.3.5 *Nannofossil assemblage analysis*

In the samples made from the bulk sediment, a total of 38 species and species groups were identified, with well-preserved taxa and most specimens identifiable to species level. The assemblage is dominated by *Florisphaera profunda* (25-84%), with alternating sub-dominant small *Gephyrocapsa* (2-40%) and *Reticulofenestra* species (4-56%). This is followed by *Calcidiscus* species and *Pseudoemiliania lacunosa* (both up to 6%), and *Discoaster* species (up to 5%). Other species that regularly made up < 5% of the taxa were *Helicosphaera* and *Umbilicosphaera*. After the removal of *Florisphaera* and small *Gephyrocapsa* species, *Reticulofenestra* species dominate the assemblage (36-85%) followed by *Calcidiscus* (1-22%), *Umbilicosphaera* (up to 16%), *P. lacunosa* (2-12%) and *Discocaster* species (up to 14%) (Fig. 3.8C).

The final *Discoaster* extinction event is captured in these samples, with the *D. brouweri* final occurrence at 1.95 million years ago (Ma) on the U1482 astronomically-tuned aged model, which is concurrent with that compiled in Backman et al. (2012) and Anthonissen & Ogg (2012). The relative abundance of the discoasters – in the non-*Florisphaera* and *Gephyrocapsa* component - starts at 19% at 2.98 Ma, but then declines to 1.4% at 2.57 Ma, followed by an increase to 25% at 2.37 Ma (Fig. 3.8B). There is then a final decrease in their abundance up to their demise at 1.95 Ma, with the final few samples (2.09-1.95 Ma), having only 1 or 2 specimens per sample. *D. brouweri* is the most common *Discoaster* seen throughout the record.

3.3.6 *Taxonomic composition of size separations*

In both size fractions, taxonomic composition is often dominated by the smaller liths, such as the *Florisphaera* and small (< 3 μm) reticulofenestra group. In the VF fraction, when combined, they make up over 90-97%, of the analysed assemblages (Fig. 3.9A). Larger liths (those > 5 μm) make up between 0 and 0.55% of the assemblages in the VF fraction (Fig. 3.8A). In the VC fraction, the *Florisphaera* and small (< 3 μm) reticulofenestra group still make up a wide range (57-91%) of the taxonomic compo-

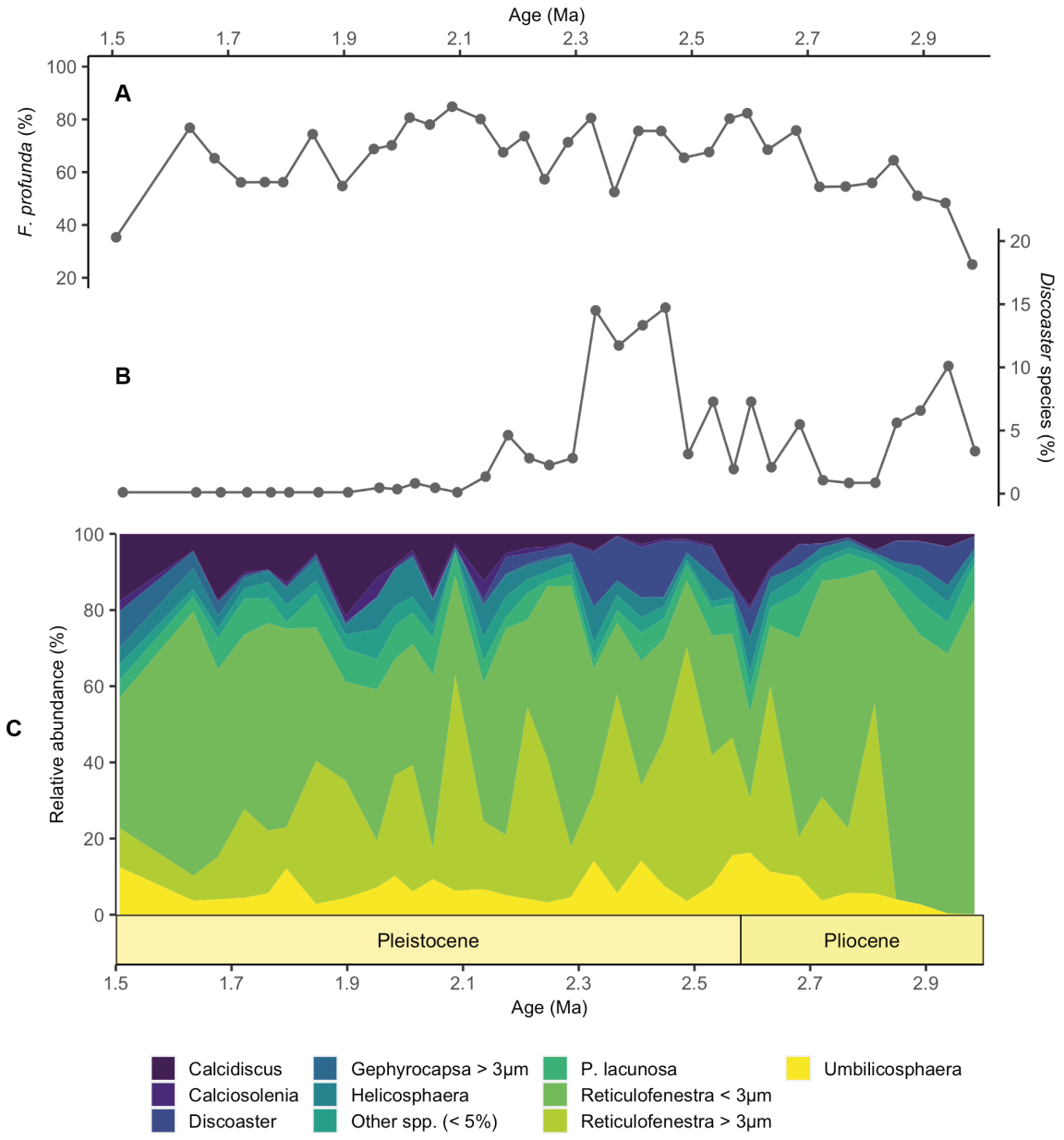


Figure 3.8: Nannofossil assemblage analysis samples spanning from the Pliocene to the Pleistocene (∼3.1 to 1.3 million years ago. A) *Florisphaera profunda* relative abundance percentage. B) *Discoaster* species relative abundance outside of the *F. profunda* and small *Gephyrocapsa* count. C) Relative abundance of all taxa without *F. profunda* and *Gephyrocapsa* < 3 µm. Note the grouping of Other spp. for those that made under 5% of the total relative abundance.

sition, with the larger liths (those > 5 µm) making up 0.55-14% of the assemblages (Fig. 3.9B). When a comparison is made between the assemblage composition and the mass composition, the VF fraction sample mass is made up of the smaller groups,

such as the *Florisphaera* and smaller reticulofenestra group (Fig. 3.9C). In the VC fraction, however, although those in the smaller reticulofenestra group often make up 20% of the mass, the larger coccoliths (*Calcidiscus, Helicopshaera, Pontosphaera, Umbilicosphaer*a) far outweigh the mass (Fig. 3.9D). This is due to their much larger and thicker liths.

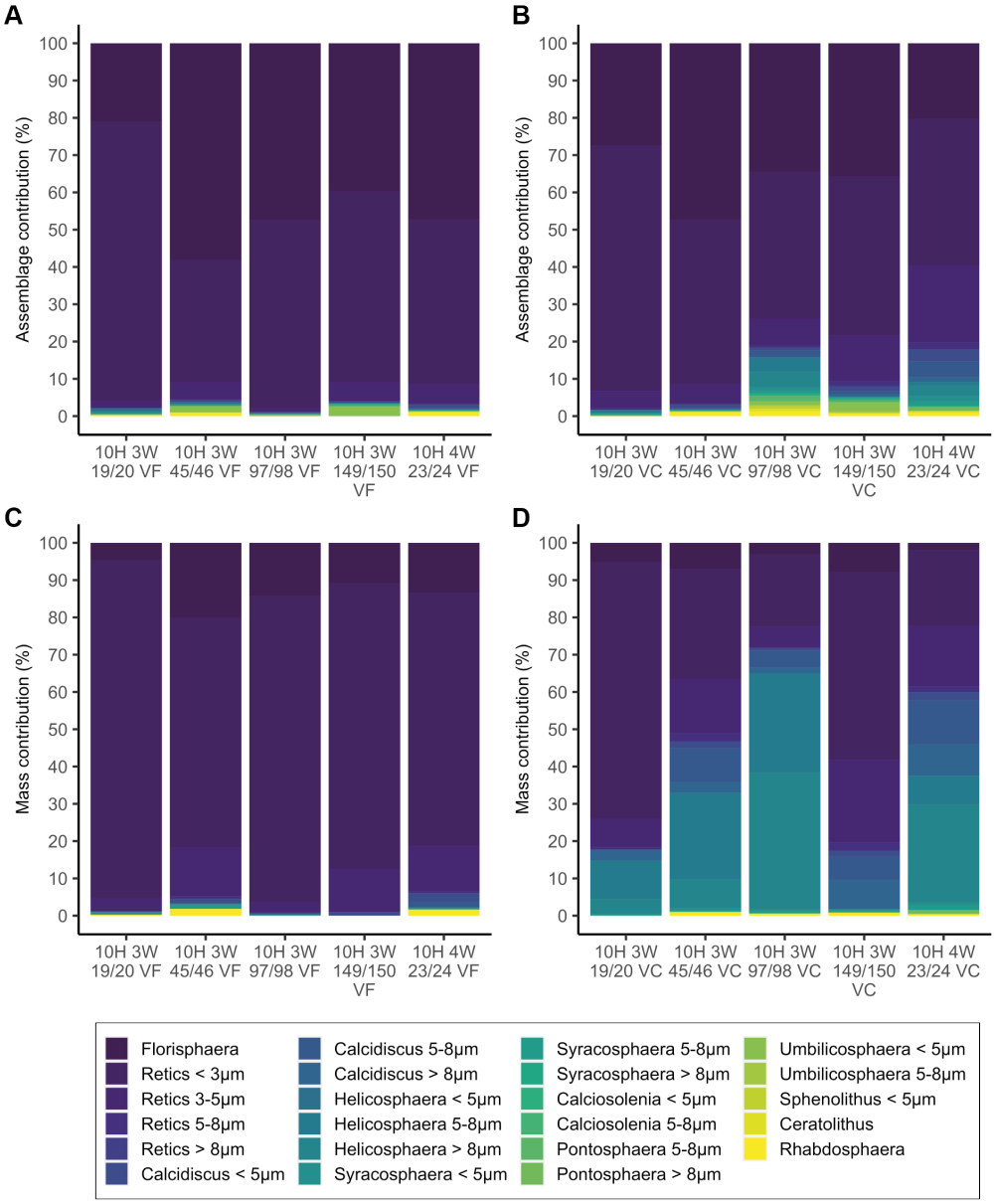


Figure 3.9: Assemblage contribution and mass contribution of 5 samples (10H 3W 19/20, 10H 3W 45/46, 10H 3W 97/98, 10H 3W 149/150, 10H 4W 23/24). Panels A & B show the assemblage contribution; A for the VF fraction and B for the VC fraction. Panels C & D show the mass contribution; C for the VF fraction and D for the VC fraction. Mass contribution was calculated using mass estimates of liths from Baumann (2004).

3.3.7 *Size corrections for $\delta^{13}C$*

The following methodology was used as an initial attempt at correcting for variability in size and mass distributions between the size fraction separates from one sample to the next. The coccolith area (size) distributions were characterised by their mean size values. The relationship between coccolith size – as represented by the means of the distributions - and coccolith size fraction isotopic values were assumed to follow a linear trend, allowing the gradient of the size-isotopic composition relationship to be calculated for each sample from the VF and VC size fraction data as:

$$Gradient = \frac{(\delta^{13}C_{VF} - \delta^{13}C_{VC})}{(\bar{X}_{VF} - \bar{X}_{VC})}$$

Where $\bar{X}_{VF}$ and $\bar{X}_{VC}$ are the mean areas of the coccolith size distributions for the very fine and very coarse fractions respectively. Using the gradient of this relationship (units of ‰/μm^2), the predicted isotopic offset ($\Delta\delta^{13}$C) was calculated for all samples, assuming that they all had the same size differential as the mean of the measured size differentials of all samples (2.68 μm^2).

From this analysis two things are clear. First, that this normalisation somewhat reduces the variance in $\Delta\delta^{13}$C between samples when the size differential between samples is relatively large (> 2 μm^2) (Fig. 3.10). In other words, where there is a larger offset in measured sizes of the VF and VC size fractions, the size correction reduces inter-sample variability, presumably that are coming in where there are large variations in the size distribution between samples. However, where there is a small differential between the mean values of size distributions of the VF and VC fractions (< 2 μm^2), the application of the correction causes a consistent bias to greater isotopic offsets as the size distributions become closer (Fig. 3.10). This effect is clearly because the raw isotopic offsets do not change substantially when this mean size differential becomes small, so as the size differential reduces the gradient of the size-isotopic composition relationship rapidly increase as the denominator of the above equation tends to zero.

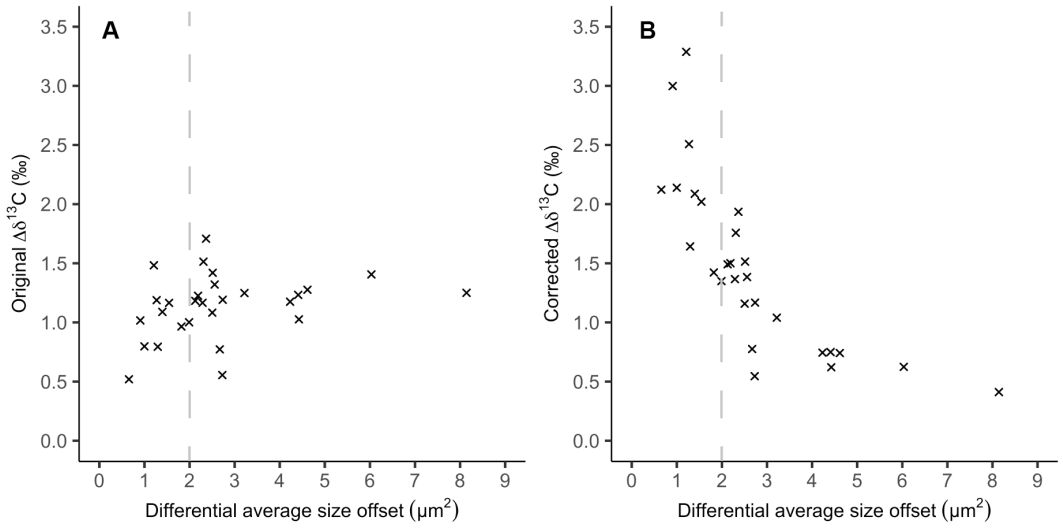


Figure 3.10: Average differential size offset between the VF and VC fractions versus $\Delta\delta^{13}$C. Grey dashed line in both A and B denotes 2 μm^2 size offset. A) The original $\Delta\delta^{13}$C between the VF and the VC fraction versus average area offset. B) the corrected $\Delta\delta^{13}$C between the VF and VC versus the average area offset. Note that those with > 2 μm^2 offset have a smaller variance, but those with < 2 μm^2 offset have a greater bias to greater isotopic offsets.

At present, the best understanding of this is that the difference in the mean coccolith area distributions provide a better representation of the difference in coccolith mass distributions when there is a greater offset between the two area distributions; i.e where there is a greater difference in size between the large and small size fractions. As noted in Chapter 2, the size distributions of all fractions are strongly left skewed towards smaller coccoliths, whereas the underlying mass distribution across size categories is strongly right skewed. Combining these two distributions to properly correct for mass distribution between the size fractions is non-trivial and is an area of active work in collaboration with Dr Sara Jabari (School of Mathematics) but which has not yet reached a resolution.

3.4 Discussion

3.4.1 *Coccolith size-fraction $\delta^{13}C$*

Our results follow on and confirm a large isotopic offset (> 1 ‰) between $\delta^{13}C_{VF}$ and $\delta^{13}C_{VC}$ in coccoliths throughout the Pliocene-Pleistocene transition, as seen previously in longer scale studies (Bolton & Stoll, 2013; Bolton et al., 2016). Our study is the first to concentrate on vital effects at such a high temporal resolution; the previous study of coccolith chemistry across this time period presented 22 data points (Bolton et al., 2012), compared to the 419 from this study. The $\delta^{13}C$ analyses show coccolith vital effects consistent with the 'heavy' and 'light' grouping of extant coccolithophore species (Dudley et al., 1986; Ziveri et al., 2003; Bolton & Stoll, 2013), where the VC fraction, with the larger coccoliths, plots consistently isotopically lighter than the VF fraction, consisting of the smaller coccoliths (Fig. 3.11A). The average particle size analysis also shows that separations with a greater contribution from larger particles also have lighter $\delta^{13}C$ values, whilst those with a smaller particle size distribution have more positive $\delta^{13}C$ values (Fig. 3.11B).

The advantage of this new, higher resolution data is that it shows relative stability in $\Delta\delta^{13}C$ when time averaged over ~20,000 years. On shorter timescales there are orbital or sub-orbital variations in $\delta^{13}C$ but with sufficient data, these can be smoothed to generate a better picture of long-term coccolith geochemistry in response to external environmental forcing. In this study, we attribute sample-to-sample variation to be most likely driven by changes in taxonomic composition of assemblages that could significantly influence the geochemical composition of individual samples, but over high-resolution data this averages out between multiple samples. These data show that the vital effects seen in coccoliths are present throughout orbital scale variations whilst both the primary $\delta^{13}C_{VF}$ and $\delta^{13}C_{VC}$ respond strongly to the 41kyr obliquity cycle – presumably representing underlying variations in the $\delta^{13}C$ composition of seawater DIC. On this orbital scale there looks to be a shift in the magnitude of variability

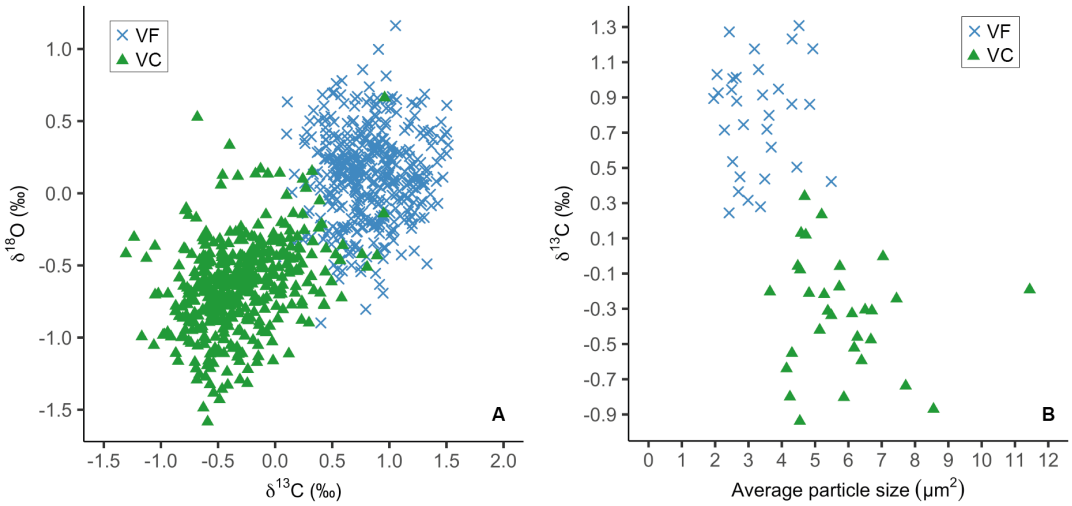


Figure 3.11: A) Cross plot of δ^{18}O vs δ^{13}C for all samples. VF is the blue crosses; VC is the green triangles. The two size fractions plot their isotopic signatures relatively separate to each other – VF is more positive in both δ^{13}C and δ^{18}O, VC is more negative in δ^{13}C and δ^{18}O. B) δ^{13}C for VF (blue crosses) and VC (green triangles) vs. average particle size (μm^2). The more positive δ^{13}C belongs to the VF fraction, the more negative δ^{13}C to the VC fraction.

of δ^{13}C in both VF and VC fractions after $\sim$2.2 Ma (Fig. 3.5C and D), most likely indicative of an increased Earth System response to orbital forcing in the early Pleistocene, including larger glacial/interglacial cycles (Lisiecki & Raymo, 2005) and/or stronger variations in the Australian monsoon (Chen et al., 2022). In particular, the change seen in the $\delta^{13}C_{VC}$ evolutionary spectral analysis to a $\sim$23 kyr precession influence at 1.7 Ma could be indicative a movement towards stronger monsoon conditions, as proposed by Chen et al. (2022).

When comparing the data presented here to the differential offset for δ^{13}C between small and large coccoliths seen in Bolton et al. (2012) (Fig. 3.12), the difference in resolution makes it difficult to compare trends. The samples from Bolton et al. (2012) were from Ocean Drilling Program (ODP) Site 999 in the Caribbean Sea and coccolith size separations were prepared following decanting protocols from Paull & Thierstein (1987) and Stoll & Ziveri (2002). This resulted in size restricted rather than monospecfic coccolith fractions. In the $\Delta\delta^{13}$C from our study (Fig. 3.3B), the trend for the overlapping period of time seems to be relatively stable, apart from a decrease

from 2.3 to 2.1 Ma, which is not captured in data from Bolton et al. (2012), that instead seems to be increasing in this interval. Similarly, a distinct drop in $\Delta\delta^{13}$C at ~2.6 Ma in the Bolton et al. (2012) record fall within a prolonged period of stable $\Delta\delta^{13}$C in our data. Indeed, apparent anomalies or short-term trends in the Bolton et al. (2012) record may be a result of aliasing orbital or sub-orbital variations in $\Delta\delta^{13}$C seen in the U1482 data, but which demonstrates a higher degree of stability in the running mean of this parameter. In both studies a degree of sample-to-sample variation is most likely driven by changes in taxonomic composition of assemblages that could significantly influence the geochemical composition of individual samples, but with high-resolution data, averages to give a better picture of long-term coccolith geochemistry in response to external environmental forcing.

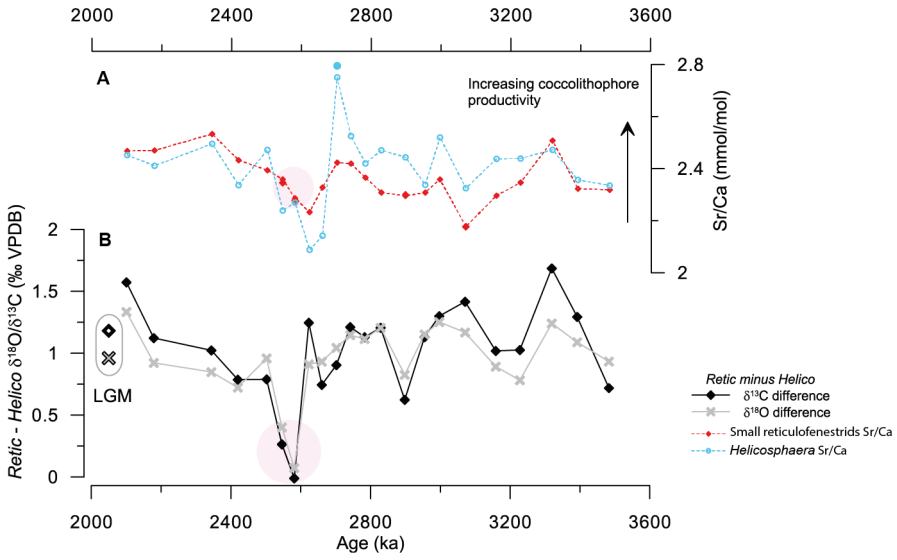


Figure 3.12: Isotopic difference and Sr/Ca ratios for small reticulofenestrids vs large *Helicosphaera*, edited from Bolton et al. (2012). A) Sr/Ca ratios for small reticulofenestrids (red dashed line) and *Helicosphaera* (blue dashed line). Higher values indicate higher coccolithophore productivity. B) Difference in isotopic composition between small reticulofenestrids and *Helicosphaera* coccolith-size fractions. δ^{13}C difference is the black line, δ^{18}O difference is the grey line.

The differential offset between $\delta^{13}C_{VF}$ and $\delta^{13}C_{VC}$ has been successfully used in geological records to indicate coccolithophore physiological responses to environmental change (Bolton & Stoll, 2013; Tremblin et al., 2016; Hermoso et al., 2020), and does not require an independent assessment of seawater $\delta^{13}C_{DIC}$. However, there are studies that seek to estimate the absolute vital effect between the isotopic signature of coccoliths and surface seawater $\delta^{13}C_{DIC}$, based on estimates from planktic foraminiferal calcite (Jin et al., 2018; Hermoso et al., 2020; Godbillot et al., 2022), to varying degrees of success. In this study we have the great advantage of a parallel high-resolution record of *Globigerinoides ruber* $\delta^{13}C$ through the same time interval from the same sediments that were analysed in this study. *Globigerinoides ruber* has relatively small vital effects (isotopic offsets from inorganic calcite) and lives in a limited spatial and depth environment (Rebotim et al., 2017), and so could be regarded as a good reference for $\delta^{13}C_{DIC}$. When plotted together, the $\delta^{13}C$ of *G. ruber* ($\delta^{13}C_{G.\ ruber}$) from Site U1482 sits very close to, but consistently slightly more positive ($\sim$0.1 to 0.2 ‰) than the $\delta^{13}C_{VF}$ (Fig. 3.13). These data strongly support the differential carbon limitation between large and small coccolithophores, with large cells reallocating a greater fraction of intra-cellular HCO_3^- from calcification to photosynthesis, leading to more negative coccolith $\delta^{13}C$ values (Bolton & Stoll, 2013; Bolton et al., 2016). The comparison to $\delta^{13}C_{G.\ ruber}$ shows that this effect is also present in smaller cells (VF fraction) during the late Pliocene – early Pleistocene, but that the reallocate fraction is smaller, leading to more positive $\delta^{13}C$ values that are closer to equilibrium ($\sim$ foraminiferal) calcite.

Overall, this is an excellent reference point record to establish $\Delta\delta^{13}C$ in a stable tropical environment. Further work should concentrate on other environments to investigate whether this stable signal is a factor of the particular oceanography of this location or is present between coarse and fine fractions in other more dynamic and/or higher productivity settings. Understanding these offsets in $\delta^{13}C$, and the cellular carbon limitation they represent, are critical in understanding the impact of de-

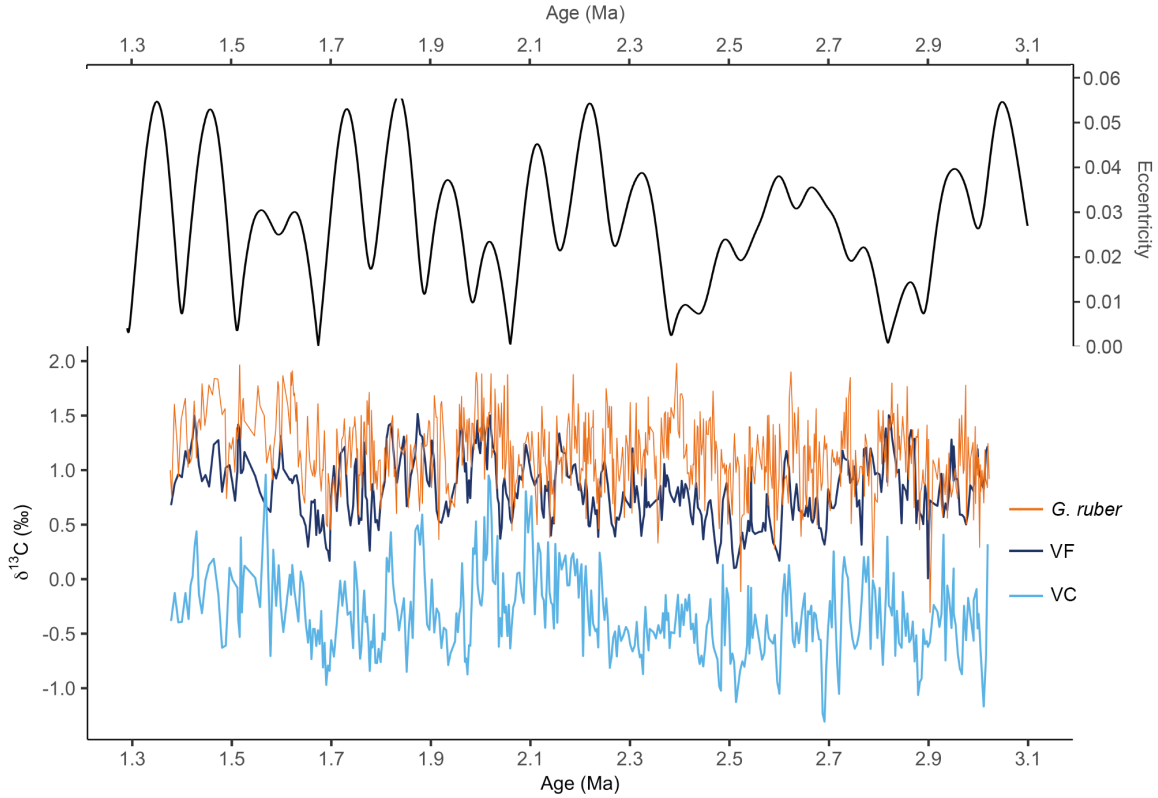


Figure 3.13: Eccentricity plotted with carbon isotope analysis of the very fine (VF) coccolith fraction in dark blue, the very coarse (VC) coccolith fraction in light blue, and $\delta^{13}C$ for the planktic foraminifera *Globigerinoides ruber* (*G. ruber*) in orange (pers. comm. Jun Liu). The $\delta^{13}C_{G.\ ruber}$ broadly plots at similar measurements as the VF coccolith fraction. Note the offset is present throughout the eccentricity orbital scale variations. Eccentricity data from `http://vo.imcce.fr/insola/earth/online/earth/earth.html`.

clining late Neogene atmospheric CO_2 on coccolithophore macroevolutionary trends (e.g. size reduction and the evolution of dominant Pleistocene taxa) and the use of coccolithophore-based CO_2 proxies. From this study, the conclusion is that carbon-limitation is broadly stable over the late Pliocene to early Pleistocene interval, consistent with the evolution of modern-like coccolithophore community structuring in the early-to-mid Pliocene (Boscolo-Galazzo et al., 2021; Boscolo-Galazzo et al., 2022; Chapter 4 of this thesis).

3.4.2 *Coccolith size-fraction* $\delta^{18}O$

There is an offset present between $\delta^{18}O_{VF}$ and $\delta^{18}O_{VC}$, but it is much more varied and not consistent in comparison to the $\delta^{13}C$ records. The $\delta^{18}O_{VC}$ is more stable than $\delta^{18}O_{VF}$, in contrast to the $\delta^{13}C$ record. *Gephyrocapsa* are part of the isotopically 'heavy' group that characterises the Noelaerahabdaceae (Dudley et al., 1986; Ziveri et al., 2003; Hermoso et al., 2015; McClelland et al., 2017), and *Florisphaera profunda* $\delta^{18}O$ measurements have found them to record the heaviest $\delta^{18}O$ signatures (Bolton et al., 2012). Changes in the composition of the assemblage (switches in dominance from *F. profunda* to *Gephyrocapsa* and vice versa) could be being recorded via the $\delta^{18}O_{VF}$ signal, most likely driven by productivity. Strong variations in the *F. profunda* to *Gephyrocapsa* ratio between samples in the Pliocene-Pleistocene were noted during shipboard biostratigraphy (Tom Dunkley Jones pers. comm.) and were thought to be associated with precession-scale variations in the clay:carbonate fraction driven by the Australian Monsoon strength.

Unlike the study of Bolton et al. (2012) (Fig. 3.12), in this study the overall $\Delta\delta^{18}O$ trends do not track $\Delta\delta^{13}C$, with peaks and troughs in each – $\Delta\delta^{13}C$ and $\Delta\delta^{18}O$ – that are not necessarily seen in the other (Figs. 3.3B and 3.4B). In the Bolton et al. (2012) record there is a distinct drop in $\Delta\delta^{18}O$ at $\sim$2.6 Ma, whereas in our study this point in time signifies a peak in the $\Delta\delta^{18}O$. As hypothesised, the sample to sample variations in our record are most likely driven by taxonomic composition, which was the reason reported in Bolton et al. (2012) for the trough seen at 2.6 Ma – they report an isolated change in species composition. However, the high-resolution nature of our study allows us to smooth over the influence of changing taxonomic composition on $\delta^{13}C$ and $\delta^{18}O$, which is not possible in a lower resolution study, where high-resolution variations are difficult to disentangle from long-term trends. Although the $\delta^{18}O$ from both studies are both variable in magnitude, it is difficult to compare the nature of these variations, because of the different temporal resolution of the two studies.

Towards the end of the record, at $\sim$1.7 Ma, the $\Delta\delta^{18}O$ begins to rapidly decline

before dropping to almost 0 at ∼1.6 Ma, with the $\delta^{18}O_{VC}$ signal actually recording higher values than the $\delta^{18}O_{VF}$ record, before the $\Delta\delta^{18}O$ stabilises with a difference of ∼1 ‰ (Fig. 3.4B). The $\delta^{18}O_{VC}$ does record more positive values here, but it is the $\delta^{18}O_{VF}$ record that drops more towards negative values. This is well after the final reduction in abundance and demise of the discoasters, which is thus unlikely to be driving the trends in this record. The relative abundance of *F. profunda* also records a sharp decrease in percentage at 1.5 Ma (Fig. 3.8A). Short term cooling episodes have been identified from the north-west margin of Australia, from benthic foraminiferal $\delta^{18}O$ records (Site U1482; Chen et al., 2022), TEX_{86} (Site U1460: Petrick et al., 2019; Site U1461: He et al., 2021) and $U^{K'}_{37}$ palaeothermometers (Site U1461: He et al., 2021). This has been touted as evidence for restriction of the Indonesian Through Flow (ITF) (Petrick et al., 2019; He et al., 2021), a major source of warm water for the Leeuwin Current (LC) (De Vleeschouwer et al., 2019). Chen et al. (2022) argues that it is indicative of a freshening of ITF surface waters being transmitted into intermediate depths, caused by enhanced precipitation due to favourable monsoonal and Westerm Pacific Warm Pool (WPWP) conditions. What is clear is there is a regional climatic change occurring due to changes in the ITF. The LC transports warm, nutrient-deficient waters along the west coast of Australia, sourced from the ITF (Pattiaratchi, 2006). There is an overall argument for a weak LC between 4 and 1.2 Ma with an increase in strength at 1.2 Ma (He et al., 2021), with punctuated periods of much weaker LC conditions at, for example, ∼2.5 Ma (Auer et al., 2019) and between 3.8-3.3 Ma (Christensen et al., 2017; De Vleeschouwer et al., 2018; Auer et al., 2019). The time around 1.55 Ma has also been recognised as one of these weaker periods (Petrick et al., 2019; He et al., 2021). A weakening of the LC would mean less of the warm, nutrient-deficient waters running along the coast, and an increase in upwelling off the coastal area of north-west Australia, leading to an increase in nutrients in the water column. The extant sub-euphotic zone species *F. profunda* lives in tropical to subtropical oceans, below the deep chlorophyll maximum (Hernández-Almeida et al., 2019) and relies on a 'clear', low-nutrient

water column to thrive at these depths. *Gephyrocapsa* species are likely better adapted to these higher nutrient conditions, with the ratio of *Gephyrocapsa* to *Florisphaera* often used as an indicator of surface ocean productivity. Although *Gephyrocapsa* is within the isotopically 'heavy' group, it is lighter in $\delta^{18}O$ than *F. profunda*. This time period is also within one of the well-known 'large *Gephyrocapsa*' intervals ($\sim$1.7 to 1.25 Ma; Agnini et al. 2017), with sizes reaching above 5 μm. One plausible mechanism for the reduction in $\Delta\delta^{18}O$ at this time is thus the loss of *F. profunda* from the VF fraction, shifting the $\delta^{18}O_{VF}$ lower, whilst an increased contribution of large *Gephyrocapsa* to the VC fraction shifts the $\delta^{18}O_{VC}$ higher. Effectively this would represent a convergence on a *Gephyrocapsa*-dominated signal $\delta^{18}O$ in both size fractions whilst the LC is weak.

A final important point is to reflect on the use of bulk carbonate $\delta^{18}O$ records as quantitative expressions of oceanographic or climate change – for example as a proxy for changes in temperature or seawater $\delta^{18}O$. Bulk carbonate records will always contain a mixture of coccoliths produced by a wide range of coccolithophore taxa with distinct $\delta^{18}O$ vital effects. In the data presented, large and small size fractions have differences in $\delta^{18}O$ of more than 1 ‰, and although they do show broadly coherent orbital-scale variations, they have differing secular ($\sim$0.5 Ma or longer) trends through time (Figs. 3.3B and 3.4B), all of which must be a result of differing cellular isotopic fractionation based on cell size or phylogeny.

3.4.3 *Coccolith size-fraction Sr/Ca*

The Sr/Ca ratios of coccoliths have been shown to be correlated to coccolithophore growth or calcification rate in both culture experiments and sediment traps (e.g., Stoll & Schrag, 2000; Rickaby et al., 2002; Ziveri et al., 2003), most likely because faster growing cells divide more often and calcify more rapidly, and this rate of calcification is the key control on the incorporation of Sr ion 'impurities' into biomineralized calcite (Stoll & Schrag, 2000; Rickaby et al., 2002; Stoll et al., 2002c). On this basis, coccolith Sr/Ca has been used in the geological record as a proxy for coccolithophore growth rate

and/or 'productivity' (e.g., Rickaby et al., 2007; Waite et al., 2008; Saavedra-Pellitero et al., 2017).

Over the interval of this study, the Sr/Ca records of Bolton et al. (2012) (Fig. 3.12) and this work (Fig. 3.7) are similar, with no significant offset between the two size fractions, but more variability in the larger size fraction. They are also close in absolute values, with average values of $\sim$ 2.2 mmol/mol in IODP Site U1482 coccoliths and $\sim$ 2.4 mmol/mol in ODP Site 999 coccoliths. Although the Bolton et al. (2012) study is based on size classes that are – in theory – based on distinct sets of dominant taxa, namely small reticulofenestrids and *Helicosphaera*, and the split of the size fractions in this study is broader, being just very fine ($\sim$ < 5μm) and very coarse ($\sim$ > 5μm), the two data sets are notably comparable in both isotopic and Sr/Ca values.

Overall, the Sr/Ca_{VF} is a more stable record than Sr/Ca_{VC}, with the Sr/Ca_{VF} ranging from 2.12 to 2.49 mmol/mol. This is indicative of no large productivity changes, which is coherent with a stable tropical environment and the assemblage analysis, particularly of *F. profunda*. An increased abundance of *F. profunda* has been used as an indicator of a deeper nutricline/thermocline, and as an overall indicator of decreased primary productivity (Molfino & McIntyre, 1990; Beaufort et al., 1997). From the abundance of *F. profunda*, we calculated the net primary productivity (Npp) (Fig. 3.14), which remains relatively stable over the studied period, ranging from $\sim$200-400 mg C m^{-2} day^{-1}, bar two outlier points at the beginning and end of the record. These productivity values are comparable to late Pleistocene values from similar oligo- to mesotrophic environments of the tropical Indo-Pacific (Beaufort et al., 2001). These results point to limited change in productivity regime over the time period and are indicative of a relatively low productivity, tropical, oligotrophic system.

The Sr/Ca_{VC} fraction, in comparison to the Sr/Ca_{VF}, shows an increased magnitude of variation over the whole record, ranging from 1.81 to 2.74 mmol/mol. A variation in magnitude of Sr/Ca ratios in the coccolith coarse fraction was also recognised by Waite et al. (2008) in a study of Pliocene equatorial Atlantic sediments, where results

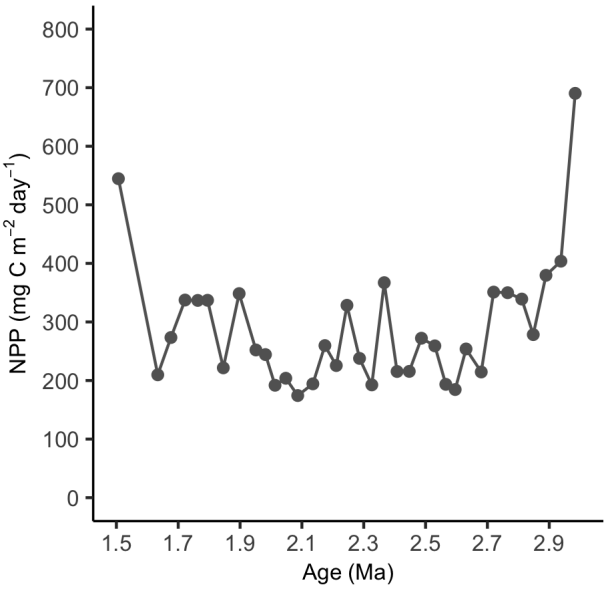


Figure 3.14: Net primary productivity from *F. profunda* relative abundance, calculated following Saavedra-Pellitero et al. (2022), expressed as mg C m^{-2} day^{-1}.

ranged between ∼1.8 and 2.5 mmol/mol. When comparing the ΔSr/Ca (Fig. 3.7B) to the relative abundance of *Discoaster* species (Fig. 3.8B), there seems to be some correlation. The points where the relative abundance is the highest, between 2.3 to 2.5 Ma and at ∼2.9 Ma seem to correspond to where ΔSr/Ca is at its highest. The convergence seen just after 2.3 Ma in Sr/Ca$_{VF}$ and Sr/Ca$_{VC}$, when ΔSr/Ca is close to zero, corresponds to the decline in *Discoaster* relative abundance, with no change at ∼1.9 Ma, around the *Discoaster* extinction. After this point, the Sr/Ca$_{VC}$ becomes much less variable in magnitude. The implication is that the discoasters are having an effect on the ΔSr/Ca, particularly in the Sr/Ca$_{VC}$. Discoasters are members of an extinct genus with no modern ancestor or analogue that we know of, and so all knowledge of their ecology or chemistry is inferred from the geological record. In general, discoasters are at the large to very large end of coccolith size, with estimates of their mass ranging from 16.5 pg for thinly calcified forms, like *D. exilis*, to as high as 219.5 pg for the thickly calcified forms, *D. surculus* (Preiss-Daimler et al., 2012). Hermoso et al. (2017) reports Sr/Ca ratios for a range of large coccoliths from the Pliocene and found that the mean Sr/Ca ratio was close to 2.5 mmol/mol, apart from for *Pontosphaera* which was 10.4

mmol/mol. This indicates that those larger forms, that would make up most of the mass of the VC fraction, would be contributing the most towards the Sr/Ca_{VC}. Changes in assemblage of the larger forms, particularly discoasters, could be driving the variation in the Sr/Ca_{VC} and corresponding ΔSr/Ca. Sr/Ca of larger coccoliths (e.g., *C. leptoporus* with 23-55% variation) have also been reported to have a more dynamic response than smaller coccoliths (e.g., *G. oceanica, F. profunda* with 6-15% variation), with this variation potentially being more pronounced in oligotrophic regions where large cell size restricts diffusive uptake of limiting nutrients (Stoll et al., 2002b).

3.5 Conclusion

This study provides the highest resolution record of size split coccolith $\delta^{13}C$ and $\delta^{18}O$ records over the Pliocene-Pleistocene transition, with accompanying Sr/Ca records. We show that there is a consistent $\sim$1 ‰ offset between the $\delta^{13}C_{VF}$ and $\delta^{13}C_{VC}$ and a variable but consistently present offset between the $\delta^{18}O_{VF}$ and $\delta^{18}O_{VC}$. The VC size fraction consistently plots with more negative $\delta^{13}C$ and $\delta^{18}O$ values than the VF fraction. Sr/Ca ratios and Npp calculations show it was a relatively stable environment, with little variation in productivity over the time period. There was a drop in *F. profunda* and a decline in the $\delta^{18}O_{VF}$ at $\sim$1.7 Ma, brought to affect by regional changes in the ITF during this time, and a potential weaking of the LC. The Sr/Ca_{VC} seems to be heavily affected by those large, heavily calcified forms, in particular discoasters. When a size correction is applied to the $\delta^{13}C$ signal, there is a reduction in inter sample variance in those with a larger size offset, but it introduces a bias towards a differential of < 2 μm^2 – it makes the differential much larger. This is part of ongoing work and is not a trivial task. Overall, this record sets in place good groundwork of a high-resolution study over a stable, oligotrophic, tropical environment, but further work is needed in more variable environments to see if the signals are still as stable.

4 | NOVEL APPROACHES TO COCCOLITH GEOCHEMISTRY OVER THE MIOCENE TO RECENT

My contribution to this work involved the preparation of the samples for analysis, the interpretation of the results, writing the text and creating the figures. The methodology is the same as that described in Chapter 2, which I co-designed with T. Dunkley Jones. Stable isotope analysis was conducted at the British Geological Survey, Keyworth, UK, by M. Leng. Particle size analysis data was collected in collaboration with S. Gattupalli. Reticulofenestra size data was collected and provided by M. Saavedra-Pellitero and T. Dunkley Jones. Gephyrocapsa species abundance data was collected by A. Jones. The age model was provided by IODP Exp. 363 participants, via shipboard biostratigraphy and paleomagnetic stratigraphy. T. Dunkley Jones provided feedback on the the research design and interpretation of the results. As in previous chapters, the editorial 'we' is used to reflect these proportional contributions.

4.1 Introduction

Coccolithophores are marine haptophyte algae and, in modern oceans, are the dominant calcifying phytoplankton (Milliman, 1993). They produce calcium carbonate plates called coccoliths, and their preservation in marine sediments makes them an excellent recorder of surface ocean environmental change through geological time. Although

many studies have focused on coccolithophore assemblage changes as indicators of phytoplankton productivity (e.g., Saavedra-Pellitero et al., 2017; Tangunan et al., 2021), surface ocean temperature (Bollmann et al., 2002) or other patterns of evolution and ecology (e.g., Jones et al., 2019; Boscolo-Galazzo et al., 2022), more recently there has been a focus on the geochemical analysis of coccolith-rich sediment fractions as the basis for palaeoenvironmental reconstructions. Most notably, the δ^{13}C stable isotopic analysis of coccolith size-separated microfractions show a marked isotopic divergence in coccolith δ^{13}C from small and large size fractions during the late Miocene to early Pliocene (7-5 Myr ago (Ma)) (Bolton & Stoll, 2013). This size-specific change in coccolith δ^{13}C has been related to a decline in atmospheric CO_2 (Bolton & Stoll, 2013; Bolton et al., 2016; McClelland et al., 2017) causing a reallocation in the coccolithophores of carbon from calcification to photosynthesis (Bolton & Stoll, 2013). These isotopic differences, also known as vital effects, are known to vary with CO_2 availability in culture studies of modern day coccolithophores (Dudley et al., 1986; Ziveri et al., 2003; Rickaby et al., 2010) as well as with cell growth rates (Ziveri et al., 2003).

Recent studies have also noted these isotopic vital effects further back in geological time related to CO_2 availability. Claxton et al. (2022) found that carbon isotope vital effects emerge and increase in magnitude during the Eocene, tracking the decline in pCO_2 records from an early Eocene high. In the Neogene, similar patterns have been observed, with limited vital effects during the middle Miocene Climatic Optimum, a period of elevated atmospheric CO_2, followed by an increase in vital effects through the Miocene Climatic Transition and associated decline in atmospheric CO_2 (Hermoso et al., 2020). As well as vital effects, there is also a strong trend of reduced coccolith size and calcification over the past 15 million years (Bolton et al., 2016; Bendif et al., 2019; Šupraha & Henderiks, 2020), again linked to declining CO_2 and alkalinity. In this case, reduced calcification in larger cells happens several million years prior to the same response of smaller cells, supporting the notion of size-specific carbon limitation driven by the fundamental differences in carbon uptake efficiency between large and

small cells (Bolton et al., 2016).

There has been less focus on $\delta^{18}O$ records of coccolith calcite, with long-term isotopic records either not including (e.g., Bolton et al., 2016; McClelland et al., 2017) or not focusing on (e.g., Rickaby et al., 2010; Bolton & Stoll, 2013) the paired $\delta^{18}O$ data that comes with standard stable isotope analyses. Culture studies on the coccolith $\delta^{18}O$ composition of modern coccolithophores have determined a split into isotopically 'heavy' (e.g. *Gephyrocapsa oceanica, Emiliania huxleyi*) and isotopically 'light' groups (e.g. *Calcidiscus leptoporus, Coccolithus pelagicus, Umbilicosphaera* spp.)(e.g., Dudley et al., 1986; Ziveri et al., 2003; Rickaby et al., 2010; Hermoso et al., 2016a; Hermoso et al., 2016b; McClelland et al., 2017). It is, however, unclear how this translated into the fossil record of coccolith isotopes, when the isotopically light group evolved relatively recently (Pliocene or younger) compared to the studies that use $\delta^{18}O$ as a focus of the work (Hermoso et al., 2020). It is also important to note that records from the geological past focus on the size-separated sediment fractions, which are by their nature multi-specific, rather than the monospecific analyses of culture studies (e.g. Bolton & Stoll, 2013; Bolton et al., 2016; Hermoso et al., 2020; Claxton et al., 2022). Here we present a $\delta^{13}C$ and $\delta^{18}O$ record of the size-separated coccolith fraction from the late Miocene to the recent, processed using the novel separation method described in detailed in Chapter 2, with the aim of testing the responses of coccolith vital effects to the most recent phase of major cooling and atmospheric CO_2 decline (Westerhold et al. 2020; Rae et al. 2021).

Within the late Miocene to Recent cooling trend, there are a series of more rapid transitions in the Earth System and/or events that have been the focus of intense study as future climate analogues. The late Miocene itself was a period of great change to both marine and terrestrial environments and ecosystems (Herbert et al., 2016), including the late Miocene cooling, where ocean temperatures dropped to near modern values between $\sim$7 and 5.4 Ma across both hemispheres (Herbert et al., 2016). Global benthic foraminiferal $\delta^{18}O$ records do not show a strong signal of sustained climate

change during this time (Herbert et al., 2016), indicating that this period of cooling was not accompanied by a large permanent increase in ice volume. The cooling detected at the tropics may not be detected in the benthic $\delta^{18}O$ because the polar regions, the location of deep water formation, had already cooled substantially and so did not affect the global $\delta^{18}O$ proxy (Herbert et al., 2016). The driver of this tropical cooling is suggested to be declining atmospheric CO_2 levels (Herbert et al., 2016), which is consistent with the late Miocene increase in coccolith vital effects (Bolton & Stoll (2013), during a time when direct carbon dioxide proxy records are still relatively sparse (Fig. 4.1).

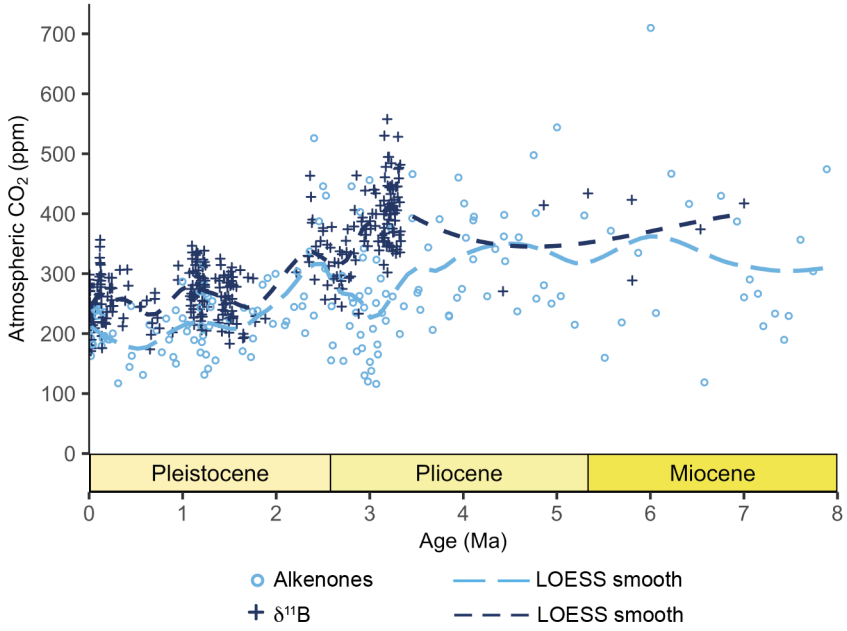


Figure 4.1: Atmospheric CO_2 reconstructions from boron isotopes (dark blue cross and dashed line) and alkenones (light blue circle and dashed line). Modified from data compilation from Rae et al. (2021).

Across a similar interval of the late Miocene, although starting up to 1 million years earlier, the late Miocene to early Pliocene "Biogenic Bloom" has been recorded as a widespread increase in silica and carbonate accumulation rates (Diester-Haass et al., 2006), and ranges from ~8 to 4.5 Ma (Lyle et al., 2019). Attributed to increases in marine primary production, the expression of this event varies regionally in its nature, time of onset and duration (Diester-Haass et al., 2006). The Biogenic Bloom coincides

with the Late Miocene Carbon Isotope Shift (LMCIS) – the last significant carbon isotope shift seen across all ocean basins (Drury et al., 2017). The causes of these two events are uncertain, although there are some explanations that focus on the movement of terrestrial matter to the marine realm and an increase in nutrients in the oceans, as well as a shift from C_3 to C_4 vegetation (Grant & Dickens, 2002; Diester-Haass et al., 2006; Herbert et al., 2016; Drury et al., 2018).

On the long-term cooling trend from the Miocene to Recent, the mid-Piacenzian Warm Period (mPWP) in the Pliocene, at 3.264-3.025 Ma, is a major target for palaeoclimate studies as a future climate analogue (Haywood et al., 2013; Haywood et al., 2016; Burke et al., 2018). The mPWP had similar CO_2 measurements to today (Seki et al., 2010) and surface temperatures 1.8℃ to 3.6℃ warmer than pre-industrial temperatures (Haywood et al., 2013). However, with the current rates of CO_2 increase, mPWP values may be surpassed by the year 2024/2025 (De La Vega et al., 2020).

Within studies of Pliocene climates, the dynamics of the Indo-Pacific system have been a major focus, with the suggestion of 'permanent El Niño'-like conditions, or 'El Padre', present during the early Pliocene (Ravelo et al., 2004; Wara et al., 2005; Fedorov et al., 2006; Ford et al., 2015). In the modern system, there are distinct gradients in SSTs and thermocline depths between the Western and Eastern Equatorial Pacific (WEP and EEP respectively) during non-El Niño years (Philander, 1990). The WEP is dominated by the West Pacific Warm Pool (WPWP), with a deep thermocline ($\sim$200-400 m) that shallows towards the EEP ($\sim$50 m), where cool, sub-thermocline water upwells to the surface (Ravelo et al., 2006). This asymmetry in surface ocean characteristics is strongly coupled to the strength of the easterly trade winds, part of the tropical Walker Cell (Philander, 1990; Lau & Yang, 2003). These trade winds break down during El Niño events, with surface temperatures off the coast of South America warming as WPWP waters move eastwards, causing a reduction of upwelling and a reduction in the east-west SST gradient. This change in surface ocean water masses also shifts the location of the major up- and down-going regions of the atmo-

spheric Walker circulation, causing east-west migrations of the major centres of rainfall and drought. These regular inter-annual variations in the WEP to EEP SST gradient, known as the El Niño Southern Oscillation cycle (ENSO), characterize the climates of the modern tropical Pacific Ocean. Palaeoclimate studies, specifically records of SSTs in the WEP and EEP and reconstructions of thermocline depths, show that the modern east-west SST gradient only developed during the late Pliocene to Pleistocene (Zhang et al., 2014) and is associated with intensified Hadley and Walker circulation across the Pliocene-Pleistocene transition (Etourneau et al., 2010).

The onset of extensive Northern Hemisphere Glaciation (NHG) occurred from 3.6 million years ago, and was recorded in the benthic δ^{18}O record as more distinct, positive values during glacial stages, indicating a build-up of ice sheets in the Northern Hemisphere (Mudelsee & Raymo, 2005). The subsequent intensification of the NHG (iNHG) at 2.7 Ma signalled a time where the 41kyr world of glacial-interglacial cycles was amplified (Ruggieri et al., 2009). The cause of this intensification is still under debate, but one suggestion is that the presence of permanent El Niño conditions prior to the iNHG could have inhibited glaciation (Wara et al., 2005; Fedorov et al., 2006).

The modern east-to-west aasymmetry seen in the WEP and EEP fully started to develop around 2.5 Ma, with the cooling of the EEP; however, a zonal difference was increasing from $\sim$3 Ma (Wara et al., 2005; Fedorov et al., 2006). However, the link between NHG, iNHG and the development of the modern ENSO system is still ambiguous.

Within the Pleistocene, the Mid-Pleistocene Transition (MPT) marks a shift in the Earth's response to orbital forcing between 1.2-0.8 Ma (Medina-Elizalde & Lea, 2005; Chalk et al., 2017). There is a transition to higher amplitude glacial-interglacial cyclicity in the Pleistocene and a shift in period, from 40 kyr to 100 kyr cycles. However, the cause of this major transition is still uncertain, with further modelling work needed (Berends et al., 2021).

The long-term records over the Miocene to Recent generated in this study will

provide more detail over these major climatic transitions. Although this record does not capture orbital scale variations, it is enough of an improved resolution on the previous most high-resolution studies (Bolton & Stoll, 2013; Bolton et al., 2016) to suggest how or if these major changes had any impact on the coccolith vital effects records.

4.2 Methodology

The novel method described in Chapter 2 for splitting samples was employed in this study for the analysis of stable isotopes and particle size distribution. In brief, samples were washed through a 63 μm then a 20 μm Endecotts Laboratory Test Sieve using deionized (DI) water, with the < 20 μm material being collected. Sediment at this point was in suspension in water. These were then centrifuged in a Mistral 1000 Centrifuge for 6 minutes at 4000 rpm, with the excess water being poured off. When fully centrifuged, samples were left to dry in an oven at 50℃ overnight until fully dry. Once dry, the samples were separated into 4 targeted size fractions: VF, F, M, and VC. The VF (very fine) and VC (very coarse) are the only size fractions that were analysed.

4.2.1 *Sample selection*

Fifty-nine sediment samples analysed in this study were taken from IODP Expedition 363, Site U1482, on the north-west margin of Australia at 15°3.32'S, 120°26.10'E in 1466m water depth (Rosenthal et al., 2018) (Fig. 4.2).

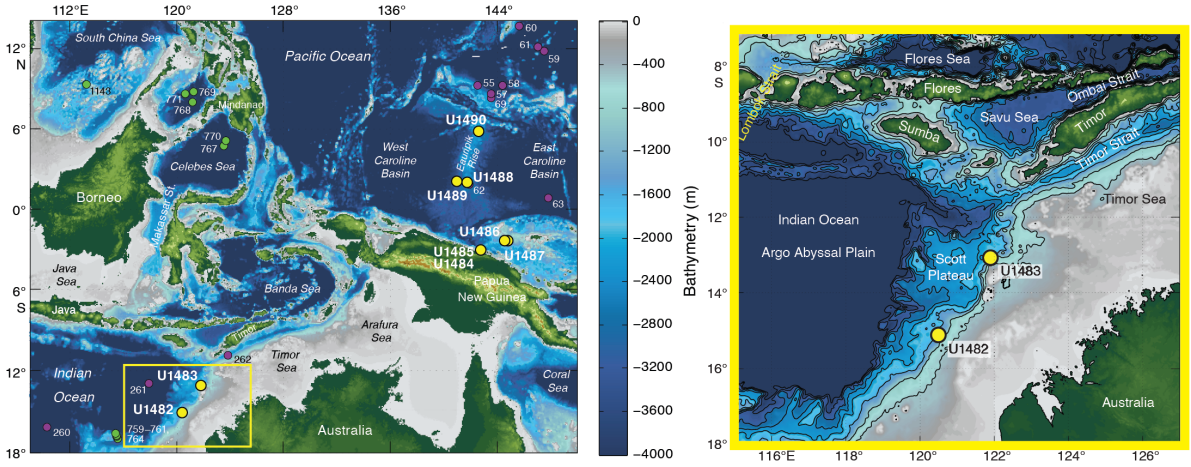


Figure 4.2: Site U1482 bathymetric map showing Site U1482, Exp. 363, modified from Rosenthal et al. (2018). The yellow circle on the right panel indicates the site. The yellow box around the right panel represents the area in the yellow square in the left panel.

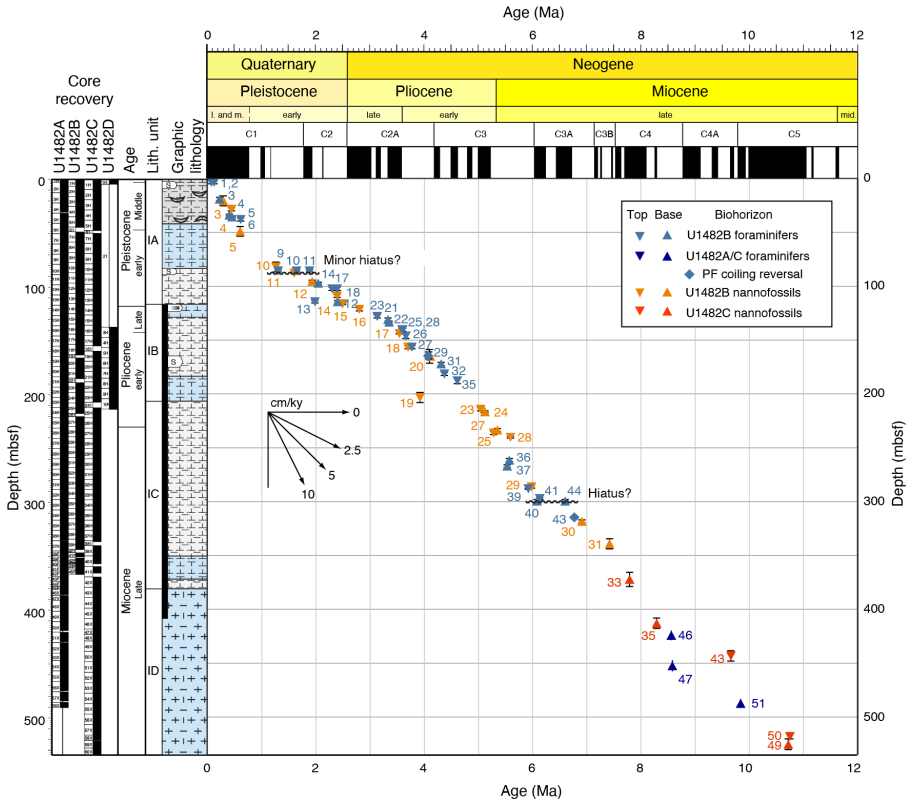


Figure 4.3: Site U1482 age-depth plot for calcareous nannofossil and planktonic foraminifera biohorizons (Rosenthal et al., 2018). Average sedimentation rates are 5.9 cm/ky during the late Miocene, 3.3 cm/ky in the early Pliocene, and 7 cm/ky in the Pleistocene (Rosenthal et al., 2018).

The samples span an age range from 0.1 to 7.7 Ma, with an average temporal resolution of ∼65 Ka, with the shortest interval being ∼36 Ka and the longest ∼1030 Ka, following the age model created with shipboard biostratigraphy and paleomagnetic stratigraphy (Rosenthal et al., 2018) (Fig. 4.3). Samples were taken between 8.05 and 423.25 CCSF-A-m from the secondary splice (Rosenthal et al., 2018), paired with samples for organic geochemistry analysis taken by Prof. Yige Zhang (Texas A&M University). Nannofossil sample tubes were within a 3 cm gap of the organic geochemistry samples, and the ages are calculated for the midpoint of the organic geochemical sample. The characteristics of the sediment was a clay-rich and foraminifer-rich nannofossil ooze, a clay-rich foraminifer nannofossil ooze and a nannofossil ooze (Rosenthal et al., 2018).

4.2.2 *Stable isotope analysis*

Stable isotope analysis was conducted on the split samples, where the VF and VC fractions were analysed and 118 samples (59 VF, 59 VC) were analysed at the BGS Stable Isotope Facility, Keyworth, Nottingham, on a VG Optima mass spectrometer (standard reproducibility of < ± 0.1%). All data are reported to the Vienna Pee Dee Belemnite (VPDB) standards. The sample went through a plasma ashing process at BGS, a widely used process to remove organic matter from samples, before being analysed. Sample material was powdered to yield CO_2 from the equivalent of 10 mg of 100% calcite and reacted with anhydrous phosphoric acid in vacuo overnight at a constant 25℃. Liberated CO_2 was separated from water vapour under vacuum and collected for analysis.

4.2.2.1 Carbon isotopes

Carbon naturally occurs in three isotopic forms, of which two are stable (^{12}C and ^{13}C) and one which is radioactive (^{14}C). They occur in different concentrations in the natural environment: ^{12}C at 98.9%, ^{13}C at 1.1% and ^{14}C which occurs in trace amounts. The

presence of the latter is used in organic materials to radiocarbon date samples, and has been widely used in geological, archaeological, and palaeontological studies for this. The $^{13}C/^{12}C$ ratio of a sample whether it is, for example, bulk sediment or foraminifera, is measured and compared to the $^{13}C/^{12}C$ ratio of a known standard, in this case a laboratory standard calcite. Carbon isotopes ($\delta^{13}C$) are reported as a per mille (‰) difference to the VPDB standard (equation below).

$$\delta^{13}C = \frac{^{13}C/^{12}C_{sample} - ^{13}C/^{12}C_{standard}}{^{13}C/^{12}C_{standard}} X1000$$

4.2.2.2 Oxygen isotopes

Oxygen naturally occurs in three stable isotopic forms: ^{16}O, ^{17}O and ^{18}O. They occur in different concentrations in the natural environment: ^{16}O at 99.763%, ^{17}O at 0.0375% and ^{18}O at 0.1995%. The $^{18}O/^{16}O$ ratio of a sample is measured and compared to the $^{18}O/^{16}O$ of a known standard, in this case a laboratory standard calcite. Oxygen isotopes ($\delta^{18}O$) are reported as per mille (‰) relative to the standard (equation below). If the δ is positive, then it indicates enrichment of the heavier isotope relative to the standard. Contrarywise, if the δ value is negative, then there is a depletion of the heavier isotope.

$$\delta^{18}O = \frac{^{18}O/^{16}O_{sample} - ^{18}O/^{16}O_{standard}}{^{18}O/^{16}O_{standard}} X1000$$

4.2.3 *Particle size analysis*

Particle size analysis was conducted on both VF and VC size fractions using slides prepared following the technique of Flores & Sierro (1997). Slides were imaged using a Zeiss AxioScope A.1 at 1000x magnification with circular polarisation, and a Märzhäuser Wetzlar motorised XYZ stage with 20-30 fields of view (FOV) taken. Images were then processed using Fiji (Schindelin et al., 2012), a version of ImageJ that facilitates the determination of particle size distributions. Any particle less than 1 μm^2 or greater than 80 μm^2 were excluded. A further in-depth description of this method

can be found in Chapter 2.

4.3 Results

4.3.1 *Stable isotope analysis - $\delta^{13}C$*

The $\delta^{13}C_{VF}$ signal remains relatively stable though time, with values between 2.35 ‰ and -0.29 ‰, a range of 2.64 ‰. The $\delta^{13}C_{VF}$ is stable between 7.7 and 5 Ma, followed by a slightly decreasing trend from ∼5 to 3.75 Ma. After this, the $\delta^{13}C_{VF}$ has an overall increasing trend for the remainder of the record. The $\delta^{13}C_{VC}$ signal is more variable, with values between 1.31 ‰ and -2.65 ‰, a range of 3.96 ‰. $\delta^{13}C_{VC}$ shows an overall decreasing trend for the first half of the record, with a decrease in values from 1.31 ‰ to -2.65 ‰. This is then followed by a generally increasing trend from 3.91 Ma to Recent. For most of the record, the $\delta^{13}C_{VF}$ and the $\delta^{13}C_{VC}$ show similar patterns of temporal variability (Fig. 4.4c).

The difference between $\delta^{13}C_{VF}$ and $\delta^{13}C_{VC}$ was calculated for all samples as:

$$\Delta\delta^{13}C = \delta^{13}C_{VF} - \delta^{13}C_{VC}$$

LOESS smoothing (locally weighted smoothing) was applied to $\Delta\delta^{13}C$ to make trends in this relationship clear (Fig. 4.4d). On the LOESS regression curve, the $\Delta\delta^{13}C$ is smallest at 7.7 Ma (0.03 ‰) and at ∼1.8 Ma (∼0.75 ‰), and largest at ∼4 Ma (3.2 ‰). The overall trend seems to be an increase in $\Delta\delta^{13}C$ from 7.7 Ma to ∼4 Ma, followed by a decrease from ∼4 Ma to ∼1.8 Ma, and then it remains stable till the recent.

4.3.2 *Stable isotope analysis - $\delta^{18}O$*

The $\delta^{18}O_{VF}$ record includes values between 0.44 ‰ and -1.09 ‰, a range of 1.53 ‰ (Fig. 4.4e). During the first half of the record (∼7.7 to ∼3.5 Ma), the $\delta^{18}O_{VF}$ is stable, or shows a very slight decreasing trend, but then significantly steps up in values between 3.5 and 3.0 Ma, with a step of 0.93 ‰. For the remainder of the record (3.0 to 0.1 Ma),

$\delta^{18}O_{VF}$ shows a slight trend to higher values through time. The trends in the $\delta^{18}O_{VC}$ are somewhat similar to those of $\delta^{18}O_{VF}$, although without the significant positive step-change at ~3.0-3.5 Ma. The $\delta^{18}O_{VC}$ values are consistently lighter than $\delta^{18}O_{VF}$, with values between -0.66 ‰ and -1.78 ‰, a range of 1.12 ‰.

The difference between $\delta^{18}O_{VF}$ and $\delta^{18}O_{VC}$ was calculated for all samples as:

$$\Delta\delta^{18}O = \delta^{18}O_{VF} - \delta^{18}O_{VC}$$

LOESS smoothing (locally weighted smoothing) was applied to $\Delta\delta^{18}O$ to make trends in this relationship clear. Stable isotope data reveals a varying offset between the $\delta^{18}O$ of the different size fractions throughout the time period, with a peak at ~2.9 Ma (~0.9 ‰) just above the step-change towards higher values in $\delta^{18}O_{VF}$. There are three lows; the first at 7.7 Ma, where values are ~0 ‰, at ~3.8 Ma where values are ~0.25 ‰, and at ~1.8 Ma where values are ~0.5 ‰.

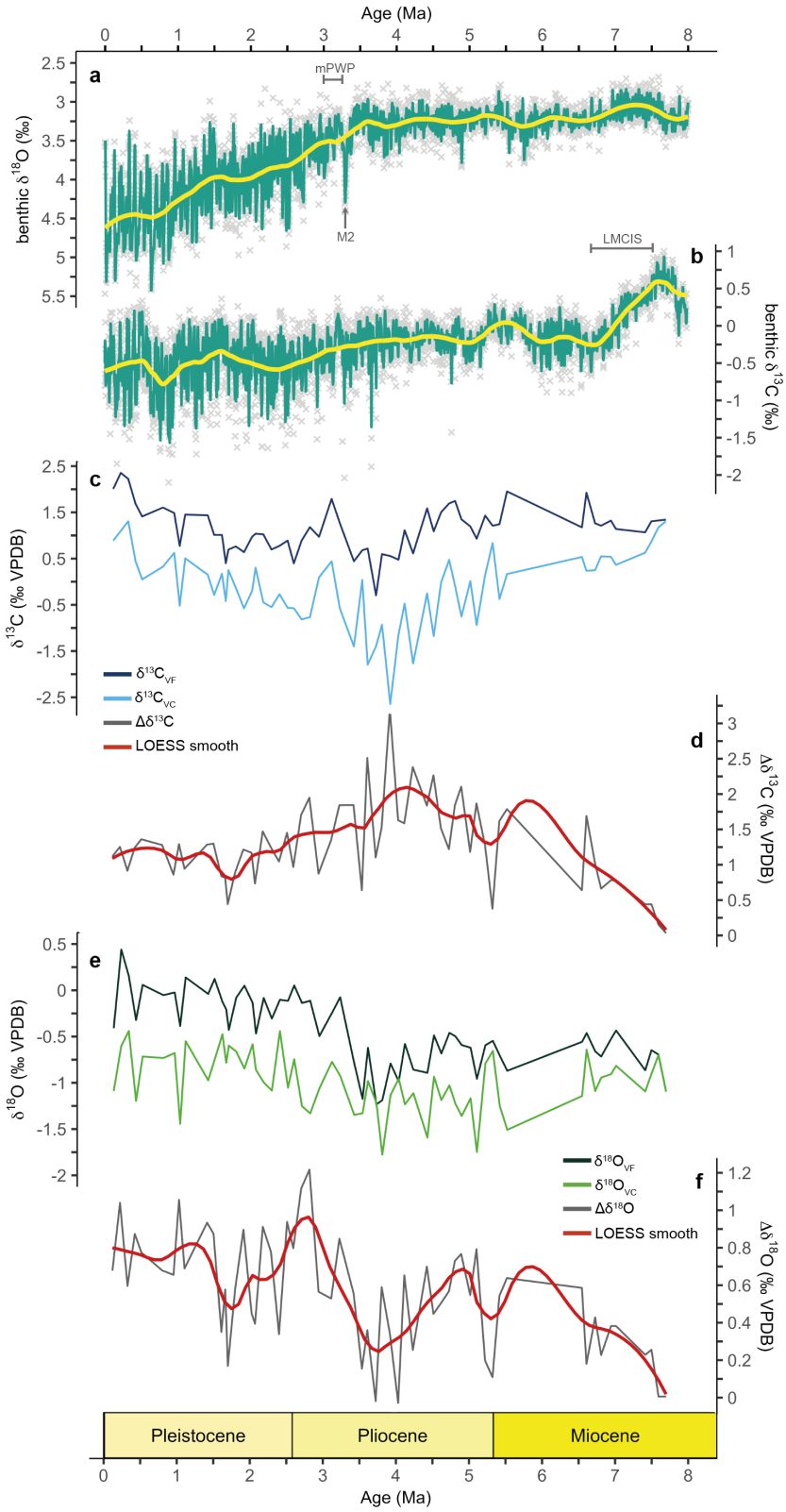


Figure 4.4: Stable isotope measurements ($\delta^{13}C$ and $\delta^{18}O$) of the very fine (VF) and very coarse (VC) size fractions from the Miocene to Recent (*cont. on next page)*

Figure 4.4: Stable isotope measurements from the Miocene to Recent. Panel **a** and **b** are benthic $\delta^{18}O$ and $\delta^{13}C$ showing their respective overall trends since the late Miocene, edited from (Westerhold et al., 2020). The yellow line indicates a 1-million-year LOESS smoothed trend line. Significant events are highlighted, including the mPWP (mid-Piacenzian Warm Period) and the M2 glaciation on panel **a**, and the LMCIS (Late Miocene Carbon Isotopic Shift) on panel **b**. Note the reversed axis on panel **a**. Panel **c** shows carbon isotopic signal of the VF (dark blue) and the VC (light blue) size fraction. Panel **d** shows the difference between the $\delta^{13}C$ for the VF and VC fractions ($\delta^{13}C_{VF} - \delta^{13}C_{VC}$). Note that the red line is LOESS smoothing with a span of 0.2. Panel **e** shows the oxygen isotopic signal for VF (dark green) and VC (light green). Panel **f** shows the difference between $\delta^{18}O$ for the VF and VC fractions ($\delta^{18}O_{VF} - \delta^{18}O_{VC}$). Note that the red line is LOESS smoothing with a span of 0.2.

4.3.3 *Particle size analysis*

Particle size analysis of the VF and VC fractions shows a generally good split between them; the VF fraction tends to have a smaller average particle size (μm^2) than the VC fraction throughout the time period (Fig. 4.5a). The VF average particle size ranges from 2.24 μm^2 to 5.69 μm^2. The VC average particle size ranges from 3.21 μm^2 to 9.2 μm^2. There are two VC samples at 6.55 and 6.81 Ma that are larger than the rest of the VC samples, with average particles sizes of 8.08 μm^2 and 9.2 μm^2. This is most likely due to a combination of clumping of liths on the slide and the threshold that was set (outlined in Chapter 2) was slightly too low, artificially making particles larger. Overall, the VF size fraction average particle size stays relatively stable from 7.7 Ma to 0.1 Ma, whereas the VC fraction average particle size remains stable from 7.7 Ma until $\sim$3.5 Ma, before decreasing from $\sim$3.5 to 2 Ma and remaining stable until 0.1 Ma. The relationship of the average particle size against the $\delta^{13}C$ values shows that the VC fraction $\delta^{13}C$ is mostly more negative than the $\delta^{13}C$ of the VF fraction (Fig. 4.5b).

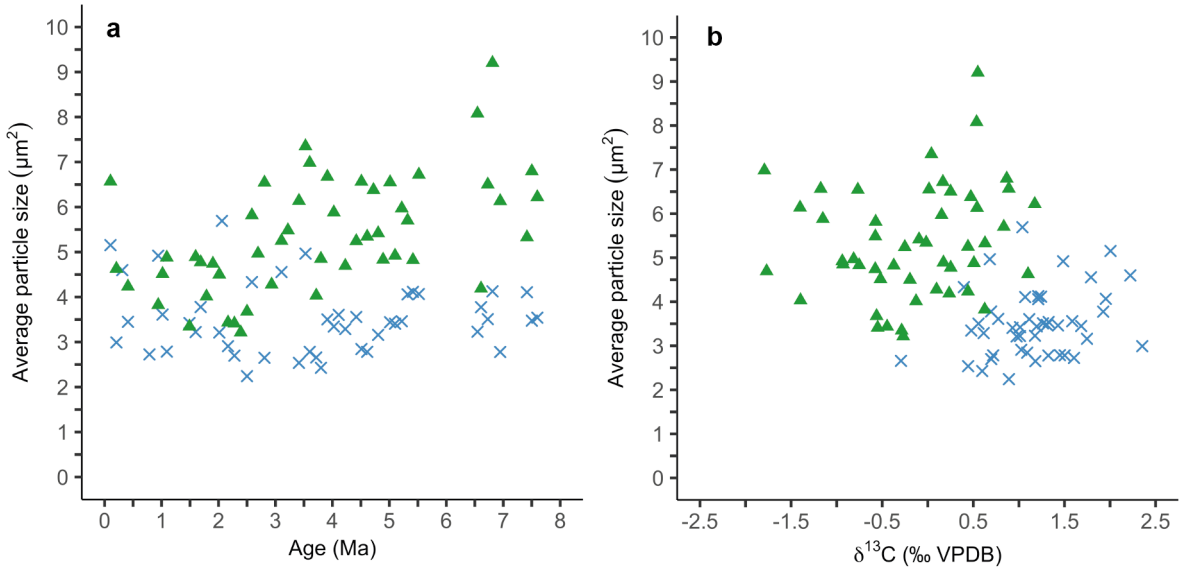


Figure 4.5: Panel **a** shows average particle size (μm^2) throughout the late Miocene to Recent, panel **b** shows the average particle size versus the $\delta^{13}C$ measurement. The VF is represented by the blue crosses and the VC by the green triangles.

4.3.4 *Size corrections of $\delta^{13}C$*

Using the same methodology described in Chapter 3, an initial attempt at correcting for variability in size and mass distributions between the size fraction separates was conducted, assuming a linear trend between coccolith size fraction isotopic values and coccolith size (the average area of the particles).

Similarly, to those corrected in the Pliocene-Pleistocene transition study, there is reduced variation on corrected samples where there is a larger (> 2 μm^2) size differential offset (Fig. 4.6). When there is a small size differential offset (< 2 μm^2), the use of the correction causes a consistent bias towards greater isotopic offsets, particularly as the size offset moves towards zero (Fig. 4.6). This is because the raw isotopic offsets do not change with the mean size differential, so as the size differential reduces, the gradient of the size-isotopic composition line increases as the size differential moves closer to 0, leading to a larger gradient.

However, in the samples used for the size corrections, there are 2 samples

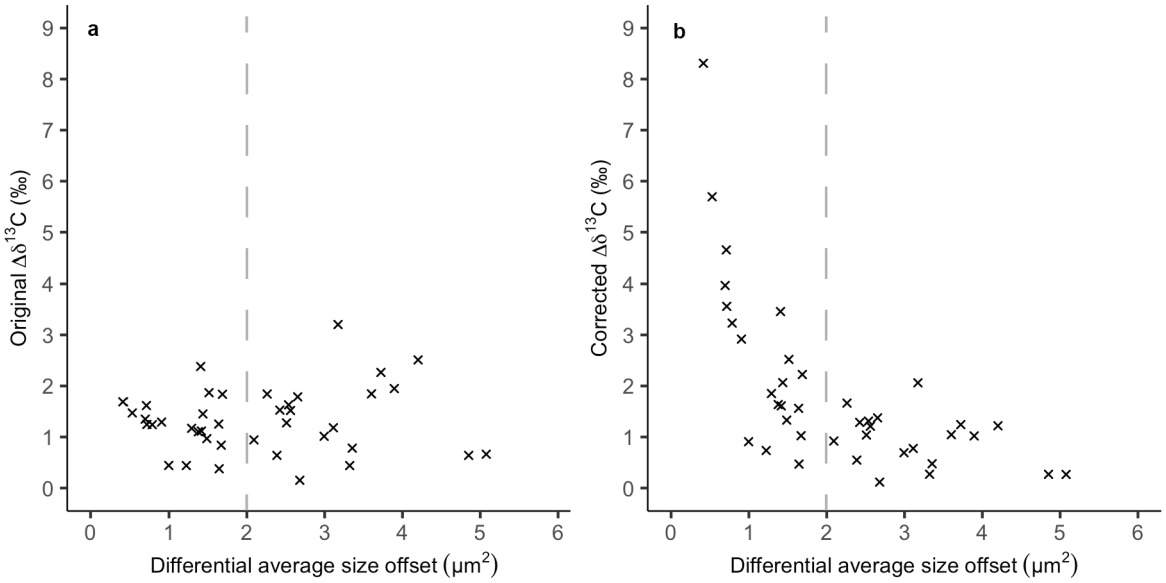


Figure 4.6: Average differential size offset (area) between the VF and VC fraction versus $\Delta\delta^{13}$C. The grey dashed line in both A and B denotes 2 μm^2 differential size offset. Note both panels are on the same $\Delta\delta^{13}$C scale. Panel **a** shows the original $\Delta\delta^{13}$C between the VF and VC fraction versus average area offset. Panel **b** shows the corrected $\Delta\delta^{13}$C between the VF and VC versus the average area offset. In those samples with a > 2 μm^2 differential size offset, the correction reduces sample intervariability. If the size offset is < 2 μm^2, the correction splays the results, biasing them to bigger isotopic offsets.

that have a larger average area in the VF fraction than the VC fraction, but still have the isotopic signature expected of them (VF more positive, VC more negative). This led to negative corrected $\Delta\delta^{13}$C values, with one sample having a corrected -35 ‰ isotopic offset with a -0.07 μm^2 average area offset, and the other with a corrected -1.6 ‰ isotopic offset with a -1.09 μm^2 average area offset. As with the samples with the expected relationship of larger average area in the VC fraction than the VF fraction, the closer to zero the differential offset is, the more biased towards greater isotopic offsets. These samples have not been plotted in Fig. 4.6 to allow for the trends towards biasing in smaller offsets to be fully visible.

4.4 Discussion

4.4.1 *Coccolith size-fraction stable isotopes and geochemistry*

Our results follow on and confirm the large (> 1 ‰) $\delta^{13}C$ isotopic offset seen between large and small coccolith size fractions from the late Miocene to Recent (Bolton & Stoll, 2013; Bolton et al., 2016). When data from ODP Site 925 (tropical Atlantic Ocean) (Bolton et al., 2016) is plotted alongside data collected in this study, they plot consistently well together and follow the same overall pattern (Fig. 4.7a). The $\delta^{13}C_{VC}$ from our study reaches its most negative values at 4 Ma. In comparison, a further study of size separated coccolith $\delta^{13}C$ at ODP Site 999 (the Caribbean Sea) (Bolton & Stoll, 2013), the 9-12 μm $\delta^{13}C$ of coccoliths also reach their most negative values at 4 Ma, and the 10-12 μm $\delta^{13}C$ reach their most negative slightly earlier, at 5 Ma. The 1 ‰ offset begins at ∼7 Ma in our study, similar to those sites in the tropical Atlantic Ocean (Bolton & Stoll, 2013; Bolton et al., 2016). At cold-water sites, the threshold was met slightly later at 5 Ma, due to the solubility of CO_2 being higher in cold waters (Bolton & Stoll, 2013). The Bolton et al. (2016) study is the most recent and highest resolution study of $\delta^{13}C$ from size separated coccoliths over the late Miocene to Recent interval, and contains 16 sampling intervals (both the small (3-5 μm) and large (8-10 μm) coccoliths), whereas this study has 119 samples intervals.

Coccolithophores utilise carbon for both calcification and photosynthesis, and when they are grown under CO_2 limiting conditions, their calcite plates show a wide range of carbon and oxygen isotopic values (Dudley et al., 1986; Ziveri et al., 2003). These deviations from the expected isotopic values of inorganic calcite are called 'vital effects'. In the data presented here, it is clear that these vital effects increase significantly between 7 and 5 Ma. Following previous interpretations, this is thought to represent a threshold response by coccolithophores to declining atmospheric pCO_2 levels, whereby intra-cellular HCO_3^- (bicarbonate) is reallocated from calcification to photosynthesis (Bolton & Stoll, 2013). In this situation, larger cells have a smaller sur-

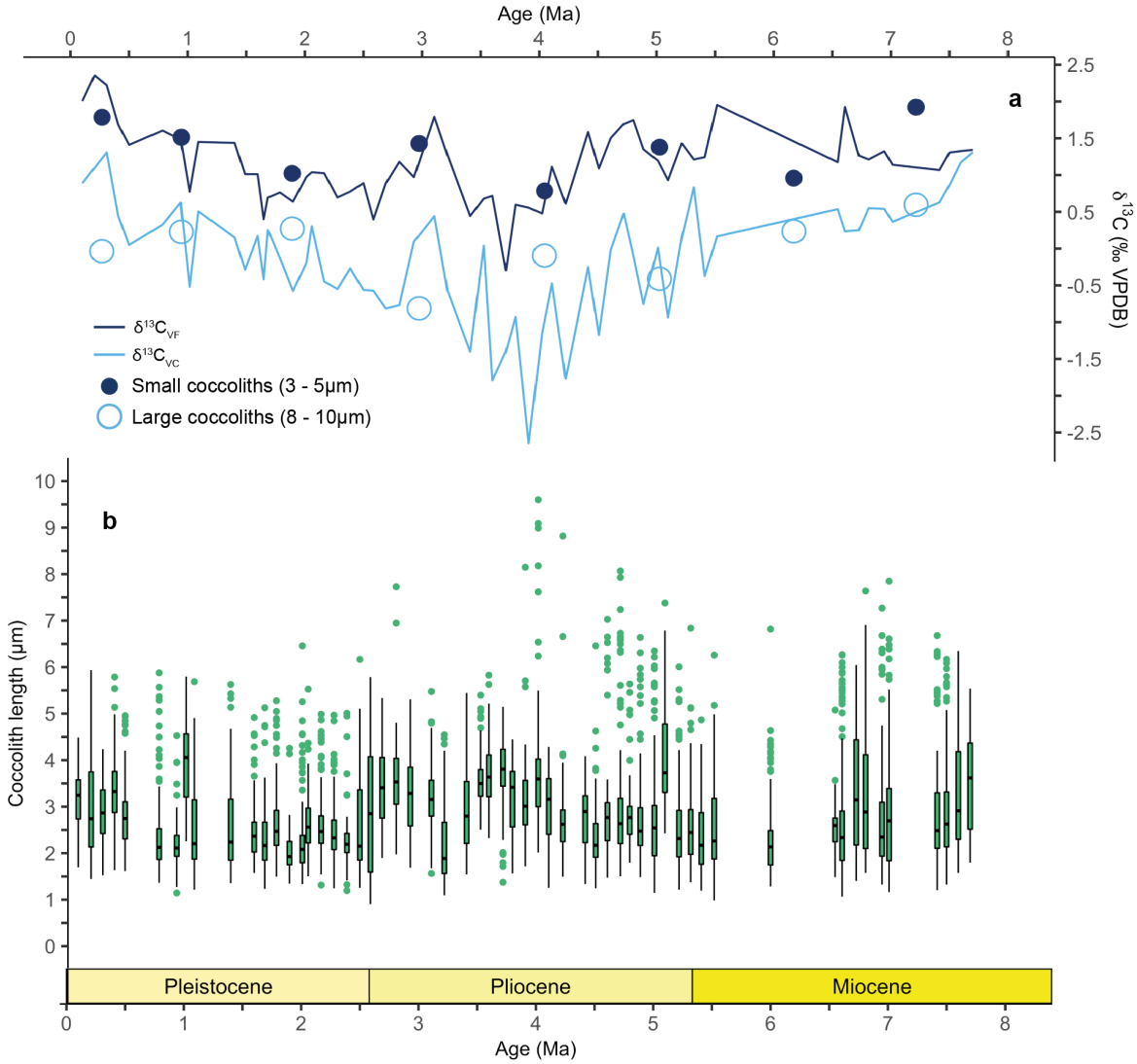


Figure 4.7: δ^{13}C and size data for Reticulofenestrids for the same period for U1482. Panel **a** shows δ^{13}C of the VF (dark blue line) and VC (light blue line) from this study. From Bolton et al. (2016): small coccoliths (3-5 µm, dark blue circle) and large coccoliths (8-10 µm, light blue open circle) δ^{13}C record over same time period. B) Box-whisker plot containing *Reticulofenestra* length measurements from Site U1482, Exp 363 (pers. comm. Mariem Saavedra Pellitero & Tom Dunkley Jones).

face area to volume ratio, making them less efficient at diffusive uptake of CO_2, and more sensitive to CO_2 limitation. Larger cells are thus required to use more bicarbonate for photosynthesis, resulting in coccolith isotopic signatures that are more negative in comparison to the smaller cells. This is supported by culture experiments, where large-celled coccolithophores (*Coccolithus pelagicus* spp. *braarudii*) preferentially in-

crease HCO_3^- transport for photosynthesis instead of for calcification, resulting in lower $\delta^{13}C$ and $\delta^{18}O$ values when compared to small cell species (*Gephyrocapsa oceanica* and *Emiliania huxleyi*) (Rickaby et al., 2010; Bolton & Stoll, 2013). When cultured at increased DIC concentrations with a constant pH, these differences between the large and small cells disappears (Rickaby et al., 2010). In the fossil record, reduced allocation to calcification was first seen in larger cells around 8 million years ago (Bolton et al., 2016). The smaller cells, in contrast, indicate a stable HCO_3^- allocation to the coccolith vesicle in relation to calcification, represented by a stable and near constant $\varepsilon_{coccolith}$ (carbon isotopic fractionation in calcification) (Bolton et al., 2016). This can be seen in our data, where the $\delta^{13}C_{VF}$ is relatively stable through time, but the $\delta^{13}C_{VC}$ varies, becoming more negative from 7.7 Ma to 4 Ma - due to that reallocation of HCO_3^- from calcification.

Some of the most notable changes in coccolith isotopic compositions are within the Pliocene, including a considerable decline in $\delta^{13}C_{VC}$ from $\sim$5.32 to 3.91 Ma, followed by a sharp increase until $\sim$3 Ma. The decrease in $\delta^{13}C_{VC}$ coincides with an increasing size range of *Reticulofenestra*, with more specimens in the medium to large size range (> 5 μm), including some reaching over 9 μm in length at $\sim$4 Ma (Fig. 4.7b). These medium to large *Reticulofenestra* then almost disappear after 4 Ma, the time when $\delta^{13}C_{VC}$ returns to more positive values. This increase of larger *Reticulofenestra* is also seen in the north-west Pacific Ocean (Imai et al., 2015), the Indian Ocean (Young, 1990), tropical Atlantic Ocean (Bolton et al., 2016) and the Atlantic and the western Pacific Oceans (Pratiwi & Sato, 2016), and broadly correlates with the re-emergence of the > 5 μm Retic. coccoliths following the '*Reticulofenestra pseudoumbilicus* gap' (Young, 1998).

Extant Noelaerhabdaceae (e.g. *E. huxleyi* and *G. oceanica*) are part of the isotopically 'heavy' group with respect to their coccoliths. Both these commonly cultured species are, however, relatively small coccolithophores, producing small and lightly calcified coccoliths, making it unclear whether their isotopic signatures relate

to their size and calcification or phylogeny. Overall, there is a distinct lack of large Noelaerhabdaceae in extant species, which means there is no living analogue to the large reticulofenestrids of the Miocene and Pliocene. Although Bolton et al. (2016) recorded the lowest thickness of Noelaerhabdaceae since the mid-Miocene 4 million years ago, this was only in coccoliths < 5 μm in length. A recent study measured the *Reticulofenestra* thickness from the Oligocene-Miocene and found that reticulofenestrid average thickness was comparable to *Coccolithus pelagicus* and *Helicosphaera* spp. (Guitián et al., 2022), whose coccoliths are both part of the isotopically 'light' group of modern coccolithophores. Such findings would be consistent with the patterns of $\delta^{13}C_{VC}$ values measured from 5.32 to 3.91 Ma in our study, where an increase in the abundance of the larger, more heavily calcified reticulofenestrids would lead to more negative coccolith $\delta^{13}C$ values as these larger cells become diffusively limited in their uptake of CO_2, and so need to exploit HCO_3^- for photosynthesis.

These trends through the Pliocene indicate the more dynamic interplay between the size distribution of coccolithophore species in any time period and carbon availability – as set by atmospheric CO_2 concentrations – in determining $\Delta\delta^{13}C$. The onset of distinct $\Delta\delta^{13}C$ between large and small coccolith size fractions in the late Miocene has been – probably correctly – interpreted as a response to declining atmospheric CO_2 concentrations not yet recorded in the sparse atmospheric CO_2 record (Bolton & Stoll, 2013)(Fig. 4.8b). However, in our new, higher resolution data, the peak in the Pliocene in $\Delta\delta^{13}C$ is more likely driven by the evolution of larger-sized reticulofenestrid coccolithophores under more stable CO_2 conditions. Such an interpretation fits with recent studies of Eocene $\Delta\delta^{13}C$, where isotopic offsets are still observed, even under CO_2 concentrations substantial higher than the Mio-Pliocene, because coccolith – and inferred coccolithophore cell – sizes were substantially larger, triggering carbon-limitation at higher CO_2 concentrations (Claxton et al., 2022).

There is a larger difference in the $\delta^{13}C_{VF}$ and $\delta^{13}C_{VC}$ in the Pliocene than the Pleistocene (Fig. 4.5a), even though atmospheric CO_2 more than halved, relative

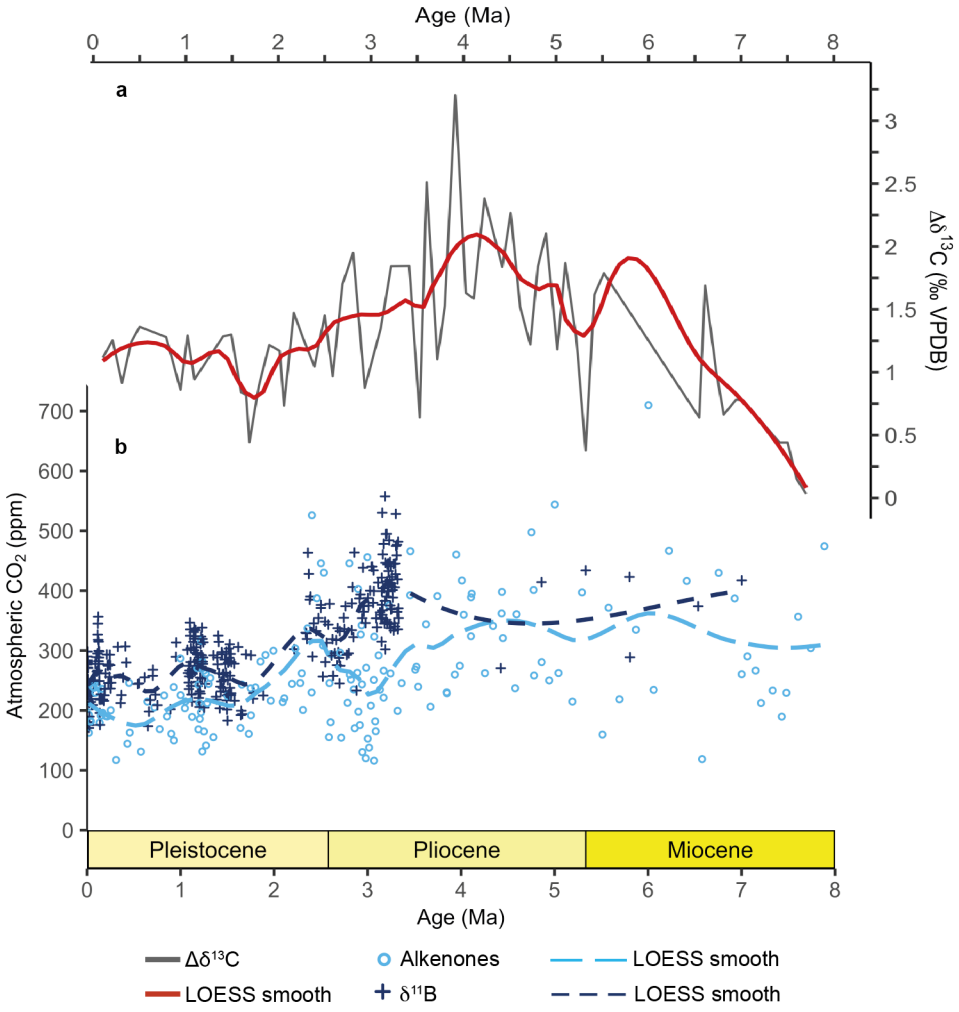


Figure 4.8: $\Delta\delta^{13}C$ and atmospheric CO_2 over the past 8 million years. Panel **a** shows the difference between the VF and VC fraction from this study, panel **b** shows atmospheric CO_2 concentrations, from the Rae et al. (2021) compilation. Light blue empty circles are alkenone measurements, and dark blue crosses are boron isotope measurements. There is a peak in difference at 4 Ma, which we have attributed to larger size reticulofenestrids, and the steady state difference after 4 Ma we have attributed to a dominance of *Gephyrocapsa* in assemblages. *Gephyrocapsa* ameliorates the effects of carbon limitation (reduced $\Delta\delta^{13}C$) despite declining atmospheric pCO_2.

to the Pliocene, in glacial climates of the late Pleistocene. The explanation for this trend in $\Delta\delta^{13}C$ is likely due to the coincident long-term trend towards smaller-sized coccolithophores, similar to those seen in the oceans today, through the Pliocene-Pleistocene. In the Pliocene, with relatively large coccolith and coccolithophore cells, carbon limitation impacted these communities even at higher atmospheric CO_2 concentrations. However, in the Pleistocene, the shift to smaller cells, and potentially dominant

species with more active carbon concentration mechanisms, reduces the isotopic effects of carbon limitation even at low atmospheric CO_2. This hypothesis is supported by coccolith size measurements through time (Fig. 4.5a), where there is a noted decrease in the average particle size of the VC size fraction after 4 Ma, representing the loss of the population of large coccoliths. This observation also fits with the noted crash in bulk carbonate mass accumulation rates after $\sim$4 Ma, ascribed to the overall late Neogene size-reduction trend of coccolithophores (Suchéras-Marx & Henderiks, 2014).

The long-term trends in $\Delta\delta^{13}C$ are important, not only for an understanding of the strength of carbon limitation experienced by coccolithophore communities through time, but also potentially using this understanding to inform estimates of atmospheric CO_2 based on coccolithophores-derived alkenone biomarkers (Rae et al., 2021). The alkenone CO_2 proxy relies on the relationship between the isotopic fractionation of carbon taking place during photosynthesis and the extent of carbon limitation, with greater isotopic fractionation alongside increased carbon availability. Recent studies have strongly indicated that this relationship breaks down within the Pleistocene to modern oceans when extreme carbon limitation is counter-acted by small cell sizes and active uptake mechanism in the gephyrocapsid clade (Badger, 2021). The results of $\Delta\delta^{13}C$ presented here support that conclusion – that peak carbon limitation was experienced by coccolithophore communities in the Pliocene, after which the evolution of small, *Gephyrocapsa*-dominated assemblages somewhat ameliorated the effects of carbon limitation driven by declining atmospheric CO_2.

The loss of the large reticulofenestrids at $\sim$4 Ma coincides with the flourishing of *Gephyrocapsa* spp. (Fig. 4.9b) and *Florisphaera profunda* (Jones, 2021; Boscolo-Galazzo et al., 2022), both of which are prolific in the late Pliocene-Pleistocene oceans. *Florisphaera profunda* is an extant sub-euphotic zone (SEZ) species that lives in tropical to subtropical oceans, below the deep chlorophyll maximum (Hernández-Almeida et al., 2019). Coccolithophores have also become more efficient in nutrient utilisation under nutrient limiting conditions, an adaptive strategy seen in modern oceans. *Emilia-*

nia huxleyi, a modern taxa closely related to *Gephyrocapsa*, is the stronger competitor over the marine diatom *Phaeodactylum tricornutum* under nutrient limiting conditions, at the expense of population growth rates (Zhao et al., 2015). This indicates that *E. huxleyi* has adapted a more economic strategy to dealing with nutrient depleted environments (Zhao et al., 2015). One explanation for this ecological shift in coccolithophore communities in the late Pliocene is a change in ocean biogeochemistry, particularly a deepening of the nutricline (Boscolo-Galazzo et al., 2021). Such a late Pliocene nutricline deepening is inferred from biogeochemical modelling and foraminiferal isotopic data (Boscolo-Galazzo et al., 2021) as well as being consistent with the proliferation of twilight zone species of foraminifera, and the rise of deep-dwelling coccolithophore ecotypes (i.e. *F. profunda*) (Boscolo-Galazzo et al., 2022).

The most striking feature of the δ^{18}O isotope records is the marked increase to more positive values, particularly in the VF fraction, from 3.72 Ma. This isotopic shift coincides with a sharp increase, from < 10% to $\sim$ 30%, in the abundance of *Gephyrocapsa* spp. in the unsplit assemblages from this site (Jones, 2021) (Fig. 4.9a). The VC also exhibits a small increase, but not of the same magnitude as the VF fraction and more gradually. Smaller coccoliths, particularly taxa from the Noelaerhabdaceae family, are concentrated in the VF fraction, and the large change in abundance in *Gephyrocapsa* in the unsplit sediments will be even more pronounced in the VF fraction. This middle Pliocene increase in *Gephyrocapsa* spp. was also noted in Sites from IODP Exp. 356 from 4.42 Ma (Karatsolis et al., 2020), and across the midlatitudes of the Indian and Atlantic Oceans, where it has been described as the 'small *Gephyrocapsa* interval' (Young, 1990; Auer et al., 2019). Analyses of modern *E. huxleyi* and *Gephyrocapsa* coccoliths place them in a distinct isotopically heavy group with respect to δ^{18}O (Dudley et al., 1986), attributed to a high growth and calcification rate (Hermoso et al., 2014; Hermoso et al., 2016b). The change in assemblage over the mid Pliocene, particularly between 3.72 and 3.1 Ma, is thus the most likely driver of the observed change in the size-separated δ^{18}O record. The size separation method employed does not re-

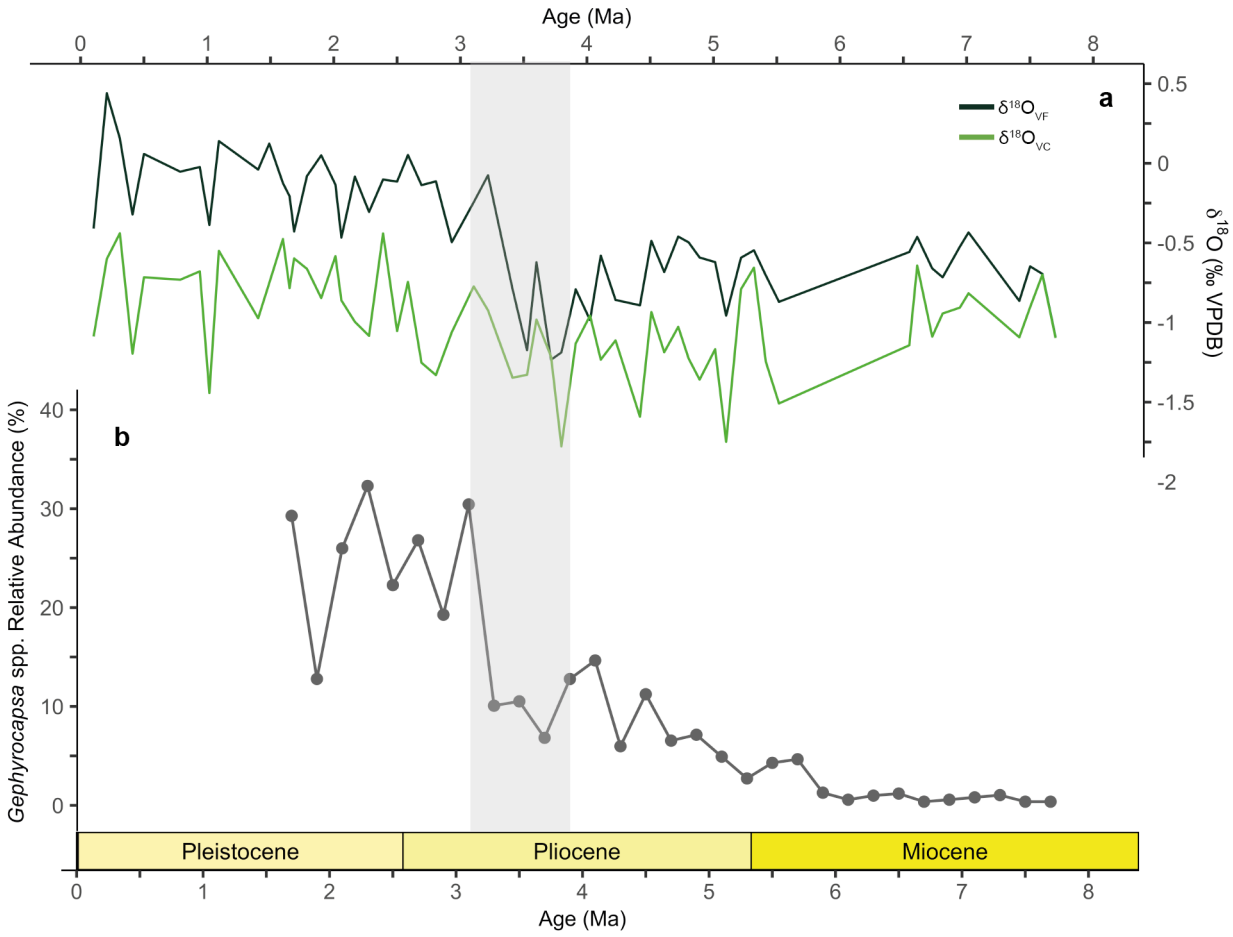


Figure 4.9: $\delta^{18}O$ and *Gephyrocapsa* species abundance since the late Miocene. Panel **a** shows $\delta^{18}O$ of the VF (dark green) and VC (light green) fractions. Panel **b** shows *Gephyrocapsa* spp. abundance from the late Miocene to the mid Pleistocene (1.7 Ma) from Jones (2021). Grey shading denotes period of interest, the 'small *Gephyrocapsa* interval', and the oxygen isotope vital effect splay.

sult in a pure size split sample, and there are often smaller taxa within the VC fraction. However, they constitute a smaller portion of the mass, and so whilst the VF fraction, dominated by *Gephyrocapsa* spp., becomes rapidly more positive, the VC, which will contain *Gephyrocapsa* spp. but other taxa which constitute more of the mass, is only slightly affected. This results in a much more positive $\delta^{18}O$ VF fraction, and a slightly more positive VC fraction. Following this middle Pliocene shift in assemblages, and the associated $\delta^{18}O$ of the size splits, $\delta^{18}O$ values remain relatively constant through the remainder of the Pliocene-Pleistocene, likely as a result of the continued dominance of

Gephyrocapsa spp., with their higher $\delta^{18}O$ values, from the mid Pliocene to the Recent.

VF fractions showing a larger mean particle size by area than VC fractions (2 samples out of 50) could be due to clumping on the smear slide in the VF fraction, making artificially large particles, or it could be due to a general lack of larger particles in the VC fraction. After $\sim$4 Ma to the recent, the VC fraction has a smaller average area than the rest of the record (Fig. 4.5), with a strong decline in average particle size area seen after 4 Ma. This is most likely due to the shift towards smaller cells in the Pleistocene and the proliferation of *Gephyrocapsa* spp. (Fig. 4.9b), with larger coccoliths being relatively sparse. As discussed in Chapters 2 and 3, the size distribution is not necessarily reflective of the mass distribution, so whilst the large coccoliths may be more absent from the assemblage, when they are present their mass will make up a large proportion, which is what is driving the isotopic signatures and offset.

4.5 Conclusion

This study offers the most high-resolution $\delta^{13}C$ and $\delta^{18}O$ for size separated coccolith fractions from the late Miocene to Recent, using a successful novel method. Alongside assemblage data, the study provides insight into the vital effects of coccolithophores in relation to declining atmospheric CO_2 (Bolton & Stoll, 2013; Bolton et al., 2016) and nutricline deepening (Boscolo-Galazzo et al., 2021; Boscolo-Galazzo et al., 2022). The long term macroevolutionary trend of declining cell size and thickness (Bolton et al., 2016), and changes in diversity (Bown et al., 2004) over the Neogene left an imprint on both the $\delta^{13}C$ and $\delta^{18}O$ records. There was a consistent offset in both the $\delta^{13}C$ and the $\delta^{18}O$, due to the presence of vital effects. These vital effects are the result of reallocation of HCO_3^- from calcification to photosynthesis (Bolton & Stoll, 2013), affecting the larger cells the most, making them more negative in both the $\delta^{13}C$ and $\delta^{18}O$. This reflects what is seen in culture studies (e.g. Ziveri et al., 2003; Rickaby et al., 2010; Hermoso et al., 2014; McClelland et al., 2017).

As demonstrated, vital effects can have a profound impact on the $\delta^{13}C$ and

$\delta^{18}O$ measurements. This may need to be considered when working with bulk carbonate analyses. We show that the proliferation of *Gephyrocapsa* spp. affected the $\delta^{18}O_{VF}$ measurement, which would be recorded in bulk carbonate records.

With the application of our novel size-separation technique we have achieved this new, higher-resolution record of late Miocene to Recent coccolithophore isotopic evolution. The honing of this method will open-up the further use of coccolithophore isotopes in palaeoclimatology. When paired with the alkenone CO_2 proxy, it would allow us to study coccolithophore carbon limitation through time. Movements are already being made to using them as a palaeothermometer (Hermoso et al., 2020) and as a pCO_2 indicator rather than as a pCO_2 trend recorder (Godbillot et al., 2022; Claxton et al., 2022), but further work is still needed to both refine size correction and normalisations, as well as our understanding of phylogenetic variations in coccolithophore vital effects.

5 | CONCLUSIONS & FUTURE WORKS

5.1 General conclusions and summary

This thesis employed a novel size separation technique and comprehensively tested it by creating two high-resolution records of size separated coccolith fraction isotope records: one through the Pliocene-Pleistocene Transition, the other from the late Miocene to Recent. All samples were from IODP Exp. 363, Site U1482, off the north-west margin of Australia. These records are the highest resolution over each of the studied time periods and lay excellent groundwork for further research. These records document how climate changes, both on a regional and global scale and as well as macroevolutionary trends, affect the recorded coccolith isotopic signals and productivity indicators. In this chapter, the overall aims of the thesis are addressed, the main findings summarised, and future directions of work proposed.

One of the aims of this thesis was to develop and test a novel size separation technique, based on centrifugation. The most common methods for size separation of the coccolith fraction include micro-filtration (Minoletti et al., 2009) or sinking-decanting (Paull & Thierstein, 1987; Stoll & Ziveri, 2002) techniques, which are very time consuming. By developing a new size separation technique with a much quicker turnaround in sample preparation time, higher-resolution size-separated coccolith records could be generated, leading to a more complete understanding of the isotopic offset seen between large and small coccolith size fractions, and from this produce a better understanding of the magnitude of coccolith vital effects. The robustness of this novel method was tested via coccolith size analysis with Fiji software (Schindelin et al., 2012). Using

circular polarizing transmitted light microscopy, 20-30 fields of view were taken using an automated stage and slide scanning software, with the image output used to determine the particle size distribution by coccolith area. The average area in μm^2 of each size-split was then calculated for each sample. In the vast majority of cases ($\sim$97%), the very fine fraction recorded a smaller average area particle size than the very coarse fraction, implying that this method was successful in generating size-separated coccolith fractions.

Using this novel size separation technique, two new high-resolution records for multiple parameters, including $\delta^{13}C$, $\delta^{18}O$ and Sr/Ca ratios, were generated. The Pliocene-Pleistocene transition record consists of $\delta^{13}C$ and $\delta^{18}O$ records for between 1.38-3.02 million years, with an average temporal resolution of $\sim$4 Ka. A consistent $\sim$1 ‰ offset was seen between the VF and VC fractions for the $\delta^{13}C$ record, which is consistent with other records of $\delta^{13}C$ isotopic offsets of this time period (Bolton et al., 2012; Bolton & Stoll, 2013; Bolton et al., 2016). The $\delta^{18}O$ also recorded an offset through the time period but was slightly more variable than the $\delta^{13}C$ record. Both of these offsets - $\delta^{13}C$ and $\delta^{18}O$ - were retained through orbital scale variations. Both the $\delta^{13}C$ and $\delta^{18}O$ records showed influences from regional climatic changes, with a strong influence from the 41 kyr obliquity cycle in the $\delta^{13}C$ of both size fractions. We recorded a decline to almost 0 ‰ in the $\Delta\delta^{18}O$, which, when paired with a decline in *Florisphaera profunda* coinciding with the large *Gephyrocapsa* interval, we attributed to a restriction of the Indonesian Through Flow and a weakening of the Leeuwin Current. The Pliocene-Pleistocene was also the focus of this study due to the final extinction of the prominent group, the discoasters. Their demise was recorded in the assemblage analysis, with the final extinction of *D. brouweri* occurring at $\sim$1.95 Ma, which is consistent with other studies (Chapman & Chepstow-Lusty, 1997; Raffi et al., 2006; Schueth & Bralower, 2015; Tangunan et al., 2018). The Sr/Ca ratios indicated a stable productivity environment, particularly when looking at the VF fraction. However, the VC fraction was much more varied, which we attributed to the presence of discoasters and other larger and

more heavily calcified liths that have been shown to yield a much larger range of Sr/Ca values than smaller liths. Overall, however, there is no clear signal in any of the coccolith geochemistry that could be interpreted as a major environmental perturbation at this site associated with the *Discoaster* extinction. Finally, a size correction for the $\delta^{13}C$ was attempted, which yielded promising initial results. When there was a large difference in size distribution between VF and VC fractions, this normalization reduced the variance isotopic compositions between samples. However, when there is a small size distribution, the correction causes a consistent bias to greater isotopic offsets. Further work needs to focus on transforming these size distributions into better estimations of mass distributions.

The Miocene to Recent record is of relatively high resolution when compared to other records over this time period (Bolton & Stoll, 2013; Bolton et al., 2016). $\delta^{13}C$ and $\delta^{18}O$ isotope signals were generated for the VF and VC fraction, consisting of 118 samples spanning 7.7-0.1 million years, with an average temporal resolution of $\sim$65 Ka. This study offers the most high-resolution $\delta^{13}C$ and $\delta^{18}O$ record over this time period, again using the novel size separation technique described in Chapter 2. Offsets can be seen throughout the record for the $\delta^{13}C$ and $\delta^{18}O$, apart from in the oldest sample at 7.7 Ma, capturing the emergence of the vital effects between the small and large size coccoliths in the late Miocene. The $\delta^{13}C_{VF}$ remains relatively stable throughout the record, whereas the $\delta^{13}C_{VC}$ moves towards negative values between $\sim$5.32 to 3.91 million years, which we believe mirrors an increase in heavily calcified, large forms of *Reticulofenestra pseudoumbilicus*. There is also a shift in the $\delta^{18}O_{VF}$ that coincides with the rise of *Gephyrocapsa* spp., particularly the small forms. These taxa have more positive $\delta^{18}O$ values, which we believe shifts the average $\delta^{18}O_{VF}$ measurement to more positive values from the late Pliocene onwards.

We believe that in both studies, a key point from the work completed in this thesis is the need to approach bulk $\delta^{13}C$, $\delta^{18}O$ and Sr/Ca ratio records from coccolith rich sediments with caution. The presence of certain taxa could bias the measurements to

positive or negative values, depending on the taxa present in the assemblages or the coccolithophores physiological reaction to the changing climate of the time. However, the size-separation methods used here provide a greater understanding of these vital effects and their consistency through time, which it is hoped, can inform future studies of the drivers of coccolithophore macroevolution and interpretation of coccolithophore-derived biomarker isotopic analyses.

5.2 Further work

Work on IODP Exp. 363, Site U1482 remains an active area of research. Currently there is work to extend the Miocene to Recent study further back in time to fully encapsulate the first records of the vital effects seen in coccolithophores. As stated in Chapter 3, an attempt at size corrections for the $\delta^{13}C$ records has been attempted and yielded promising results. However, it is not a trivial process, and further collaboration with colleagues in the School of Mathematics is ongoing to convert coccolith area distributions to mass distributions and then use these full distributions to correct for sample-to-sample variations in size fractions. Sr/Ca ratios for the Miocene to Recent study are still being analysed, and the return of this data should hopefully give an insight into productivity trends over a key period of macroevolutionary and climatic changes. The records generated in this thesis are representative of a stable, tropical, oligotrophic environment. Similar studies on sites with more variable environments is crucial to see if the signals recorded are mainly a factor of global forcing – such as atmospheric CO_2 – or local oceanographic conditions. However, the samples in this thesis are from an excellent, continuous sedimentary record from the Miocene to the Recent with very good coccolith preservation. This level of completeness across the same age intervals with excellent nannofossil preservation may be hard to find.

REFERENCES

Agnini, C., Monechi, S. & Raffi, I. (2017), 'Calcareous nannofossil biostratigraphy: historical background and application in Cenozoic chronostratigraphy', *Lethaia* **50**(3), 447–463.

Ahn, S., Khider, D., Lisiecki, L. E. & Lawrence, C. E. (2017), 'A probabilistic Pliocene–Pleistocene stack of benthic δ^{18}O using a profile hidden Markov model', *Dynamics and Statistics of the Climate System* **2**(1).

Anthonissen, D. E. & Ogg, J. G. (2012), Appendix 3 - Cenozoic and Cretaceous Biochronology of Planktonic Foraminifera and Calcareous Nannofossils, *in* F. M. Gradstein, J. G. Ogg, M. D. Schmitz & G. M. Ogg, eds, 'The Geologic Time Scale', Elsevier, Boston, pp. 1083–1127.

Aubry, M.-P. (2007), A major Pliocene coccolithophore turnover: Change in morphological strategy in the photic zone, *in* 'Large Ecosystem Perturbations: Causes and Consequences', Geological Society of America.

Auer, G., De Vleeschouwer, D., Smith, R. A., Bogus, K., Groeneveld, J., Grunert, P., Castañeda, I. S., Petrick, B., Christensen, B., Fulthorpe, C., Gallagher, S. J. & Henderiks, J. (2019), 'Timing and Pacing of Indonesian Throughflow Restriction and Its Connection to Late Pliocene Climate Shifts', *Paleoceanography and Paleoclimatology* **34**(4), 635–657.

Backman, J., Raffi, I., Rio, D., Fornaciari, E. & Pälike, H. (2012), 'Biozonation and biochronology of Miocene through Pleistocene calcareous nannofossils from low and middle latitudes', *Newsletters on Stratigraphy* **45**(3), 221–244.

Badger, M. P. S. (2021), 'Alkenone isotopes show evidence of active carbon concentrating mechanisms in coccolithophores as aqueous carbon dioxide concentrations fall below 7μmol L^{-1}', *Biogeosciences* **18**(3), 1149–1160.

Badger, M. P. S., Chalk, T. B., Foster, G. L., Bown, P. R., Gibbs, S. J., Sexton, P. F., Schmidt, D. N., Pälike, H., Mackensen, A. & Pancost, R. D. (2019), 'Insensitivity of alkenone carbon isotopes to atmospheric CO_2 at low to moderate CO_2 levels', *Climate of the Past* **15**(2), 539–554.

Badger, M. P. S., Schmidt, D. N., Mackensen, A. & Pancost, R. D. (2013), 'High-resolution alkenone palaeobarometry indicates relatively stable CO_2 during the Pliocene (3.3–2.8Ma)', *Philosophical Transactions of the Royal Society A: Mathematical, Physical and Engineering Sciences* **371**(2001), 20130094.

Bailey, I., Hole, G. M., Foster, G. L., Wilson, P. A., Storey, C. D., Trueman, C. N. & Raymo, M. E. (2013), 'An alternative suggestion for the Pliocene onset of major northern hemisphere glaciation based on the geochemical provenance of North Atlantic Ocean ice-rafted debris', *Quaternary Science Reviews* **75**, 181–194.

Baumann, K. H. (2004), 'Importance of Size Measurements for Coccolith Carbonate Flux Estimates', *Micropaleontology* **50**, 35–43.

Beaufort, L., Garidel-Thoron, T., Mix, A. C. & Pisias, N. G. (2001), 'ENSO-like Forcing on Oceanic Primary Production During the Late Pleistocene', *Science* **293**(5539), 2440–2444.

Beaufort, L. & Grelaud, M. (2017), 'A 2700-year record of ENSO and PDO variability from the Californian margin based on coccolithophore assemblages and calcification', *Progress in Earth and Planetary Science* **4**(1).

Beaufort, L., Lancelot, Y., Camberlin, P., Cayre, O., Vincent, E., Bassinot, F. & Labeyrie, L. (1997), 'Insolation Cycles as a Major Control of Equatorial Indian Ocean Primary Production', *Science* **278**(5342), 1451–1454.

Beaufort, L., Probert, I., de Garidel-Thoron, T., Bendif, E. M., Ruiz-Pino, D., Metzl, N., Goyet, C., Buchet, N., Coupel, P., Grelaud, M., Rost, B., Rickaby, R. E. & de Var-

gas, C. (2011), ‘Sensitivity of coccolithophores to carbonate chemistry and ocean acidification’, *Nature* **476**(7358), 80–83.

Beltran, C., Rousselle, G., De Rafélis, M., Sicre, M.-A., Labourdette, N. & Schouten, S. (2019), ‘Evolution of the Zonal Gradients Across the Equatorial Pacific During the Miocene–Pleistocene’, *Journal of Sedimentary Research* **89**(3), 242–252.

Bendif, E. M., Nevado, B., Wong, E. L. Y., Hagino, K., Probert, I., Young, J. R., Rickaby, R. E. M. & Filatov, D. A. (2019), ‘Repeated species radiations in the recent evolution of the key marine phytoplankton lineage *Gephyrocapsa*’, *Nature Communications* **10**(1), 1–9.

Berends, C. J., Köhler, P., Lourens, L. J. & Wal, R. S. W. (2021), ‘On the Cause of the Mid-Pleistocene Transition’, *Reviews of Geophysics* **59**(2).

Bollmann, J., Henderiks, J. & Brabec, B. (2002), ‘Global calibration of *Gephyrocapsa* coccolith abundance in Holocene sediments for paleotemperature assessment’, *Paleoceanography and Paleoclimatology* **17**(3), 71–79.

Bolton, C. T., Gibbs, S. J. & Wilson, P. A. (2010), ‘Evolution of nutricline dynamics in the equatorial Pacific during the late Pliocene’, *Paleoceanography and Paleoclimatology* **25**(1), 1–13.

Bolton, C. T., Hernandez-Sanchez, M. T., Fuertes, M. A., Gonzalez-Lemos, S., Abrevaya, L., Mendez-Vicente, A., Flores, J. A., Probert, I., Giosan, L., Johnson, J. & Stoll, H. M. (2016), ‘Decrease in coccolithophore calcification and CO_2 since the middle Miocene’, *Nature Communications* **7**, 10284.

Bolton, C. T. & Stoll, H. M. (2013), ‘Late Miocene threshold response of marine algae to carbon dioxide limitation’, *Nature* **500**(7464), 558–562.

Bolton, C. T., Stoll, H. M. & Mendez-Vicente, A. (2012), ‘Vital effects in coccolith cal-

cite: Cenozoic climate-pCO_2 drove the diversity of carbon acquisition strategies in coccolithophores?', *Paleoceanography and Paleoclimatology* **27**(4).

Boscolo-Galazzo, F., Crichton, K. A., Ridgwell, A., Mawbey, E. M., Wade, B. S. & Pearson, P. N. (2021), 'Temperature controls carbon cycling and biological evolution in the ocean twilight zone', *Science* **371**(6534), 1148–1152.

Boscolo-Galazzo, F., Jones, A., Dunkley Jones, T., Crichton, K. A., Wade, B. S. & Pearson, P. N. (2022), 'Late Neogene evolution of modern deep-dwelling plankton', *Biogeosciences* **19**(3), 743–762.

Bown, P., Lees, J. & Young, J. (2004), Calcareous nannoplankton evolution and diversity through time, *in* H. Thierstein & J. R. Young, eds, 'Coccolithophores: From Molecular Processes to Global Impact', Springer Berlin Heidelberg, Berlin, Heidelberg, pp. 481–508.

Bown, P. R. (2005), 'Calcareous Nannoplankton Evolution: A Tale of Two Oceans', *Micropaleontology* **51**, 299–308.

Bown, P. R. & Young, J. (1998), Techniques, *in* P. R. Bown, ed., 'Calcareous Nannofossil Biostratigraphy', Springer, London, pp. 16–28.

Bralower, T. J. (2002), 'Evidence of surface water oligotrophy during the Paleocene-Eocene thermal maximum: Nannofossil assemblage data from Ocean Drilling Program Site 690, Maud Rise, Weddell Sea', *Paleoceanography and Paleoclimatology* **17**(2), 1–15.

Broecker, W. & Peng, T. (1982), *Tracers in the Sea*, Eldigio Press, Palisanades, N.Y.

Browning, E., Bergen, J. A., Blair, S., Boesiger, T. & de Kaenel, E. (2017), 'Late Miocene to Late Pliocene taxonomy and stratigraphy of the genus *Discoaster* in the circum North Atlantic Basin: Gulf of Mexico and ODP Leg 154', *Journal of Nannoplankton Research* **37**, 189–214.

Bukry, D. (1971), 'Discoaster Evolutionary Trends', *Micropaleontology* **17**(1).

Burke, K. D., Williams, J. W., Chandler, M. A., Haywood, A. M., Lunt, D. J. & Otto-Bliesner, B. L. (2018), 'Pliocene and Eocene provide best analogs for near-future climates', *Proceedings of the National Academy of Sciences* **115**(52), 13288–13293.

Cane, M. A. & Molnar, P. (2001), 'Closing of the Indonesian seaway as a precursor to east African aridification around 3–4million years ago', *Nature* **411**(6834), 157–162.

Cavaleiro, C., Voelker, A. H. L., Stoll, H., Baumann, K.-H. & Kucera, M. (2020), 'Coccolithophore productivity at the western Iberian Margin during the Middle Pleistocene (310–455ka) – evidence from coccolith Sr/Ca data', *Climate of the Past* **16**(6), 2017–2037.

Cerling, T. E., Harris, J. M., Macfadden, B. J., Leakey, M. G., Quade, J., Eisenmann, V. & Ehleringer, J. R. (1997), 'Global vegetation change through the Miocene/Pliocene boundary', *Nature* **389**(6647), 153–158.

Chalk, T. B., Hain, M. P., Foster, G. L., Rohling, E. J., Sexton, P. F., Badger, M. P. S., Cherry, S. G., Hasenfratz, A. P., Haug, G. H., Jaccard, S. L., Martinez-Garcia, A., Palike, H., Pancost, R. D. & Wilson, P. A. (2017), 'Causes of ice age intensification across the Mid-Pleistocene Transition', *Proceedings of the National Academy of Sciences* **114**(50), 13114–13119.

Chapman, M. R. & Chepstow-Lusty, A. J. (1997), 'Late Pliocene climatic change and the global extinction of the discoasters: an independent assessment using oxygen isotope records', *Palaeogeography, Palaeoclimatology, Palaeoecology* **134**(1-4), 109–125.

Chen, Y., Xu, J., Liu, J., Li, T., Xiong, Z., Zhang, P. & Yan, H. (2022), 'Climatic and tectonic constraints on the Plio–Pleistocene evolution of the Indonesian Throughflow intermediate water recorded by benthic δ^{18}O from IODP site U1482', *Quaternary Science Reviews* **295**.

Christensen, B. A., Renema, W., Henderiks, J., De Vleeschouwer, D., Groeneveld, J., Castañeda, I. S., Reuning, L., Bogus, K., Auer, G., Ishiwa, T., McHugh, C. M., Gallagher, S. J. & Fulthorpe, C. S. (2017), 'Indonesian Throughflow drove Australian climate from humid Pliocene to arid Pleistocene', *Geophysical Research Letters* **44**(13), 6914–6925.

Claxton, L. M., McClelland, H. L. O., Hermoso, M. & Rickaby, R. E. M. (2022), 'Eocene emergence of highly calcifying coccolithophores despite declining atmospheric CO_2', *Nature Geoscience* **15**, 826–831.

Colleoni, F., De Santis, L., R. Naish, T., DeConto, R. M., Escutia, C., Stocchi, P., Uenzelmann-Neben, G., Hochmuth, K., Hillenbrand, C.-D., van de Flierdt, T., Pérez, L. F., Leitchenkov, G., Sangiorgi, F., Jamieson, S., Bentley, M. J. & Wilson, D. J. (2022), Past Antarctic ice sheet dynamics (PAIS) and implications for future sea-level change, *in* F. Florindo, M. Siegert, L. D. Santis & T. Naish, eds, 'Antarctic Climate Evolution (Second Edition)', Elsevier, Amsterdam, pp. 689–768.

De La Vega, E., Chalk, T. B., Wilson, P. A., Bysani, R. P. & Foster, G. L. (2020), 'Atmospheric CO_2 during the Mid-Piacenzian Warm Period and the M2 glaciation', *Scientific Reports* **10**(1), 11002.

De Schepper, S., Gibbard, P. L., Salzmann, U. & Ehlers, J. (2014), 'A global synthesis of the marine and terrestrial evidence for glaciation during the Pliocene Epoch', *Earth-Science Reviews* **135**, 83–102.

De Vleeschouwer, D., Auer, G., Smith, R., Bogus, K., Christensen, B., Groeneveld, J., Petrick, B., Henderiks, J., Castañeda, I. S., O'Brien, E., Ellinghausen, M., Gallagher, S. J., Fulthorpe, C. S. & Pälike, H. (2018), 'The amplifying effect of Indonesian Throughflow heat transport on Late Pliocene Southern Hemisphere climate cooling', *Earth and Planetary Science Letters* **500**, 15–27.

De Vleeschouwer, D., Petrick, B. F. & Martínez-García, A. (2019), 'Stepwise Weakening of the Pliocene Leeuwin Current', *Geophysical Research Letters* **46**(14), 8310–8319.

Diester-Haass, L., Billups, K. & Emeis, K. C. (2006), 'Late Miocene carbon isotope records and marine biological productivity: Was there a (dusty) link?', *Paleoceanography and Paleoclimatology* **21**(4), PA4216.

Dowsett, H. J., Foley, K. M., Stoll, D. K., Chandler, M. A., Sohl, L. E., Bentsen, M., Otto-Bliesner, B. L., Bragg, F. J., Chan, W.-L., Contoux, C., Dolan, A. M., Haywood, A. M., Jonas, J. A., Jost, A., Kamae, Y., Lohmann, G., Lunt, D. J., Nisancioglu, K. H., Abe-Ouchi, A., Ramstein, G., Riesselman, C. R., Robinson, M. M., Rosenbloom, N. A., Salzmann, U., Stepanek, C., Strother, S. L., Ueda, H., Yan, Q. & Zhang, Z. (2013), 'Sea Surface Temperature of the mid-Piacenzian Ocean: A Data-Model Comparison', *Scientific Reports* **3**(1).

Drury, A. J., Lee, G. P., Gray, W. R., Lyle, M., Westerhold, T., Shevenell, A. E. & John, C. M. (2018), 'Deciphering the State of the Late Miocene to Early Pliocene Equatorial Pacific', *Paleoceanography and Paleoclimatology* **33**(3), 246–263.

Drury, A. J., Westerhold, T., Frederichs, T., Tian, J., Wilkens, R., Channell, J. E. T., Evans, H., John, C. M., Lyle, M. & Röhl, U. (2017), 'Late Miocene climate and time scale reconciliation: Accurate orbital calibration from a deep-sea perspective', *Earth and Planetary Science Letters* **475**, 254–266.

Dudley, W. C., Blackwelder, P., Brand, L. & Duplessy, J.-C. (1986), 'Stable isotopic composition of coccoliths', *Marine Micropaleontology* **10**(1-3), 1–8.

Dunkley Jones, T., Bown, P. R., Pearson, P. N., Wade, B. S., Coxall, H. K. & Lear, C. H. (2008), 'Major shifts in calcareous phytoplankton assemblages through the Eocene-Oligocene transition of Tanzania and their implications for low-latitude primary production', *Paleoceanography and Paleoclimatology* **23**(4), 1–14.

Dyez, K. A., Honisch, B. & Schmidt, G. A. (2018), 'Early Pleistocene obliquity-scale pCO_2 variability at 1.5 million years ago', *Paleoceanography and Paleoclimatology* **33**(11), 1270–1291.

Etourneau, J., Martinez, P., Blanz, T. & Schneider, R. (2009), 'Pliocene–Pleistocene variability of upwelling activity, productivity, and nutrient cycling in the Benguela region', *Geology* **37**(10), 871–874.

Etourneau, J., Schneider, R., Blanz, T. & Martinez, P. (2010), 'Intensification of the Walker and Hadley atmospheric circulations during the Pliocene–Pleistocene climate transition', *Earth and Planetary Science Letters* **297**(1-2), 103–110.

Fedorov, A. V., Dekens, P. S., McCarthy, M., Ravelo, A. C., deMenocal, P. B., Barreiro, M., Pacanowski, R. C. & Philander, S. G. (2006), 'The Pliocene paradox (mechanisms for a permanent El Niño)', *Science* **312**(5779), 1485–1489.

Fink, C., Baumann, K.-H., Groeneveld, J. & Steinke, S. (2010), 'Strontium/Calcium ratio, carbon and oxygen stable isotopes in coccolith carbonate from different grain-size fractions in South Atlantic surface sediments', *Geobios* **43**(1), 151–164.

Flores, J. A. & Sierro, F. (1997), 'Revised technique for calculation of calcareous nannofossil accumulation rates', *Micropaleontology* **43**(3), 321–324.

Flores, J. A. & Sierro, F. J. (2013), PALEOCEANOGRAPHY, BIOLOGICAL PROXIES | Coccolithophores, *in* S. A. Elias & C. J. Mock, eds, 'Encyclopedia of Quaternary Science (Second Edition)', Amsterdam, pp. 783–794.

Ford, H. L., Ravelo, A. C., Dekens, P. S., Lariviere, J. P. & Wara, M. W. (2015), 'The evolution of the equatorial thermocline and the early Pliocene *El Padre* mean state', *Geophysical Research Letters* **42**(12), 4878–4887.

Godbillot, C., Minoletti, F., Bassinot, F. & Hermoso, M. (2022), 'Parallel between the

isotopic composition of coccolith calcite and carbon levels across Termination II: developing a new paleo-CO_2', *Climate of the Past* **18**(3), 449–464.

Grant, K. M. & Dickens, G. R. (2002), 'Coupled productivity and carbon isotope records in the southwest Pacific Ocean during the late Miocene–early Pliocene biogenic bloom', *Palaeogeography, Palaeoclimatology, Palaeoecology* **187**(1-2), 61–82.

Groeneveld, J., Hathorne, E. C., Steinke, S., DeBey, H., Mackensen, A. & Tiedemann, R. (2014), 'Glacial induced closure of the Panamanian Gateway during Marine Isotope Stages (MIS) 95–100 (2.5 Ma)', *Earth and Planetary Science Letters* **404**, 296–306.

Guitián, J., Fuertes, M. , Flores, J.-A., Hernández-Almeida, I. & Stoll, H. (2022), 'Variation in calcification of *Reticulofenestra* coccoliths over the Oligocene–Early Miocene', *Biogeosciences* **19**(20), 5007–5019.

Hall, R. (2009), 'Southeast Asia's changing palaeogeography', *Blumea - Biodiversity, Evolution and Biogeography of Plants* **54**(1), 148–161.

Hayashi, T., Yamanaka, T., Hikasa, Y., Sato, M., Kuwahara, Y. & Ohno, M. (2020), 'Latest Pliocene Northern Hemisphere glaciation amplified by intensified Atlantic meridional overturning circulation', *Communications Earth & Environment* **1**(1).

Haywood, A. M., Dowsett, H. J. & Dolan, A. M. (2016), 'Integrating geological archives and climate models for the mid-Pliocene warm period', *Nature Communications* **7**(1), 10646.

Haywood, A. M., Hill, D. J., Dolan, A. M., Otto-Bliesner, B. L., Bragg, F., Chan, W. L., Chandler, M. A., Contoux, C., Dowsett, H. J., Jost, A., Kamae, Y., Lohmann, G., Lunt, D. J., Abe-Ouchi, A., Pickering, S. J., Ramstein, G., Rosenbloom, N. A., Salzmann, U., Sohl, L., Stepanek, C., Ueda, H., Yan, Q. & Zhang, Z. (2013), 'Large-scale features of Pliocene climate: results from the Pliocene Model Intercomparison Project', *Climate of the Past* **9**(1), 191–209.

Haywood, A. M., Valdes, P. J. & Peck, V. L. (2007), 'A permanent El Niño-like state during the Pliocene?', *Paleoceanography and Paleoclimatology* **22**(1).

He, Y., Wang, H. & Liu, Z. (2021), 'Development of the Leeuwin Current on the northwest shelf of Australia through the Pliocene-Pleistocene period', *Earth and Planetary Science Letters* **559**.

Hennissen, J. A. I., Head, M. J., De Schepper, S. & Groeneveld, J. (2014), 'Palynological evidence for a southward shift of the North Atlantic Current at $\sim$2.6Ma during the intensification of late Cenozoic Northern Hemisphere glaciation', *Paleoceanography and Paleoclimatology* **29**(6), 564–580.

Herbert, T. D., Lawrence, K. T., Tzanova, A., Peterson, L. C., Caballero-Gill, R. & Kelly, C. S. (2016), 'Late Miocene global cooling and the rise of modern ecosystems', *Nature Geoscience* **9**(11), 843–847.

Hermoso, M. (2014), 'Coccolith-Derived Isotopic Proxies in Palaeoceanography: Where Geologists Need Biologists', *Cryptogamie, Algologie* **35**(4), 323–351.

Hermoso, M. (2015), 'Control of ambient pH on growth and stable isotopes in phytoplanktonic calcifying algae', *Paleoceanography and Paleoclimatology* **30**(8), 1100–1112.

Hermoso, M. (2016), 'Isotopic record of Pleistocene glacial/interglacial cycles in pelagic carbonates: Revisiting historical data from the Caribbean Sea', *Quaternary Science Reviews* **137**, 69–78.

Hermoso, M., Candelier, Y., Browning, T. J. & Minoletti, F. (2015), 'Environmental control of the isotopic composition of subfossil coccolith calcite: Are laboratory culture data transferable to the natural environment?', *GeoResJ* **7**, 35–42.

Hermoso, M., Chan, I. Z. X., McClelland, H. L. O., Heureux, A. M. C. & Rickaby, R.

E. M. (2016a), 'Vanishing coccolith vital effects with alleviated carbon limitation', *Biogeosciences* **13**(1), 301–312.

Hermoso, M., Horner, T. J., Minoletti, F. & Rickaby, R. E. M. (2014), 'Constraints on the vital effect in coccolithophore and dinoflagellate calcite by oxygen isotopic modification of seawater', *Geochimica et Cosmochimica Acta* **141**, 612–627.

Hermoso, M., Lefeuvre, B., Minoletti, F. & de Rafelis, M. (2017), 'Extreme strontium concentrations reveal specific biomineralization pathways in certain coccolithophores with implications for the Sr/Ca paleoproductivity proxy', *PLoS One* **12**(10).

Hermoso, M., McClelland, H.-L. O., Hirst, J. S., Minoletti, F., Bonifacie, M. & Rickaby, R. E. M. (2020), 'Towards the use of the coccolith vital effects in palaeoceanography: A field investigation during the middle Miocene in the SW Pacific Ocean', *Deep Sea Research Part I: Oceanographic Research Papers* **160**, 103262.

Hermoso, M., Minoletti, F., Aloisi, G., Bonifacie, M., McClelland, H. L. O., Labourdette, N., Renforth, P., Chaduteau, C. & Rickaby, R. E. M. (2016b), 'An explanation for the δ^{18}O excess in Noelaerhabdaceae coccolith calcite', *Geochimica et Cosmochimica Acta* **189**, 132–142.

Hermoso, M., Minoletti, F., Le Callonnec, L., Jenkyns, H. C., Hesselbo, S. P., Rickaby, R. E. M., Renard, M., De Rafélis, M. & Emmanuel, L. (2009), 'Global and local forcing of Early Toarcian seawater chemistry: A comparative study of different paleoceanographic settings (Paris and Lusitanian basins)', *Paleoceanography and Paleoclimatology* **24**(4), 1–15.

Hernández-Almeida, I., Ausín, B., Saavedra-Pellitero, M., Baumann, K. H. & Stoll, H. M. (2019), 'Quantitative reconstruction of primary productivity in low latitudes during the last glacial maximum and the mid-to-late Holocene from a global *Florisphaera profunda* calibration dataset', *Quaternary Science Reviews* **205**, 166–181.

Hill, D. J., Bolton, K. P. & Haywood, A. M. (2017), 'Modelled ocean changes at the Plio-Pleistocene transition driven by Antarctic ice advance', *Nature Communications* **8**(1), 14376.

Honisch, B., Hemming, N. G., Archer, D., Siddall, M. & McManus, J. F. (2009), 'Atmospheric carbon dioxide concentration across the mid-Pleistocene transition', *Science* **324**(5934), 1551–1554.

Imai, R., Farida, M., Sato, T. & Iryu, Y. (2015), 'Evidence for eutrophication in the northwestern Pacific and eastern Indian oceans during the Miocene to Pleistocene based on the nannofossil accumulation rate, *Discoaster* abundance, and coccolith size distribution of *Reticulofenestra*', *Marine Micropaleontology* **116**, 15–27.

Jakob, K. A., Bolton, C. T., Wilson, P. A., Bahr, A., Pross, J., Fiebig, J., Kähler, K. & Friedrich, O. (2017), 'Glacial–interglacial changes in equatorial Pacific surface-water structure during the Plio–Pleistocene intensification of Northern Hemisphere Glaciation', *Earth and Planetary Science Letters* **463**, 69–80.

Jin, X., Liu, C., Zhang, H., Zhou, C., Jiang, X., Wu, Z. & Xu, J. (2018), 'Evolutionary driven of *Gephyrocapsa* coccolith isotopic vital effects over the past 400 ka', *Earth and Planetary Science Letters* **503**, 236–247.

Johnson, R., Langer, G., Rossi, S., Probert, I., Mammone, M. & Ziveri, P. (2022), 'Nutritional response of a coccolithophore to changing pH and temperature', *Limnology and Oceanography* **67**(10), 2309–2324.

Jones, A. P. (2021), *Macroevolutionary dynamics and diversity of coccolithophores across long-term cooling periods of the Cenozoic*, University of Birmingham, Birmingham, UK.

Jones, A. P., Dunkley Jones, T., Coxall, H., Pearson, P. N., Nala, D. & Hoggett, M. (2019), 'Low-Latitude Calcareous Nannofossil Response in the Indo-Pacific Warm

Pool Across the Eocene-Oligocene Transition of Java, Indonesia', *Paleoceanography and Paleoclimatology* **34**(11), 1833–1847.

Karas, C., Nürnberg, D., Bahr, A., Groeneveld, J., Herrle, J. O., Tiedemann, R. & Demenocal, P. B. (2017), 'Pliocene oceanic seaways and global climate', *Scientific Reports* **7**(1), 39842.

Karatsolis, B. De Vleeschouwer, D., Groeneveld, J., Christensen, B. & Henderiks, J. (2020), 'The Late Miocene to Early Pliocene "Humid Interval" on the NW Australian Shelf: Disentangling Climate Forcing From Regional Basin Evolution', *Paleoceanography and Paleoclimatology* **35**(9).

Keigwin, L. (1982), 'Isotopic Paleoceanography of the Caribbean and East Pacific: Role of Panama Uplift in Late Neogene Time', *Science* **217**(4557), 350–353.

Kirby, N., Bailey, I., Lang, D. C., Brombacher, A., Chalk, T. B., Parker, R. L., Crocker, A. J., Taylor, V. E., Milton, J. A., Foster, G. L., Raymo, M. E., Kroon, D., Bell, D. B. & Wilson, P. A. (2020), 'On climate and abyssal circulation in the Atlantic Ocean during late Pliocene marine isotope stage M2, $\sim$3.3 million years ago', *Quaternary Science Reviews* **250**.

Lau, K. & Yang, S. (2003), 'Walker Circulation', *Encyclopedia of Atmospheric Sciences* **2505**(2510), 450–454.

Lawrence, K. T., Sosdian, S., White, H. E. & Rosenthal, Y. (2010), 'North Atlantic climate evolution through the Plio-Pleistocene climate transitions', *Earth and Planetary Science Letters* **300**(3-4), 329–342.

Li, M., Hinnov, L. & Kump, L. (2019), '*Acycle*: Time-series analysis software for paleoclimate research and education', *Computers & Geosciences* **127**, 12–22.

Lisiecki, L. E. & Raymo, M. E. (2005), 'A Pliocene-Pleistocene stack of 57 globally

distributed benthic δ^{18}O records', *Paleoceanography and Paleoclimatology* **20**(1), 1–17.

Lunt, D. J., Foster, G. L., Haywood, A. M. & Stone, E. J. (2008), 'Late Pliocene Greenland glaciation controlled by a decline in atmospheric CO_2 levels', *Nature* **454**(7208), 1102–1105.

Lyle, M., Drury, A. J., Tian, J., Wilkens, R. & Westerhold, T. (2019), 'Late Miocene to Holocene high-resolution eastern equatorial Pacific carbonate records: stratigraphy linked by dissolution and paleoproductivity', *Climate of the Past* **15**(5), 1715–1739.

Lübbers, J., Holbourn, A. E., Kuhnt, W. & Beil, S. (2020), Data report: revision of IODP Expedition 363 Site U1482 shipboard sediment splice based on X-ray fluorescence scanning elemental data, *in* 'Western Pacific Warm Pool', Proceedings of the International Ocean Discovery Program.

McClelland, H. L., Bruggeman, J., Hermoso, M. & Rickaby, R. E. (2017), 'The origin of carbon isotope vital effects in coccolith calcite', *Nature Communications* **8**, 14511.

McIntyre, A. & Molfino, B. (1996), 'Forcing of Atlantic Equatorial and Subpolar Millennial Cycles by Precession', *Science* **274**(5294), 1867–1870.

Medina-Elizalde, M. & Lea, D. W. (2005), 'The mid-Pleistocene transition in the tropical Pacific', *Science* **310**(5750), 1009–1012.

Milliman, J. D. (1993), 'Production and accumulation of calcium carbonate in the ocean: Budget of a nonsteady state', *Global Biogeochemical Cycles* **7**(4), 927–957.

Minoletti, F., Gardin, S., Nicot, E., Renard, M. & Spezzaferri, S. (2001), 'Mise au point d'un protocole experimental de separation granulometrique d'assemblages de nannofossiles calcaires; applications paleoecologiques et geochimiques', *Bulletin de la Société Géologique de France* **172**(4), 437–446.

Minoletti, F., Hermoso, M. & Gressier, V. (2009), 'Separation of sedimentary micron-sized particles for palaeoceanography and calcareous nannoplankton biogeochemistry', *Nature Protocols* **4**(1), 14–24.

Molfino, B. & McIntyre, A. (1990), 'Precessional Forcing of Nutricline Dynamics in the Equatorial Atlantic', *Science* **249**(4970), 766–769.

Mudelsee, M. & Raymo, M. E. (2005), 'Slow dynamics of the Northern Hemisphere glaciation', *Paleoceanography and Paleoclimatology* **20**(4), 1–14.

Müller, M. N., Lebrato, M., Riebesell, U., Barcelos E Ramos, J., Schulz, K. G., Blanco-Ameijeiras, S., Sett, S., Eisenhauer, A. & Stoll, H. M. (2014), 'Influence of temperature and CO_2 on the strontium and magnesium composition of coccolithophore calcite', *Biogeosciences* **11**(4), 1065–1075.

Naafs, B. D. A., Stein, R., Hefter, J., Khélifi, N., De Schepper, S. & Haug, G. H. (2010), 'Late Pliocene changes in the North Atlantic Current', *Earth and Planetary Science Letters* **298**(3-4), 434–442.

Pagani, M. (2014), Biomarker-Based Inferences of Past Climate: The Alkenone pCO_2 Proxy, *in* H. D. Holland & K. K. Turekian, eds, 'Treatise on Geochemistry (Second Edition)', Elsevier, Oxford, pp. 361–378.

Pagani, M., Liu, Z., LaRiviere, J. & Ravelo, A. C. (2010), 'High Earth-system climate sensitivity determined from Pliocene carbon dioxide concentrations', *Nature Geoscience* **3**(1), 27–30.

Pattiaratchi, C. (2006), 'Surface and sub-surface circulation and water masses off Western Australia', *Bulletin Australian Meteorological and Oceanographic Society* **19**, 95–104.

Paull, C. K. & Thierstein, H. R. (1987), 'Stable isotopic fractionation among particles

in Quaternary coccolith-sized deep-sea sediments', *Paleoceanography and Paleoclimatology* **2**(4), 423–429.

Petrick, B., Martínez-García, A., Auer, G., Reuning, L., Auderset, A., Deik, H., Takayanagi, H., De Vleeschouwer, D., Iryu, Y. & Haug, G. H. (2019), 'Glacial Indonesian Throughflow weakening across the Mid-Pleistocene Climatic Transition', *Scientific Reports* **9**(1).

Philander, S. (1990), *El Niño, La Niña, and the southern oscillation*, Academic Press, San Diego.

Pratiwi, S. D. & Sato, T. (2016), 'Reconstruction of Paleoceanography Significance in the Western Pacific and Atlantic Oceans during the Neogene Based on Calcareous Nannofossil Productivity and Size Variations, Related to the Global Tectonic Events', *Open Journal of Geology* **6**(8), 931–943.

Preiss-Daimler, I., Baumann, K.-H. & Henrich, R. (2012), 'Carbonate budget mass estimates for Neogene discoasters from the Equatorial Atlantic (Ceara Rise: ODP Site 927)', *Journal of Micropalaeontology* **31**(2), 169–178.

Rae, J. W. B., Zhang, Y. G., Liu, X., Foster, G. L., Stoll, H. M. & Whiteford, R. D. M. (2021), 'Atmospheric CO_2 over the Past 66 Million Years from Marine Archives', *Annual Review of Earth and Planetary Sciences* **49**(1), 609–641.

Raffi, I., Backman, J., Fornaciari, E., Pälike, H., Rio, D., Lourens, L. & Hilgen, F. (2006), 'A review of calcareous nannofossil astrobiochronology encompassing the past 25 million years', *Quaternary Science Reviews* **25**(23-24), 3113–3137.

Ravelo, A. C., Andreasen, D. H., Lyle, M., Olivarez Lyle, A. & Wara, M. W. (2004), 'Regional climate shifts caused by gradual global cooling in the Pliocene epoch', *Nature* **429**(6989), 263–267.

Ravelo, A. C., Dekens, P. S. & McCarthy, M. (2006), 'Evidence for El Niño–like conditions during the Pliocene', *GSA Today* **16**(3), 4–11.

Raymo, M. E. (1994), 'The Initiation of Northern Hemisphere Glaciation', *Annual Review of Earth and Planetary Sciences* **22**(1), 353–383.

Raymo, M. E., Lisiecki, L. E. & Nisancioglu, K. H. (2006), 'Plio-Pleistocene Ice Volume, Antarctic Climate, and the Global δ^{18}O Record', *Science* **313**(5786), 492–495.

Rebotim, A., Voelker, A. H. L., Jonkers, L., Waniek, J. J., Meggers, H., Schiebel, R., Fraile, I., Schulz, M. & Kucera, M. (2017), 'Factors controlling the depth habitat of planktonic foraminifera in the subtropical eastern North Atlantic', *Biogeosciences* **14**(4), 827–859.

Rickaby, R. E. M., Bard, E., Sonzogni, C., Rostek, F., Beaufort, L., Barker, S., Rees, G. & Schrag, D. P. (2007), 'Coccolith chemistry reveals secular variations in the global ocean carbon cycle?', *Earth and Planetary Science Letters* **253**(1-2), 83–95.

Rickaby, R. E. M., Henderiks, J. & Young, J. N. (2010), 'Perturbing phytoplankton: response and isotopic fractionation with changing carbonate chemistry in two coccolithophore species', *Climate of the Past* **6**(6), 771–785.

Rickaby, R. E. M., Schrag, D. P., Zondervan, I. & Riebesell, U. (2002), 'Growth rate dependence of Sr incorporation during calcification of *Emiliania huxleyi*', *Global Biogeochemical Cycles* **16**(1), 6–1–6–8.

Rosenthal, Y., Holbourn, A. E., Kulhanek, D. K., Aiello, I. W., Babila, T. L., Bayon, G., Beaufort, L., Bova, S. C., Chun, J. H., Dang, H., Drury, A. J., Dunkley Jones, T., Eichler, P. P. B., Fernando, A. G. S., Gibson, K., Hatfield, R. G., Johnson, D. L., Kumagai, Y., Li, T., Linsley, B. K., Meinicke, N., Mountain, G. S., Opdyke, B. N., Pearson, P. N., Poole, C. R., Ravelo, A. C., Sagawa, T., Schmitt, A., Wurtzel, J. B., Xu, J., Yamamoto, M. & Zhang, Y. G. (2018*a*), *Expedition 363 summary*, Proceedings of the International Ocean Discovery Program.

Rosenthal, Y., Holbourn, A. E., Kulhanek, D. K., Aiello, I. W., Babila, T. L., Bayon, G., Beaufort, L., Bova, S. C., Chun, J. H., Dang, H., Drury, A. J., Dunkley Jones, T., Eichler, P. P. B., Fernando, A. G. S., Gibson, K., Hatfield, R. G., Johnson, D. L., Kumagai, Y., Li, T., Linsley, B. K., Meinicke, N., Mountain, G. S., Opdyke, B. N., Pearson, P. N., Poole, C. R., Ravelo, A. C., Sagawa, T., Schmitt, A., Wurtzel, J. B., Xu, J., Yamamoto, M. & Zhang, Y. G. (2018*b*), *U1482*, Proceedings of the International Ocean Discovery Program, 363, College Station, TX (International Ocean Discovery Program).

Rosenthal, Y., Holbourn, A. E., Kulhanek, D. K., Aiello, I. W. & Zhang, Y. G. (2017), *International Ocean Discovery Program Expedition 363 Preliminary Report: Western Pacific Warm Pool*, International Ocean Discovery Program Scientific Prospectus.

Rost, B. & Riebesell, U. (2004), Coccolithophores and the biological pump: responses to environmental changes, *in* H. R. Thierstein & J. R. Young, eds, 'Coccolithophores: From Molecular Processes to Global Impact', Springer Berlin Heidelberg, Berlin, Heidelberg, pp. 99–125.

Ruggieri, E., Herbert, T., Lawrence, K. T. & Lawrence, C. E. (2009), 'Change point method for detecting regime shifts in paleoclimatic time series: Application to δ^{18}O time series of the Plio-Pleistocene', *Paleoceanography and Paleoclimatology* **24**(1), 1204.

Saavedra-Pellitero, M., Baumann, K.-H., Ullermann, J. & Lamy, F. (2017), 'Marine Isotope Stage 11 in the Pacific sector of the Southern Ocean; a coccolithophore perspective', *Quaternary Science Reviews* **158**, 1–14.

Saavedra-Pellitero, M., Hernández-Almeida, I., Cabarcos, E., Baumann, K.-H., Dunkley Jones, T., Sierro, F. J. & Flores, J.-A. (2022), 'Coupled Coccolith-Based Temperature and Productivity High-Resolution Reconstructions in the Eastern Equatorial

Pacific During the Last Deglaciation and the Holocene', *Frontiers in Marine Science* **9**.

Schindelin, J., Arganda-Carreras, I., Frise, E., Kaynig, V., Longair, M., Pietzsch, T., Preibisch, S., Rueden, C., Saalfeld, S., Schmid, B., Tinevez, J.-Y., White, D. J., Hartenstein, V., Eliceiri, K., Tomancak, P. & Cardona, A. (2012), 'Fiji: an open-source platform for biological-image analysis', *Nature Methods* **9**(7), 676–682.

Schueth, J. D. & Bralower, T. J. (2015), 'The relationship between environmental change and the extinction of the nannoplankton *Discoaster* in the early Pleistocene', *Paleoceanography and Paleoclimatology* **30**(7), 863–876.

Seki, O., Foster, G. L., Schmidt, D. N., Mackensen, A., Kawamura, K. & Pancost, R. D. (2010), 'Alkenone and boron-based Pliocene pCO_2 records', *Earth and Planetary Science Letters* **292**(1-2), 201–211.

Stevenson, E. I., Hermoso, M., Rickaby, R. E. M., Tyler, J. J., Minoletti, F., Parkinson, I. J., Mokadem, F. & Burton, K. W. (2014), 'Controls on stable strontium isotope fractionation in coccolithophores with implications for the marine Sr cycle', *Geochimica et Cosmochimica Acta* **128**, 225–235.

Stoll, H. M., Arevalos, A., Burke, A., Ziveri, P., Mortyn, G., Shimizu, N. & Unger, D. (2007a), 'Seasonal cycles in biogenic production and export in Northern Bay of Bengal sediment traps', *Deep Sea Research Part II: Topical Studies in Oceanography* **54**(5-7), 558–580.

Stoll, H. M., Guitian, J., Hernandez-Almeida, I., Mejia, L. M., Phelps, S., Polissar, P., Rosenthal, Y., Zhang, H. & Ziveri, P. (2019), 'Upregulation of phytoplankton carbon concentrating mechanisms during low CO_2 glacial periods and implications for the phytoplankton pCO_2 proxy', *Quaternary Science Reviews* **208**, 1–20.

Stoll, H. M., Klaas, C. M., Probert, I., Encinar, J. R. & Alonso, J. I. G. (2002a), 'Calcifica-

tion rate and temperature effects on Sr partitioning in coccoliths of multiple species of coccolithophorids in culture', *Global and Planetary Change* **34**(3-4), 153–171.

Stoll, H. M., Rosenthal, Y. & Falkowski, P. (2002c), 'Climate proxies from Sr/Ca of coccolith calcite: calibrations from continuous culture of *Emiliania huxleyi*', *Geochimica et Cosmochimica Acta* **66**(6), 927–936.

Stoll, H. M. & Schrag, D. P. (2000), 'Coccolith Sr/Ca as a new indicator of coccolithophorid calcification and growth rate', *Geochemistry, Geophysics, Geosystems* **1**(5).

Stoll, H. M., Shimizu, N., Archer, D. & Ziveri, P. (2007b), 'Coccolithophore productivity response to greenhouse event of the Paleocene–Eocene Thermal Maximum', *Earth and Planetary Science Letters* **258**(1-2), 192–206.

Stoll, H. M. & Ziveri, P. (2002), 'Separation of monospecific and restricted coccolith assemblages from sediments using differential settling velocity', *Marine Micropaleontology* **46**(1-2), 209–221.

Stoll, H. M., Ziveri, P., Geisen, M., Probert, I. & Young, J. R. (2002b), 'Potential and limitations of Sr/Ca ratios in coccolith carbonate: new perspectives from cultures and monospecific samples from sediments', *Philosophical Transactions of the Royal Society of London. Series A: Mathematical, Physical and Engineering Sciences* **360**(1793), 719–747.

Stoll, H. & Ziveri, P. (2004), Coccolithophorid-based geochemical paleoproxies, *in* H. R. Thierstein & J. R. Young, eds, 'Coccolithophores: From Molecular Processes to Global Impact', Springer Berlin Heidelberg, Berlin, Heidelberg, pp. 529–562.

Suchéras-Marx, B. & Henderiks, J. (2014), 'Downsizing the pelagic carbonate factory: Impacts of calcareous nannoplankton evolution on carbonate burial over the past 17 million years', *Global and Planetary Change* **123**, 97–109.

Šupraha, L. & Henderiks, J. (2020), 'A 15-million-year-long record of phenotypic evolution in the heavily calcified coccolithophore *Helicosphaera* and its biogeochemical implications', *Biogeosciences* **17**(11), 2955–2969.

Tangunan, D., Berke, M. A., Cartagena-Sierra, A., Flores, J. A., Gruetzner, J., Jiménez-Espejo, F., Levay, L. J., Baumann, K.-H., Romero, O., Saavedra-Pellitero, M., Coenen, J. J., Starr, A., Hemming, S. R., Hall, I. R. & Party, E. . (2021), 'Strong glacial-interglacial variability in upper ocean hydrodynamics, biogeochemistry, and productivity in the southern Indian Ocean', *Communications Earth & Environment* **2**(80).

Tangunan, D. N., Baumann, K.-H., Just, J., Levay, L. J., Barker, S., Brentegani, L., De Vleeschouwer, D., Hall, I. R., Hemming, S. & Norris, R. (2018), 'The last 1millionyears of the extinct genus *Discoaster*: Plio–Pleistocene environment and productivity at Site U1476 (Mozambique Channel)', *Palaeogeography, Palaeoclimatology, Palaeoecology* **505**, 187–197.

Thomson, D. J. (1982), 'Spectrum estimation and harmonic analysis', *Proceedings of the IEEE* **70**(9), 1055–1096.

Tremblin, M., Hermoso, M. & Minoletti, F. (2016), 'Equatorial heat accumulation as a long-term trigger of permanent Antarctic ice sheets during the Cenozoic', *Proceedings of the National Academy of Sciences* **113**(42), 11782–11787.

Van Der Lubbe, H. J. L., Hall, I. R., Barker, S., Hemming, S. R., Baars, T. F., Starr, A., Just, J., Backeberg, B. C. & Joordens, J. C. A. (2021), 'Indo-Pacific Walker circulation drove Pleistocene African aridification', *Nature* **598**(7882), 618–623.

Venti, N. L., Billups, K. & Herbert, T. D. (2013), 'Increased sensitivity of the Plio-Pleistocene northwest Pacific to obliquity forcing', *Earth and Planetary Science Letters* **384**, 121–131.

Waite, A. J., Gibbs, S. J., Diester-Haass, L., Rickaby, R. E. M. & Billups, K. (2008), 'A top-down and bottom-up comparison of paleoproductivity proxies: Calcareous nan-

nofossil Sr/Ca ratios and benthic foraminiferal accumulation rates', *Geochemistry, Geophysics, Geosystems* **9**(6).

Wara, M. W., Ravelo, A. C. & Delaney, M. L. (2005), 'Permanent El Niño-like conditions during the Pliocene warm period', *Science* **309**(5735), 758–761.

Westerhold, T., Marwan, N., Drury, A. J., Liebrand, D., Agnini, C., Anagnostou, E., Barnet, J. S. K., Bohaty, S. M., De Vleeschouwer, D., Florindo, F., Frederichs, T., Hodell, D. A., Holbourn, A. E., Kroon, D., Lauretano, V., Littler, K., Lourens, L. J., Lyle, M., Palike, H., Rohl, U., Tian, J., Wilkens, R. H., Wilson, P. A. & Zachos, J. C. (2020), 'An astronomically dated record of Earth's climate and its predictability over the last 66 million years', *Science* **369**(6509), 1383–1387.

Willeit, M., Ganopolski, A., Calov, R., Robinson, A. & Maslin, M. (2015), 'The role of CO_2 decline for the onset of Northern Hemisphere glaciation', *Quaternary Science Reviews* **119**, 22–34.

Wilson, D. J., van de Flierdt, T., McKay, R. M. & Naish, T. R. (2022), Pleistocene antarctic climate variability: ice sheet, ocean and climate interactions, *in* F. Florindo, M. Siegert, L. D. Santis & T. Naish, eds, 'Antarctic Climate Evolution (Second Edition)', Elsevier, Amsterdam, pp. 523–621.

Young, J. (1990), 'Size variation of Neogene *Reticulofenestra* coccoliths from Indian Ocean DSDP Cores', *Journal of Micropalaeontology* **9**(1), 71–85.

Young, J. (1998), Neogene, *in* P. R. Bown, ed., 'Calcareous Nannofossil Biostratigraphy', Springer, London, pp. 225–258.

Zachos, J., Pagani, M., Sloan, L., Thomas, E. & Billups, K. (2001), 'Trends, Rhythms, and Aberrations in Global Climate 65 Ma to Present', *Science* **292**(5517), 686–693.

Zhang, C., Wang, Y., Deng, T., Wang, X., Biasatti, D., Xu, Y. & Li, Q. (2009), 'C4 ex-

pansion in the central Inner Mongolia during the latest Miocene and early Pliocene', *Earth and Planetary Science Letters* **287**(3-4), 311–319.

Zhang, H., Liu, C., Mejía, L. M. & Stoll, H. (2021), 'Technical note: Accelerate coccolith size separation via repeated centrifugation', *Biogeosciences* **18**(5), 1909–1916.

Zhang, H., Stoll, H., Bolton, C., Jin, X. & Liu, C. (2018), 'Technical note: A refinement of coccolith separation methods: measuring the sinking characteristics of coccoliths', *Biogeosciences* **15**(15), 4759–4775.

Zhang, S., Zhou, R. & DePaolo, D. J. (2020), 'The seawater Sr/Ca ratio in the past 50 Myr from bulk carbonate sediments corrected for diagenesis', *Earth and Planetary Science Letters* **530**.

Zhang, Y. G., Pagani, M. & Liu, Z. (2014), 'A 12-million-year Temperature History of the Tropical Pacific Ocean', *Science* **344**(6179), 84–87.

Zhao, Y., Wang, Y. & Quigg, A. (2015), 'Comparison of population growth and photosynthetic apparatus changes in response to different nutrient status in a diatom and a coccolithophore', *Journal of Phycology* **51**(5), 872–884.

Ziveri, P., Stoll, H., Probert, I., Klaas, C., Geisen, M., Ganssen, G. & Young, J. (2003), 'Stable isotope 'vital effects' in coccolith calcite', *Earth and Planetary Science Letters* **210**(1-2), 137–149.

Ziveri, P., Thoms, S., Probert, I., Geisen, M. & Langer, G. (2012), 'A universal carbonate ion effect on stable oxygen isotope ratios in unicellular planktonic calcifying organisms', *Biogeosciences* **9**(3), 1025–1032.